Sintering Studies of Magnesia-Chromite Refractory Composites

by

Hamidreza Zargar

A THESIS SUBMITTED IN PARTIAL FULFILLMENT OF
THE REQUIREMENTS FOR THE DEGREE OF

DOCTOR OF PHILOSOPHY

in

The Faculty of Graduate and Postdoctoral Studies
(Materials Engineering)

THE UNIVERSITY OF BRITISH COLUMBIA

(Vancouver)

March 2014

Abstract

The magnesia-chromite refractory composites are the best candidates for the lining of non-ferrous metal smelting and refining furnaces, due to their high melting temperature, chemical inertness, and excellent thermal shock resistance. However, their high sintering temperatures (>1700°C) increase the processing complexity and costs. In this investigation, the primary goal was to study the sintering of these composites, with the long-term engineering goal to reduce their sintering temperature to <1500°C in air.

The materials were synthesized via chemical methods using nitrates to assure chemical homogeneity. Al_2O_3, Fe_2O_3, and SnO_2 affected the kinetics of the $MgCr_2O_4$ formation and increased the density of $MgCr_2O_4$ in the order Fe_2O_3>Al_2O_3>SnO_2. The enhanced $MgCr_2O_4$ densification was attributed to the cation distribution in spinel structure (inversion phenomenon), caused by the inherent affinity of Fe^{+3} and Al^{+3} to tetrahedral sites. Fe_2O_3 and Al_2O_3 showed to form inverted spinel, while SnO_2 resulted in the formation of normal spinel solid solutions.

Twelve magnesia-chromite composites were synthesized to study the effects of Al_2O_3, Fe_2O_3 and Cr_2O_3 on their sintering conditions; Cr_2O_3 decreased the density, while Fe_2O_3 and Al_2O_3 enhanced the densification of composites. The microstructural studies revealed that Fe_2O_3 and Al_2O_3 reduced the dihedral angle between MgO and spinel, while Cr_2O_3 increased it. The increased densification by Fe_2O_3 and Al_2O_3 was attributed to the decreased dihedral angle and formation of inverted solid solutions.

The optimized composition [MgO6.9$Cr_2O_3$6.9$Al_2O_3$2.7Fe_2O_3]mol% (*MK*) reached nearly full density in air at 1475˚C for 70minutes; 1700°C is currently used for magnesia-chromite refractories.

In order to study the effects of the particle size on densification, magnesia-chromite composites (*NMK*) with average particle size of ~20 nm were synthesized via Pechini's method. Reducing the particle size from 1.2 μm for *MK* to 20 nm for *NMK* reduced the onset sintering temperature by 200°C to 1000°C.

The densification results were evaluated using master sintering curve theory for the first time for this kind of composites. The sintering activation energy was 443.7 and 302.6 kJ/mol for *MK* and *NMK* respectively. It was hypothesized that the oxygen diffusion through lattice and grain boundaries was rate controlling mechanism for *MK* and *NMK* respectively.

Preface

This research program was conducted within the collaborative research between Teck Metals Ltd., Trail, B.C., Clayburn Industries, Abbotsford, BC and the University of British Columbia, Vancouver BC (UBC), co-supported by NSERC-CRD grant. Teck metal provided UBC ceramic group (UBCeram) technical information on the performance of the refractories currently used in their facility. Clayburn provided UBCeram with the raw materials for making mag-chrome refractory castables.

One journal paper and 2 conference papers have been published so far based on the results of this project, and are included in the present thesis. Parts of Chapters 5 and 6 are submitted for publication in peer reviewed journals, as listed below. I am the primary contributor to the publications listed below, and the co-authors contributions are as follow: my supervisors, Drs. Tom Troczynski and George Oprea extensively commented on the experimental and analysis methods, and the results interpretation; C. Oprea contributed to editorial work on the papers.

1- H. Zargar, G.Oprea, T. Troczynski, Influence of solid solution formation on the solid state sintering $MgCr_2O_4$, Unitecr 2013, September , Victoria, Canada.

2- H. Zargar, C. Oprea, G. Oprea, T. Troczynski, The effect of nano-Cr_2O_3 in solid solution assisted sintering of MgO refractories, Ceramic International, 2012, 38, 6235–6241.

3- H. R. Zargar, G. Oprea, C.Oprea and T.Troczynski , Evaluation of the role of nano chromia in performance of magnesia chromite castables, Unitecr 2011, October 2011, Kyoto , Japan.

Table of Contents

List of Tables

List of Figures

Nomenclature

Latin Symbols

m	Numerical exponent
n	Numerical exponent
H	Temperature depended constant
a	Concentration of hydrogen
L	Length
C	constant
E_a	Activation energy
D_s	Surface diffusion coefficient
D_l	Lattice diffusion coefficient
D_{gb}	Grain boundary diffusion coefficient
P_0	vapor pressure over a flat surface
k	Boltzman constant
m_a	Mass of atom
T	Absolute temperature
GB	Grain boundary
G	Grain size
ΔG°	Standard free of formation
ΔG	Free energy of formation
ΔH	Enthalpy of formation
ΔS	Entropy of formation
TD	Theoretical density
BD	Bulk density
WA	Water absorption
AP	Apparent porosity
W_i	Weight of immersed specimen
W_w	Weight of saturated specimen
W_d	Weight of dry specimen
RD	Relative density
Z	number of molecules per unit cell
M	molecular weight of sample
N	Avogadro number
V	volume of unit cell
n_A	Avarmi constant
$W_{1/2}$	Full width at half maximum
F_0	structural factor for normal spinel
F_1	numerical factor
I_{hkl}	Intensity
F	Structure factor
P	Multiplicity factor
Lp	Lorentz-polarization factor
ΔG_D	free energy of disordering cation distribution

N_a	Mole fraction of $MgFe_2O_4$
M_a	Mole fraction of $MgAl_2O_4$
r	Cationic radios
x	The mole percent of trivalent and tetravalent cation substituted for Cr
v	The mole percent of Fe_2O_3 and SnO_2 substituted for $MgCr_2O_4$ and Cr_2O_3
x_d	The diffusion depth
ρ_0	initial density at time (t_0)
t	time
γ	Surface energy
$CPFD$	cumulative percentage finer than, d
Q	Activation energy of sintering
d	Smallest [article size
D	Largest particle size

Greek Symbols

δ_S	thickness of surface
δ_{gb}	grain boundary
γ_{sv}	specific surface energy
μ	viscosity
ρ	density
ξ	Inversion parameter
λ_{XRD}	Wave length
β_{XRD}	full width at half maximum of the intensity
ϕ	Heating rate
α	Inversion parameter of divalent cation
β	Inversion parameter of trivalent cation
λ	Related to the inversion parameter
$\alpha^{A\text{-}B}$	the difference between site preference energies of A and B
$\beta^{'}$	constant
N_a	numbers of molecules $MgFe_2O_4$
M_a	numbers of molecules $MgAl_2O_4$
$\varphi_{M/M}$	Dihedral angle between magnesia grains
$\varphi_{S/M}$	Dihedral angle between magnesia and spinel grains
$\varphi_{S/S}$	Dihedral angle between spinel grains
$\gamma_{solid/liquid}$	Grain boundary energy of solid liquid interface
ρ_0	initial density at time (t_0)
γ	Surface energy
Γ_v	Microstructure scaling factor for lattice
Γ_b	Microstructure scaling factor for grain boundary
Ω	Atomic volume
$\phi(\rho)$	Constant includes all the microstructure evolution during sintering
$\Theta(t,T(t))$	Sintering parameters depending on the thermal history
$G(\rho)$	G function relates grain size to density

Q	Activation energy of sintering
d	Smallest particle size

Abbreviations

FCC	Face centered cubic
FF	$FeFe_2O_4$
MF	$MgFe_2O_4$
FA	$FeAl_2O_4$
MA	$MgAl_2O_4$
FC	$FeCr_2O_4$
MC	$MgCr_2O_4$
TGA	Thermal gravimetry analysis
SSR	Solid state reaction
XRD	X-ray diffraction
HMOR	Hot modulus of rupture
MOR	Modulus of rupture
CCS	Cold crushing strength
MK	Magnesia chromite composites (MgO-$6.9Al_2O_3$-$2.7Fe_2O_3$-$6.9Cr_2O_3$)[*d*: 1.27um]
NMK	Magnesia chromite composites (MgO-$6.9Al_2O_3$-$2.7Fe_2O_3$-$6.9Cr_2O_3$) [*d*: 20nm]
STA	Simultaneous thermal analysis
BBOC	Bottom blown oxygen convertor
TCML	Teckmetal Ltd
CIP	Cold isostatic pressing
DSC	Differential scanning calorimeter
MK1	MgO-$6.9Al_2O_3$-$2.71Fe_2O_3$-$4.9Cr_2O_3$
MK2	MgO-$6.9Al_2O_3$-$2.71Fe_2O_3$-$5.9Cr_2O_3$
MK3	MgO-$6.9Al_2O_3$-$2.71Fe_2O_3$-$6.9Cr_2O_3$
MK4	MgO-$6.9Al_2O_3$-$2.71Fe_2O_3$-$7.9Cr_2O_3$
MK5	MgO-$6.9Al_2O_3$-$2.71Fe_2O_3$-$8.9Cr_2O_3$
MK6	MgO-$4.9Al_2O_3$-$2.71Fe_2O_3$-$6.9Cr_2O_3$
MK7	MgO-$5.9Al_2O_3$-$2.71Fe_2O_3$-$6.9Cr_2O_3$
MK8	MgO-$7.9Al_2O_3$-$2.71Fe_2O_3$-$6.9Cr_2O_3$
MK9	MgO-$8.9Al_2O_3$-$2.71Fe_2O_3$-$6.9Cr_2O_3$
MK10	MgO-$6.9Al_2O_3$-$3.71Fe_2O_3$-$6.9Cr_2O_3$
MK11	MgO-$6.9Al_2O_3$-$1.71Fe_2O_3$-$6.9Cr_2O_3$
MK12	MgO-$6.9Al_2O_3$-$0.71Fe_2O_3$-$6.9Cr_2O_3$

Acknowledgments

I would like to express my sincerest gratitude to my supervisors, Dr. Tom Troczynski and Dr. George Oprea, for their insightful guidance and ongoing patience. They have helped me to improve my research quality and presentation skills by their constructive comments during the course of my study. I would like to thank them for their support and encouragement thorough out this research. It is not exaggeration if I say they are truly mentor for me.

I would like to recognize my supervisor committee members for their technical suggestions and guidance in the early stages of this thesis.

I would like to show gratitude to Dr. Akram Alfantazi for his permission to use his lab facilities. I would like to acknowledge Dr. Edouard Asselin who generously provided me with the access to use his *STA* instrument.

I would like to express thanks to Mrs. Carmen Oprea for her invaluable support during my experiments.

I would also like to express my appreciation to Mr. Dominic Verhelst and Mr. Terry Mills for their constructive advice and suggestions.

I would like to sincerely thank Mr. Ross Mcleod, Mr. Carl Ng, Mr. David Torok, Mr. Glenn Smith, Mr. Rudy Cardeno, Mr. Gary Lockart, and Mr. Roger Bennett for their technical supports. Special thanks to Mr. Wonsang Kim and Mr. Jacob Kabel for the time they spent to train me on instruments, repair furnaces and troubleshooting.

I would like to thank administration office personals Mrs. Fiona Webster, Mrs. Mary Jansepar, and Mrs. Michelle Tierney for their invaluable support from the day I arrived to UBC until my graduation day.

I would like to appreciate my aunts, cousins especially Isar, and their families for keeping my parents company during my studies in Canada. I would also like to acknowledge all my helpful and kind family and friends in Vancouver, Canada.

I would like to express my respect to Dr. Farhad Golestanifard, and Dr. Hamidreza Rezaei, my previous supervisors at Iran University of Science and Technology, for their invaluable support. I would like to express my sincerest gratitude to Dr. Reza Bayati who always inspired me in both my academic and personal life.

This work was supported by Clayburn Refractories, Teckmetal Ltd and the Natural Sciences and Engineering Research Council (NSERC) of Canada.

Dedication

With love and respect to my dearests father Mahmood, mother Maryam, and brother Ehsan

for their eternal love and support during my entire life.

Without them I would not be here.

&

To my love Neda - her love inspired me and this thesis has been finalized with her unwavering

support and encouragement.

Chapter 1. Introduction

Magnesia chromite refractories (called mag-chrome refractories) are widely used as refractory linings for the furnaces in steel, copper, nickel and lead industries. Mag-chrome refractories are a sub group of basic refractories preferentially used in the above applications due to their superior thermal shock resistance and chemical inertness in contact with molten metal and slags, in comparison to other basic refractories, including magnesia-spinel and magnesia refractories.

The mag-chrome refractories are usually made from fused magnesia chromite grains. The fused grains with the desired particle size distribution (typically 0.1 μm to 7 mm) are mixed and then pressed to form a brick. The bricks are sintered in a tunnel kiln for about 48-72 hours, depending on its size. The sintering temperature is usually about 1700-1800°C and the sintering atmosphere is partially reducing to help the densification of fused grains.

Figure 1-1 illustrates the schematic of a mag-chrome refractory microstructure. The large grains (>1 mm) called aggregates are bonded together by smaller particles (<1mm) called the matrix or binding system. During sintering the matrix would densify and form a bond with the aggregates, thus giving strength and integrity to the brick.

The matrix is the key component of the mag-chrome bricks because it is the first component of the brick which reacts with the corrosive environment. Therefore, the composition, the sintering behavior, and the interaction between binding system (matrix) and aggregates (fused magnesia chromite grains) are important in designing a microstructure for the refractory applications. The binding system for mag-chrome grains is usually fine fused grains and a small amount of MgO, Al_2O_3, and Fe_2O_3 to enhance the densification. These oxides react to form

spinel during the sintering and enhance the densification probably via synthesis and sintering process. No chromium oxide usually would be added because Cr_2O_3 reduces the densification of the binding system. Therefore, it is expected that the binding system would be vulnerable to fast corrosion especially when it is in contact with the molten slags used in the non-ferrous industry.

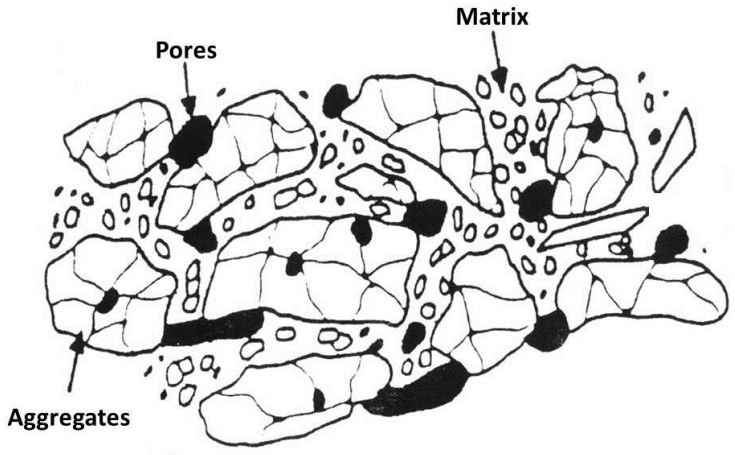

Figure 1-1. The schematic of a mag-chrome refractory[6]

The phase analysis of fused mag-chrome grains indicates that they are composed of magnesia and a complex spinel solid solution. Therefore, a fully dense binding system (matrix) with the same composition or with high Cr_2O_3 composition would be ideal for the mag-chrome brick. Moreover, a composition with a spinel crystal structure is favorable because it may bond better to aggregate with the same crystal structure. In addition, reducing the sintering temperature of mag-chrome refractory from 1700°C to less than 1500°C via designing an appropriate binding system is significant for industry because high sintering temperature increases the production costs and contributes to the greenhouse effect by the CO_2 emission associated with fossil combustible, commonly used for sintering.

Based on these rationales, the objective of this study was to design a binding system with the highest Cr_2O_3 content which reacts with aggregates and forms bond, and also a binding

system which sintered to densities above 95% at temperatures below 1500°C. Magnesia chromite spinel ($MgCr_2O_4$) and $(Mg_{1-x-y}Al_xFe_y)[Mg_{x+y}Al_xFe_yCr_{1-x-y}]_2O_4$ were selected as the base structures, and the effect of Al_2O_3, Fe_2O_3, and Cr_2O_3 on their crystal structure and densification were studied. The optimized composition, sintered to 96% density at 1475°C for 70 minutes in air, was selected as the binding system. The effect of reducing the particle size to nano scale (20 nm) on the sintering of selected binding system was evaluated. The sintering kinetics of this system was also studied. Attempts have been made to evaluate the effect of the designed binding system on the densification of the mag-chrome refractory. In this regard, a mag-chrome refractory was made using fused mag-chrome grains as aggregates and the designed composite as the binding system (matrix).

Chapter 2. Literature review

The sintering process has been used for thousands of years for the production of bricks, porcelains, etc.[5]. Its application is now also being directed to the manufacture of engineered microstructures suitable for certain applications, for instance dental implants, semiconductor substrates, turbine blades, etc.

The goal of sintering is to create a reproducible dense ceramic or metal part with a designed microstructure, which can be achieved through selecting and optimizing the processing variables. Therefore, sintering studies often focus on how the processing variables influence the final microstructure of the sintered body[1]. This is a measure of the microstructural and bulk parameters, or physical, mechanical and electrical properties, or their combinations, as a function of sintering parameters, including time and temperature[5].

Magnesia-chromite* refractory composites have been used for more than 50 years as refractory linings in non-ferrous metal smelting and refining furnaces, owing to their high corrosion resistance against high silica and iron content slags and gaseous environments. However, the challenge of using them is the rapid oxidation of Cr during sintering. To avoid this, the sintering of magnesia-chromite refractory composites takes place at relatively high temperatures (~1750°C) and in a controlled atmosphere, which leads to high production costs. While the sintering mechanisms of MgO and chromite are separately well understood[17-19], there is limited published work focusing on the sintering mechanism of magnesia-chromite refractory composites. Chromite is defined as a solid solution between two or more spinels, wherein one of

* Chromite is the mineralogical name of $FeCr_2O_4$ (*FC*), however, it generally refers to any chromium-containing spinels or spinel solid solutions of [$FeFe_2O_4$(*FF*), $MgFe_2O_4$(*MF*), $FeAl_2O_4$(*FA*), $MgAl_2O_4$(*MA*), $MgCr_2O_4$(*MC*)][6]. However, magnesia-chromite term in this context refers to MgO- $MgCr_2O_4$ composites and henceforth called *MK* composites.

them contains chromium in its composition[6]. The magnesia-chromite refractory composites contain spinel solid solutions that may experience different degrees of disordering, due to the cations movement between tetra and octahedral sites; thus the correlation between sintering properties and the degree of disordering has to be identified.

Many researchers have studied the structure of spinel solid solutions and evaluated the cations distribution in such structures[20,21]. However, to the best of author's knowledge, there are no published works correlating the extent of disordering to the sintering properties of spinel solid solutions, and there are only a few studies focused on the spinel solid solutions sintering.

This literature review will look at the sintering of magnesia-chromite refractory composites regarding three main research topics: sintering mechanisms of MgO-spinel composites, sintering mechanisms of Cr_2O_3 and Cr-containing spinels, and cation distribution in spinel solid solutions.

2.1 Sintering theory overview

Sintering can be defined as a thermally activated process that results in consolidation by bond formation between individual particles via mass transport mechanisms. It is accompanied by a lowering of the free energy of the system, due to reduced total interfacial energy[4].

Sintering is categorized based on the mechanism by which the consolidation takes place. In solid-state sintering, the powder compact shrinks by the solid-state diffusion. In liquid-state sintering, the densification occurs in the presence of a liquid phase. If the liquid phase is only present in the early stage of sintering and the full densification occurs in the solid state, then this is a transient liquid-phase sintering[4]. Viscous sintering takes place in amorphous materials, where the volume fraction of liquid is high enough to lead to full densification by viscous flow of the grain-liquid mixture. Figure 2-1 shows the temperature range for each sintering type[1,4,5].

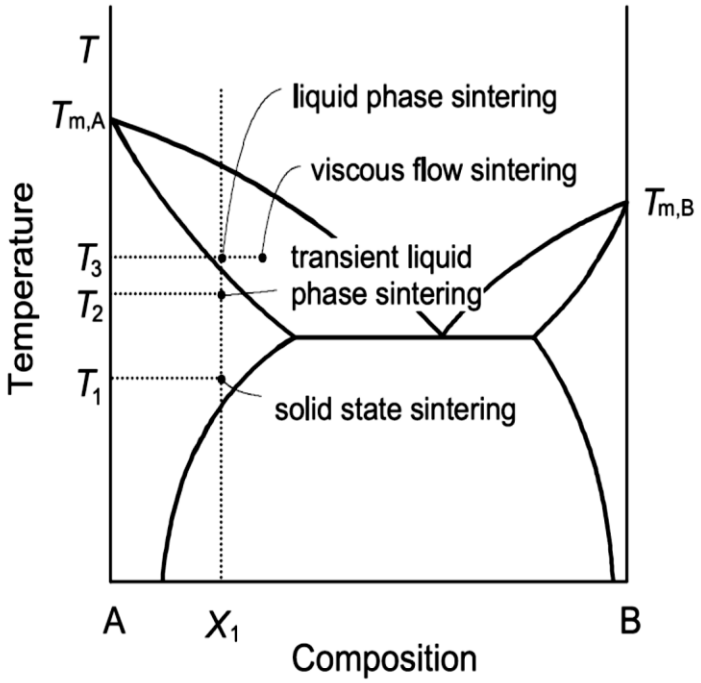

Figure 2-1. Illustration of various types of sintering[4]

2.1.1 Sintering mechanisms

As mentioned in section 2.1, sintering relies on mass transport mechanisms, which determine how mass transfers in response to the sintering driving force. There are two main mass transport mechanisms during sintering: bulk transport and surface transport. Although they both rely on the type and concentration of defects[*] in the crystal structure, and contribute to the bond formation, only the bulk mass transport mechanisms are responsible for densification.

The surface transport mechanisms indicate that mass flow initiates and terminates on the surface of the particles. It includes surface diffusion, evaporation, and condensation. As a result of the surface mass transport mechanisms, the particles contact area (neck) will grow, which leads to surface area reduction and bond formation, but no shrinkage (reduction in the distance

[*] Crystal defects are displacement of an atom (point defect), arrays of atoms (line defect), atomic plan (planar defect) or cluster of atoms (volume defect) from the ideal arrangement of the crystal.

between the particle centers)[4]. Evaporation and condensation usually occur during the sintering of materials with high vapor pressure and are the dominating transport mechanism in sintering of the materials with small particle size and high surface area. In contrast, surface diffusion involves the atom movement between surface defects such as kinks and vacancies. The bond between the surface defect and the atom breaks first, then the atom moves and reattaches to the next available site, which is usually a kink. This is the initial mechanism of the sintering in almost all materials, and its contribution is higher for materials with highly curved surfaces and defective sites, where the concentration of vacancies is high due to the capillary forces[1].

Bulk mass transport mechanisms are volume diffusion, mass diffusion and plastic flow, the latter usually occurring during pressure sintering[22]. The volume diffusion (or lattice diffusion) is the movement of vacancies through a crystalline structure, and accordingly, is influenced by temperature, composition and curvature. In contrast, the grain boundary (*GB*) diffusion indicates the mass flow between *GB*s. The *GB* is a narrow region (2-5 nm) between sintered grains, which is highly defected[22]. Thus the mass transport is faster than volume diffusion. The activation energy of *GB* diffusion is between that of the surface and volume diffusion. The summary of sintering mechanisms and their contribution to densification is depicted in Figure 2-2.

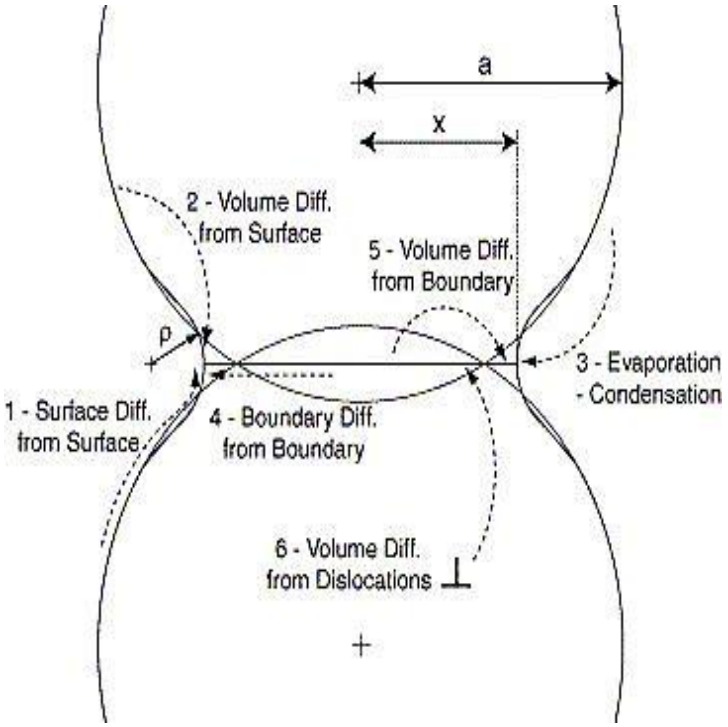

Figure 2-2. Different sintering mechanisms:1) Surface diffusion, 2) Volume diffusion from the surface, 3) Evaporation and condensation, 4) Grain boundary diffusion, 5) Volume diffusion from the grain boundary, and 6) Plastic flow (dislocation movement). All mechanisms lead to bond formation, but only the first 3 ones are accompanied by densification[1]

2.1.2 Sintering models and equations

Over the last five decades several models have been introduced to study the sintering kinetics of particles. They relate the sintering rate to the particle characteristics and compactness, and the sintering atmosphere and temperature. The derived models usually assume that the particles in the initial powder compact are spherical and of the same size, and that they are uniformly packed. These assumptions made the accuracy of the equations debatable[23]. The solid-state sintering process occurs in three overlapping stages, which are schematically shown in Figure 2-3.

The first stage is called initial stage sintering, in which the particle rearrangement and the bond formation initiate at the primary contact points. The contribution of this stage to the densification is very limited, and is about 3 to 5 %.

The modeling of the initial stage sintering was first published by Kingery and Berg[24], Coble[25], and Johnson and Cutler[26]. According to their estimations, the relation between shrinkage and densifying mechanisms can be expressed as below:

$$\left(\frac{\Delta L}{L_0}\right)^{\frac{m}{2}} = -\frac{H}{2^m a^n} t \qquad 2\text{-}1$$

where ΔL is the change in the length, L_0 is the initial length, m and n are numerical exponents indicating the mechanism of sintering, and H is a function of temperature that includes material and geometrical parameters. Table 2-1 shows the value of m and n for different mechanisms. In practice, the sintering mechanism of the initial stage of sintering can be estimated by plotting $\mathrm{Log}\left(\frac{\Delta L}{L_0}\right)$ versus Log(t). The curve would be a straight line with the slope of (1/m).

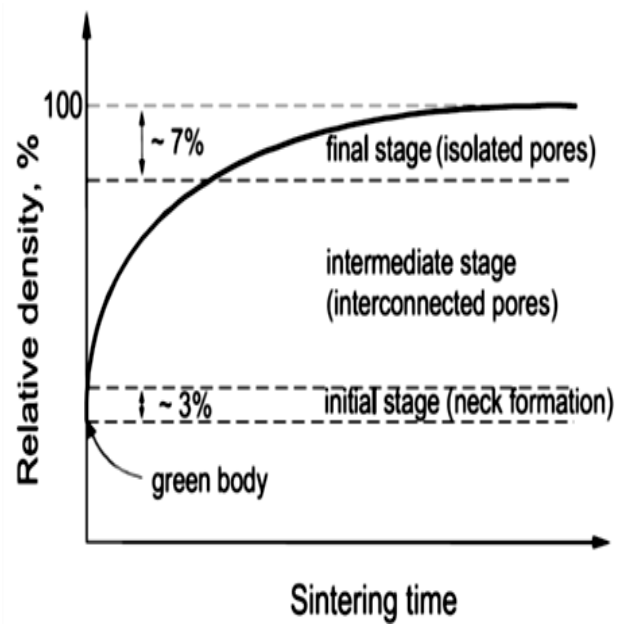

Figure 2-3. Schematic of the sintering process of a compacted powder, illustrating 3 stages of solid state sintering[4].

However, when more than one sintering mechanism is active, then this method is no longer accurate enough to be used for the sintering mechanism estimation. The activation energy of densification in the initial stage of sintering can also be calculated by plotting the results of linear shrinkage vs temperature, and using the equations derived by Tietz[27] and Younge[28].

$$\left(\frac{(\frac{dL}{L})}{T}\right) = C.exp(-\frac{nE_a}{RT}) \qquad 2\text{-}2$$

In the former equation, $\left(\frac{\mathrm{d}L}{L}\right)$ is the relative shrinkage at temperature T (limited to the initial sintering stage), E_a is the activation energy and n is a constant describing the sintering mechanism (n = 1, 0.5 and 0.33 for viscous, volume diffusion or grain-boundary diffusion respectively).

The second stage of sintering is called intermediate stage sintering and is the most important, since it determines the properties of the sintered compact. This stage covers about 90 % of the total densification that occurs during the whole sintering process[5]. The driving force is the reduction of surface energy due to the difference in surface curvature and consequent mass transport[29].

The intermediate stage initiates after the grain growth and pore shape change, when pores and grain boundaries reach an equilibrium state and form dihedral angles. At this stage, the pore phase is considered as a continuous channel which shrinks afterward. In order to develop a model of this sintering stage, Coble[30] approximated the complex shape of the pore by a continuous cylinder and applied diffusion equations. Equations 2-3 and 2-4 show the proposed models based on lattice and *GB* diffusion, respectively.

$$\frac{1}{\rho}\frac{d\rho}{dt} \sim \frac{10 D_l \gamma_{sv} \Omega}{\rho G^3 kT} \quad \text{2-3}$$

$$\frac{1}{\rho}\frac{d\rho}{dt} \sim \frac{10 D_{gb} \delta_{gb} \gamma_{sv} \Omega}{\rho (1-\rho)^{1/2} G^4 kT} \quad \text{2-4}$$

In these equations ρ is the density; D_l and D_{gb} are diffusion coefficients of the lattice and grain boundary diffusion, respectively; δ_{gb} is the thickness of the grain boundary; γ_{sv} is the specific surface energy; *k* is the Boltzman constant; *G* is the grain size; *T* is the absolute temperature and $\frac{d\rho}{dt}$ is the densification rate.

Table 2-1. Estimated values for each sintering mechanism[1]

Mechanism	*m*	*n*	*H*[b]
Surface diffusion[a]	7	4	$\frac{56 D_s \delta_s \gamma_{sv} \Omega}{kT}$
Lattice diffusion from the surface[a]	4	3	$\frac{20 D_l \gamma_{sv} \Omega}{kT}$
Evaporation and condensation[a]	3	2	$\frac{3 P_0 \gamma_{sv} \Omega}{2(\pi M k T)^{1/2} kT}$
Grain boundary diffusion	6	4	$\frac{96 D_{gbs} \delta_{gbs} \gamma_{sv} \Omega}{kT}$
Lattice diffusion from grain boundary	5	3	$\frac{80 \pi D_{ls} \gamma_{sv} \Omega}{kT}$
Viscous flow	2	1	$\frac{3 \gamma_{sv}}{2\eta}$

a: denotes non-densifying mechanism, i.e., $\left(\frac{\Delta L}{L_0}\right) = 0$

b: *Ds*, *Dl*, *Dgb*: diffusion coefficient of surface, lattice, and grain boundary diffusion; δs, δgb; thickness of surface and grain boundary; γ_{sv}: specific surface energy; *P0*: vapor pressure over a flat surface; *k*: Boltzman constant; m: mass of atom; *T*: absolute temperature; η: viscosity.

These assumptions introduced errors that resulted in predicted shrinkage rate higher than the experimental results. Kakar[31] added two more assumptions to the previous model. The first was considering the shape and the second one was considering one active densifying mechanism,

i.e. volume diffusion or *GB* diffusion. In his model the pores and grains had certain geometries (polyhedral and cylindrical respectively), however the grain and pore sizes were set as constant during sintering. The model was criticized by Jorgensen[32] for not considering the grain growth and the mathematical errors, respectively.

In 1970 Johnson[33] proposed a model for intermediate-stage sintering in which the densification rate was related to the geometry of the compact during sintering, and to the bulk diffusion coefficients (D_v and D_{gb}). In this model, simultaneous grain and pore growth was assumed during sintering. In fact, the Johnson model is a modified version of the Coble model.

The third stage is called final stage sintering, in which the elimination of the isolated pores continues until the theoretical density is reached. Although the grain growth initiates during the intermediate stage of sintering, this phenomenon is the main feature for the final stage. Due to the separation of *GB*s from pores, the pores move easier and faster than in the previous stage. As a result, the large grains tend to increase in size at the expense of the smaller grains, while simultaneously the pores shrink continuously until are totally eliminated[33].

A final stage sintering model has also been developed by Coble[25] and has become a standard, despite the fact that the effects of surface sintering mechanisms have not been included. In addition to Coble's model, Herring's scaling law has been also used for studying the kinetics in the final stage sintering[34,16]. In this model, the effect of the pore size on the material transport at *GB*/pore interface was taken into account. According to the concept introduced by Herring's law, Kang and Jung[16] derived the following equations to relate the densification rate to the volume diffusion and the *GB* diffusion, respectively:

$$\frac{d\rho}{dt} = \frac{441 D_l \gamma_{sv} \Omega}{RTG^3}(1-\rho)^{1/3} \quad \text{2-5}$$

$$\frac{d\rho}{dt} = \frac{735 D_{gb} \delta_{gb} \gamma_{sv} \Omega}{RTG^4} \quad \text{2-6}$$

All parameters have been already introduced

In all the introduced models it is assumed that the grain size is constant, while it is changing during sintering, and it considerably changes the kinetics of sintering. For instance grain growth in the initial stage of sintering causes an increase in pore size locally and decreases the densification rate[35]. Grain growth is basically an increase in dimension of grains during sintering. The mechanisms of grain growth are usually different from those of densification; however, they are diffusion controlled. Grain growth occurs as atoms (ions) diffuse for a fraction of interatomic distance at grain boundary, resulting in dimensional increase of a grain at the expense of another[1]. The driving force of grain growth is the reduction of grain boundary area, as it is a high energy area.

There are two types of grain growth for porous ceramics, the normal and exaggerated growth. In normal grain growth the grain size is increasing, but the grain size distribution does not change considerably. Moreover, the pores remain attached to the grain boundary, especially for porous ceramics. In contrast, in exaggerated grain growth, a few grains grow very fast, eventually resulting in a bimodal distribution. Pores usually detach from the *GB* and remain inside the grain.

Although these sintering models are important in understanding the sintering process, they are impractical in terms of interpreting the experimental results. Therefore, few numerical and empirical models have been derived to help estimate the sintering kinetics.

2.1.3 Sintering of ionic compositions

The sintering mechanisms mentioned in section 2.1.1 are active in systems where densification and grain growth occur by the movement of single type atoms or point defects of a component, whereas in polycrystalline ceramics, the matter transport may occur by diffusion of ions, or other charged species (point defects) rather than atoms. Accordingly, the type and concentration of defects can be influenced by the mobility and sinterability of ceramics.

There are two types of point defects in ceramics: intrinsic defects, which are formed during crystal growth and their concentration does not change with external influences; and extrinsic defects, which are caused by external influences, such as gaseous atmospheres, additives, etc[36]. Figure 2-4 shows the different types of point defects in an ionic compound. The defects in ceramic structures would carry charges and they may react by ions and other defects[*1]. For instance, annealing metal oxide (MO) in a reducing atmosphere leads to the formation of an oxygen vacancy in the metal oxide structure (MO_{1-x}). In contrast, annealing the same composition in an atmosphere with high oxygen partial pressure induces a metal vacancy ($M_{1-y}O$) in the structure. In both cases the metal oxide seeks to equilibrate its components with the surrounding atmosphere. Solutes (dopants or additives) also change the structure of a ceramic compound by forming solid solutions. For example, Al^{+3} in Al_2O_3 may substitute for Mg^{+2} in MgO and forms vacant sites of Mg in MgO (V''_{Mg}).

As a conclusion, the rate of mass transport is a function of the point defect concentration in ceramic materials, and can be altered by temperature, oxygen partial pressure and dopant concentration. Since there is no clear controlling sintering mechanism for a ceramic compound, the correlation between the defect structure and the sintering rate is not straightforward and

[*] Study of the interactions between defects is not within the scope of this thesis.

accurate. Therefore, the knowledge of defect chemistry may help predict the sintering of ceramic compounds under given conditions.

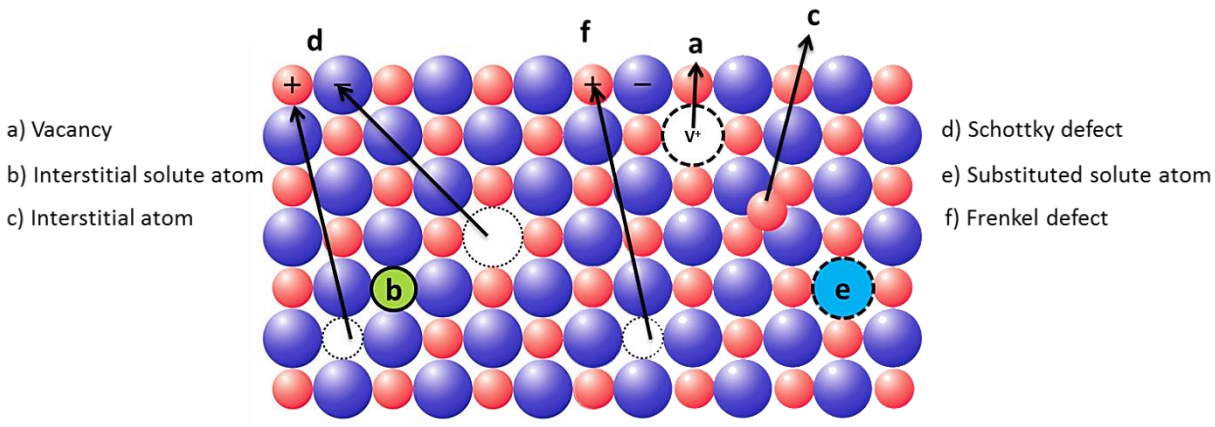

Figure 2-4. Point defects in ionic structures[4]

2.2 Spinel structures

A spinel crystal is a *FCC* arrangement of anions where cations are filling tetrahedral and octahedral sites available between the anions, Figure 2-5. A unit cell of spinel is composed of 56 atoms and includes 24 cations and 32 anions[37,38]. There are two types of cations in a unit cell of a spinel crystal, with two different valences. The general structural formula of a spinel crystal is $A^{X}B^{Y}{}_{2}O_{4}$ where X and Y are the valences of cations; however, it should be mentioned that a spinel unit cell consists of 8 units, with the formula $A_{8X}B_{8Y}O_{32}$.

Type A cations are usually divalent e.g. Mg^{+2}, Zn^{+2}, Ni^{+2}, Fe^{+2}, Mn^{+2}, etc. and fill 8 of the 64 available tetrahedral sites in the spinel crystal. In comparison type B cations are usually trivalent e.g. Al^{+3}, Ti^{+4}, Cr^{+3}, Fe^{+3}, etc. and are usually located at 16 of the 32 available octahedral sites[37,39].

Depending on the valences of cations, two types of spinels are identified, including:

4-2 spinels where X= +2 and Y= +4 e.g. Mg_2TiO_4

3-2 spinels where X= +2 and Y= +3 e.g. $MgAl_2O_4$

A large group of industrially available spinels are crystallized in either type of spinels. For instance, spinels for refractory applications are (but not limited to) $MgAl_2O_4$, $MgFe_2O_4$, $MgCr_2O_4$, Mg_2SnO_4, etc.; for electronic applications include $CoFe_2O_4$, $ZnCr_2O_4$, etc[39].

Spinels with such cation arrangement where divalent and trivalent cations have filled tetrahedral and octahedral sites of a spinel crystal respectively are called normal spinels. However, the position of cations may change in a way that tri or tetravalent cations move to the tetrahedral sites and divalent cations locate into octahedral sites. In a certain situation, half of *B* type cations are located in tetravalent sites, and all *A* type cations are located in octahedral sites. A spinel crystal with this cation arrangement is called inverse spinel[2]. Therefore, the chemical formula of a 3-2 inverse spinel is $B(AB)_2O_4$. In naturally occurring spinels a fraction of cations change their positions between tetrahedral and octahedral sites; thus they are partially inversed. In order to understand the cation distribution in spinels, a general structural formula $^{T}(A_{1-\xi}B_{\xi})^{M}(B_{2-\xi}A_{\xi})O_4$ is being used. In this formula, *A* and *B* refer to the two types of cations, *T* and *M* refer to tetrahedral and octahedral sites respectively and ξ is the inversion parameter[40].

The inversion parameter ξ varies between 0 and 1, e.g. it is 0 for completely normal spinel and 1 for completely inverse spinel. The degree of inversion is a function of temperature, atmosphere, neighboring cation and anions, cation size and the electronic structure of the cation. For example, the inversion parameter (ξ) for $CoAl_2O_4$ is 0.055 at 850°C and 0.15 at 1400°C [41]; this means that higher atomic mobility is present in the Co-Al spinel structure at higher temperature. Thus it can be concluded that the inversion parameter can be used to predict the relative cationic mobility in two spinels. In this regard, understanding the factors that control the inversion parameter is essential.

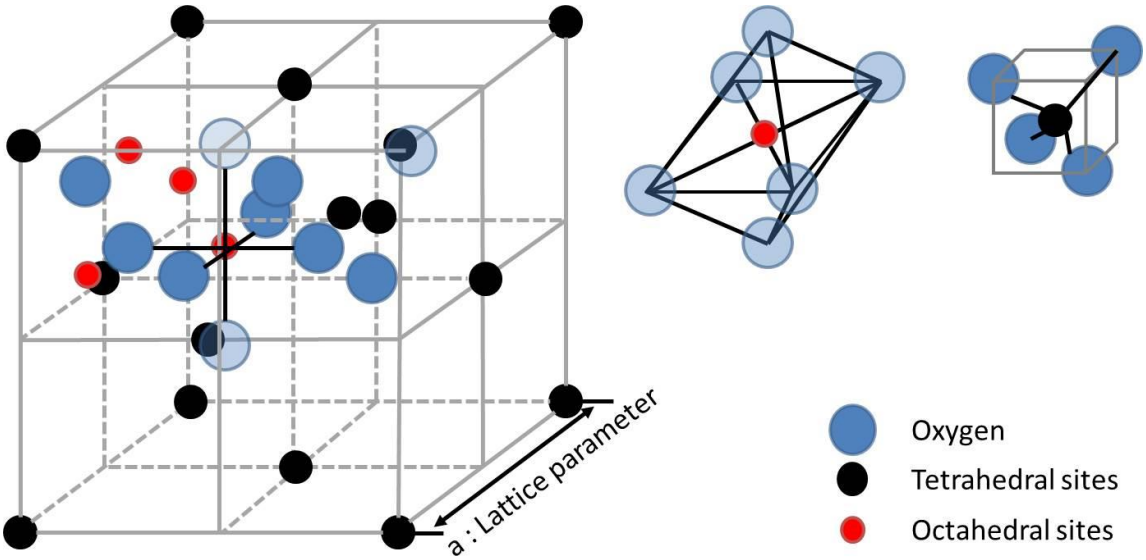

Figure 2-5. Schematic of a spinel crystal[4]

2.2.1 Chromite spinels

Chromite is a mineralogical name for $FeCr_2O_4$; however, it generally refers to any chromium-containing spinels or solid solutions with spinel crystal structure[6]. There are six important chromite end-members including $FeFe_2O_4$ (*FF*), $MgFe_2O_4$ (*MF*), $FeAl_2O_4$ (*FA*), $MgAl_2O_4$ (*MA*), $FeCr_2O_4$ (*FC*), $MgCr_2O_4$ (*MC*); among them, $MgCr_2O_4$, $MgAl_2O_4$ and $MgFe_2O_4$ are stable in harsh environments where high temperature (>1300°C), thermal shock resistance, oxidizing-reducing atmosphere and corrosion resistance against molten slags are necessary. Due to these characteristics, $MgCr_2O_4$, $MgAl_2O_4$, $MgFe_2O_4$ and their solid solutions have been used as refractory materials for more than 50 years.

$MgCr_2O_4$ is a normal spinel (space group Fd3m) with a lattice parameter of 8.333±0.002 Å[42,43] and theoretical density of 4.412 g/cm^3. According to the MgO-$MgCr_2O_4$ phase diagram (Figure 2-6), it is the only compound in this system, and its melting temperature is ~2350°C[44]. At high temperatures and in air atmosphere, the intrinsic defect in $MgCr_2O_4$ is the Cr vacancy, as

reported by Hiroki et al.[45]. Since the formation of Cr vacancies might be due to the evaporation mechanisms, the formed vacancies may improve the self-diffusion rate or the diffusion rates of other cations, but they cannot help the densification rate.

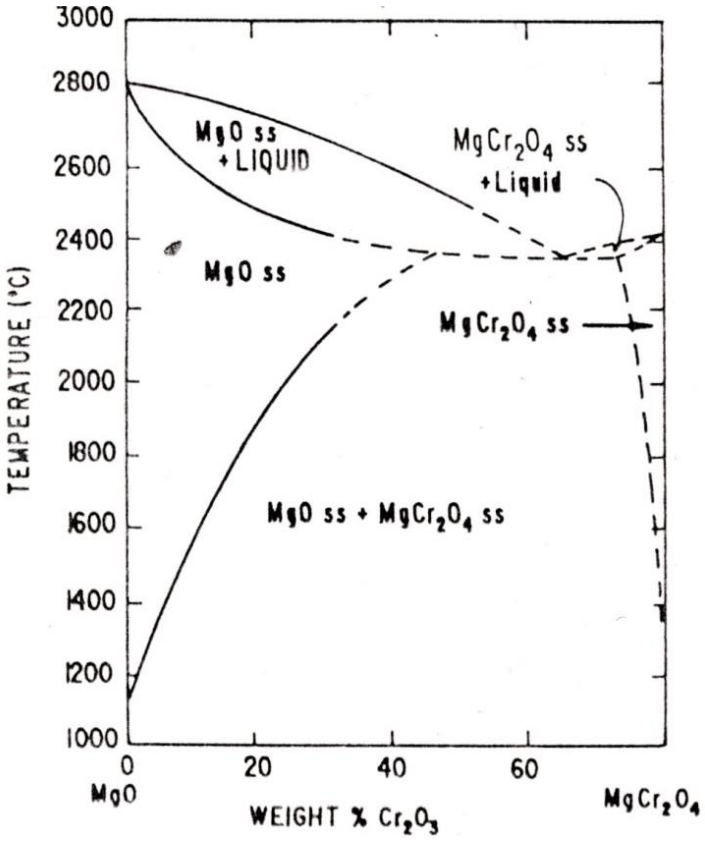

Figure 2-6. MgO-$MgCr_2O_4$ phase diagram[7]

The mechanism of vacancy formation has been was expressed by Kazumatomo[46] as follows:

$$\frac{3}{4}O_2(g) = \frac{3}{2}O_l + V_{Cr}''' + 3h^{\bullet} \qquad 2\text{-}7$$

where $O_2(g)$ is gaseous oxygen, O_l is oxygen lattice and V_{Cr}''' and $h^{\bullet}$ are negatively charged vacancy and electron hole, respectively. Calculating the self-diffusion coefficient of Cr at

different temperatures and partial pressures of oxygen, Kazumatomo demonstrated that self-diffusion was controlled by the Cr vacancies concentration.

$MgAl_2O_4$ is an isostructure of $MgCr_2O_4$ and is a normal spinel (space group Fd3m); its structure is described as a cubic lattice of oxygen atoms with Mg^{+2} occupying 12.5 % of tetrahedral sites and Al^{+3} occupying 50 % octahedral sites[47]. The lattice parameter and theoretical density are 8.0887 Å and the 3.59 g/cm^3 respectively.

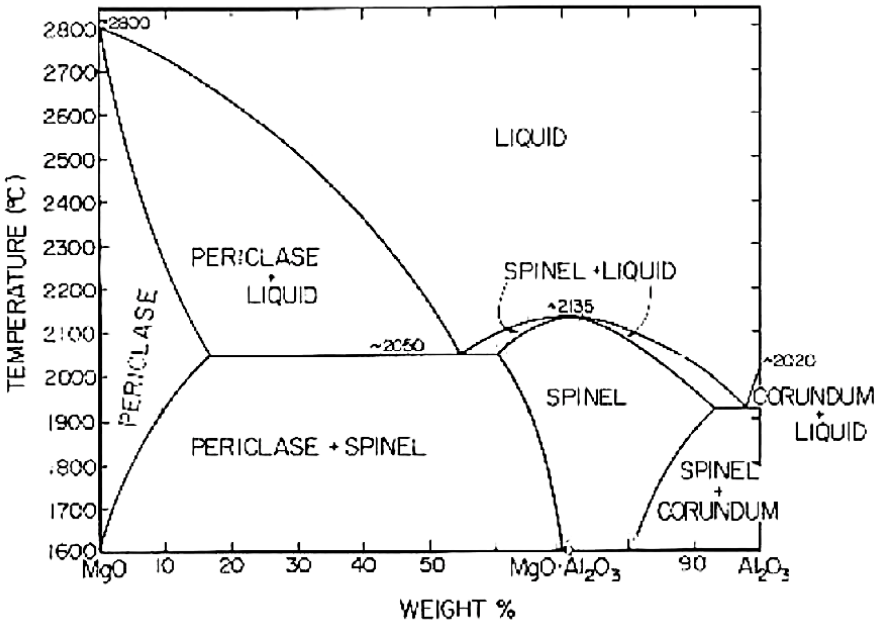

Figure 2-7. MgO-Al_2O_3 phase diagram[8]

As shown in MgO-Al_2O_3 phase diagram (Figure 2-7) $MgAl_2O_4$ is also the only intermediate phase in MgO-Al_2O_3 system and its melting point is about 2135°C. Although $MgAl_2O_4$ and $MgCr_2O_4$ are isostructural compounds, the form different defects. Unlike $MgCr_2O_4$ in which Cr vacancy forms readily at high temperatures, Al vacancy in $MgAl_2O_4$ does not form very easily, due to the high vacancy formation energy (4.76 ev)[45].

However, Murphy[48] reported that the main defect type in stoichiometric $MgAl_2O_4$ spinel is the antisite disorder, as described in equation 2-8, due to the lower formation energy of this process compared to other intrinsic defects. Such charged defects play a significant role in the accommodation of non-stoichiometry, foreign cations and also in the diffusional properties of spinel structure.

$$Mg_{Mg}^{\times} + Al_{Al}^{\times} = Mg_{Mg}^{\bullet} + Mg_{Al}' \qquad 2\text{-}8$$

Like two other chromites, $MgFe_2O_4$ is crystallized in spinel structure but unlike them it is an inverse spinel in which Fe^{+3}occupies tetrahedral sites and Mg^{+2} octahedral sites; the inversion reaction may be triggered by heat[49]. The lattice parameter and theoretical density of $MgFe_2O_4$ are 8.3938 Å[50] and 4.502 g/cm[351] respectively. At temperatures above 1000°C, $MgFe_2O_4$ has an area of stability in the MgO-Fe_2O_3 phase diagram (Figure 2-8), and its maximum melting temperature is ~1750°C. The main defect in the $MgFe_2O_4$ structure is disordering due to the lower octahedral site preference energy of Fe^{+3} than of Mg^{+2}.

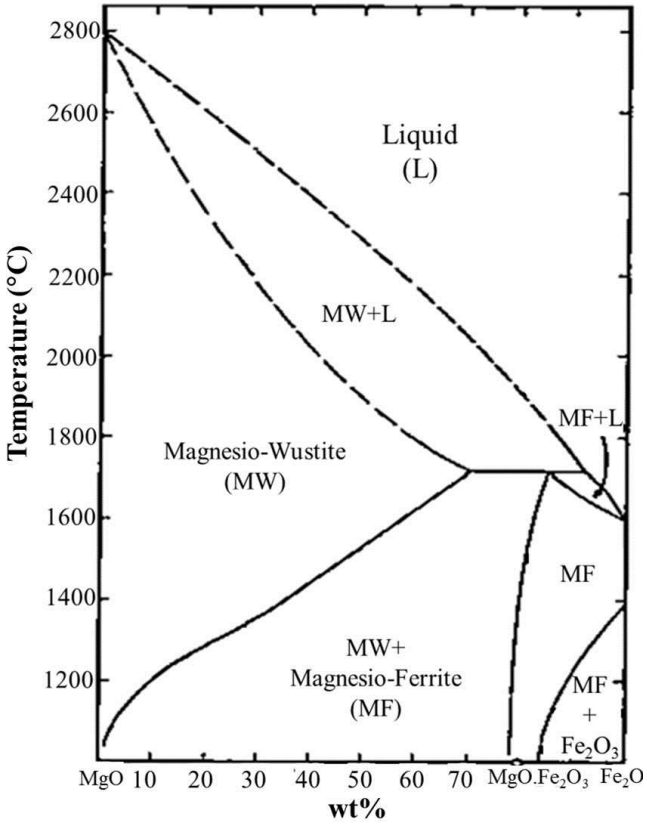

Figure 2-8. MgO-Fe_2O_3 phase diagram[2]

Alper[2] showed that there was unlimited solid solubility between the chromite spinels at temperatures higher than 1000˚C. It was also revealed that the chromite spinels, which are 2-3 type spinels, could also make solid solution with 2-4 spinels. The binary solid solutions of chromite spinels are generally considered as ideal solid solutions, although in few conditions (based on temperature and composition) they behave differently.

Chromite spinels ($MgAl_2O_4$, $MgCr_2O_4$, $MgFe_2O_4$ and their solid solution) have been usually considered as chemically stable compounds, however, their chemical stability is controlled by temperature, partial pressure of oxygen and composition. Ulmer[43] graphically illustrated that the stability of the chromite spinel solid solutions was influenced by the partial

pressure of oxygen. Figure 2-9 is a quaternary phase diagram of MgO-Cr_2O_3-Al_2O_3-Fe_2O_3 at 1300˚C at different oxygen activities.

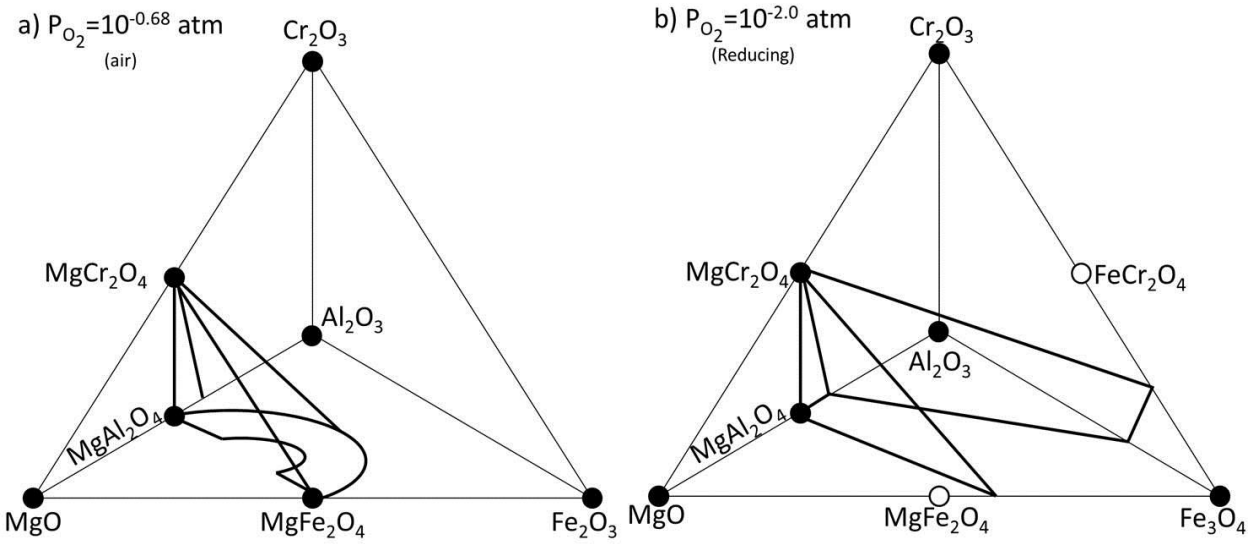

Figure 2-9. Spinel redox stability in MgO-Cr_2O_3-Al_2O_3-Fe_2O_3 at 1300˚C a) in air and b) in reducing atmosphere. Open circles show unstable compounds; closed circles refer to stable compounds; bold lines illustrate the stable chromite spinel solid solutions; reprinted from[2].

As seen in Figure 2-9, in air atmosphere all sesquioxides were stable and iron was stable as hematite. No $FeCr_2O_4$ spinel would form in this condition since it would readily oxidize to parent oxides. Hence, $MgAl_2O_4$, $MgCr_2O_4$, $MgFe_2O_4$, and their solid solutions were stable in the mentioned conditions. Decreasing the oxygen partial pressure on the other hand made $MgFe_2O_4$ unstable and resulted in the hematite transformation into magnetite. In spite of these changes, no change in the stability of $MgCr_2O_4$, $MgAl_2O_4$ and their solid solutions was observed.

Walter[42] reported that high temperature evaporation of Cr_2O_3 in $MgAl_2O_4$-$MgCr_2O_4$ solid solution and dissociation of $MgFe_2O_4$ above 1350˚C in $MgCr_2O_4$-$MgFe_2O_4$ solid solutions

caused deviations from the Vegard's law*. Paladino[52] found that in equilibrated MgO-Fe_2O_3 mixtures, $MgCr_2O_4$ could be stable with hematite. Philips et al.[42] also investigated the phase diagram of MgO-Fe_2O_3 by mineralogical identification process, and found that even at 1500˚C and 1650˚C $MgFe_2O_4$ decomposed into two phases Magnesiowustite (*MW*) + Magnesioferrite (*MF*). Speidel[53] studied the stability of $MgFe_2O_4$ at different temperatures and oxygen activities using *TGA*, and found that the $MgFe_2O_4$ is a single phase up to 1300˚C.

Ulmer et al. showed that the addition of Cr_2O_3 to MgO-Fe_2O_3 mixtures increased the stability of $MgFe_2O_4$, as implied by the reduction in ferrous iron content in response to Cr_2O_3 increase. Walter[42] also found that the addition of $MgCr_2O_4$ into $MgFe_2O_4$ decreased the cell size of the formed solid solution spinel and increased the degree of normality of parent spinel structure. Therefore, it is generally considered that the $MgCr_2O_4$-$MgFe_2O_4$ solid solutions are binary up to 1400°C; however, above this temperature the deviation from binary behavior is significant.

The above review of chromite spinel structures and interactions between them shows that $MgCr_2O_4$, $MgAl_2O_4$, $MgFe_2O_4$ and their solid solution are isostructural; however, depending on the cations involved in the spinel structures, the solid solution between them can be normal or inverse. Since the inversion involves cation mobility and also structural disordering, this phenomenon may affect the diffusion rates and densification behavior. Therefore, understanding the inversion mechanism and cation distribution in spinel solid solutions is essential for the analysis of the sintering mechanisms of spinel solid solutions.

* Vegard's law states that the lattice parameters should vary linearly with composition for a continuous substitutional solid solution in which atoms or ions that substitute for each other are randomly distributed[22].

2.2.1.1 Synthesis of chromite spinels

As described earlier, spinels such as $MgAl_2O_4$, $MgCr_2O_4$ and $MgFe_2O_4$ are categorized as chromite spinel materials. Chromite spinels are important materials due to their physico-chemical properties[54], which them excellent candidates for refractories[55,56], sensors[57], catalysts, etc.

Chromite spinels have been traditionally synthesized by solid state reaction (*SR*), which involves high synthesis temperatures, usually above 1200°C[58,59], resulting in low specific surface area and low reactivity. To avoid these shortcomings, several chemical synthesis techniques have been developed, including the sol–gel method (*SG*)[60,61], co-precipitation (*CP*)[44], solution combustion (*SC*)[19,62], and hydrazine method (*HM*)[61]. The advantage of chemical routes compared to the solid state method was the ability to control the stoichiometry, particle size, and morphology of the synthesized spinel.

The basics of spinel formation have been explained by Wagner's theory[59]: spinel formation initiates at the interface of primary oxides via counter diffusion of cations, and results in the formation of a spinel layer between Cr_2O_3 and MgO. Due to the higher diffusion rate of Mg^{+2} in Cr_2O_3 in comparison to Cr^{+3} in MgO, the spinel layer grows toward Cr_2O_3 and leaves pores (termed "Kirkendall pores"), on the MgO site. The mechanism is schematically shown in Figure 2-10; as seen, the spinel formation is accompanied by volume expansion. This mechanism was also reported by Greskovich[63] for the formation of $MgCr_2O_4$, and by Watson[59] for the formation of $MgAl_2O_4$.

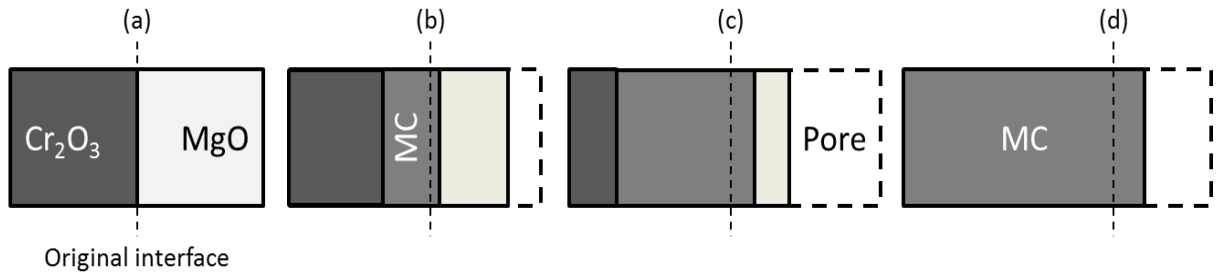

Figure 2-10. The schematic of spinel formation mechanism according to Wagner theory; reproduced from[9]

Dilatometric studies of the reactions between spinel and sesquioxides in air confirmed the reduction of the sesquioxides to spinel at elevated temperatures. The studies also show that the reactions and phase transformations in chromite spinels involve volume change. For example, the isothermal reduction studies by Ulmer[43] and dilatometry studies by Rigby and Culter[64] pointed out where volume increase was observed during the reduction of sesquioxides to spinels. The volume increase was linked to the reduction of Fe^{+3} to Fe^{+2}.

Although redox reactions were considered a reason for volume change in chromite spinels, Rigby[64] introduced the Kirkendall effect i.e. pore formation due to different diffusion rates, as the main reason for such volume changes. Sako et al.[65] also linked the pore formation to the Kirkendall effect during the formation of in situ spinel in Al_2O_3-MgO castables. In fact, larger pores were observed for higher MgO size in the microstructure of samples sintered at 1500˚C for 5 h in air. Moreover, a spinel rim was seen around pores, emphasizing the presence of MgO in the existing pores before the spinel formation. In other words, MgO reacted with Al_2O_3 to form spinel and left a Kirkendall pore behind. The same results were also published by Braulio[9], Yu et al.[66], etc.

Table 2-2. Thermodynamic properties of selected chromite spinels; reprinted from[2]

	ΔG° (1000-1227°C) (kcal/mol)	ΔG (kcal/mol)	ΔH (kcal/mol)	ΔS (cal/K)
$MgCr_2O_4$	$-10.27+1.7\times10^{-3}T$ (±0.5)			
25°C		-9.75±0.5	-9.9±0.5	-0.5
1000°C		-8.10±0.5	-10.3±0.5	-1.7
$MgAl_2O_4$	-			
25°C		-	-	0.53±0.2
1000°C		-8.4	-6.9	+1.1
$MgFe_2O_4$	$-5.75+0.32\times10^{-3}T$ (±0.4)			
25°C		-4.5±0.4	-4.8±0.4	1.1±1
1000°C		-5.34±0.4	-5.75±0.4	-0.3±1

The thermodynamic properties of chromite spinels at 1000°C are summarized in Table 2-2. As seen the ΔG° values for the formation of $MgCr_2O_4$ and $MgFe_2O_4$ are negative, i.e. their formation is thermodynamically favorable. Moreover, the value of free energy of chromite spinels at 25°C and 1000°C indicates that $MgCr_2O_4$ should be the most stable phase both at low and high temperatures; $MgAl_2O_4$ followed by $MgFe_2O_4$ are the two most stable chromite phases after $MgCr_2O_4$. Therefore, understanding the solid solution formation between chromite spinels is essential, as they do not dissociate at high temperature, but react. As a result of the reaction between the chromite spinels, the crystal defects, disordering (cation distribution), and crystal distortion may occur, which affects the diffusional properties and densification behavior accordingly.

2.2.2 Cation distribution in chromite spinels

Spinels are important minerals and industrial materials and have been used as refractory, magnetic and semiconducting materials, and gems. Naturally occurring spinels consist of a variety of cations; the group of spinels which mainly consist of Mg^{+2}, Al^{+3}, Ti^{+4}, Cr^{+3}, Fe^{+2}, and Fe^{+3} are categorized as chromite spinels. Since the type and position of cations involved in spinel

structure considerably change the physical and chemical properties of spinels, the determination of cation distribution is crucial in the characterization and prediction of the properties of either natural or synthetic spinels.

O'Neill and Navrotsky[67] suggested that the inversion parameter describes the cation distribution in the case of binary spinels. Della et al.[68] showed that the inversion parameter affected the static potentials in aluminate and ferrite spinels significantly. Kumar and Abbas[69,70] showed that the magnetic properties in ferrite spinels, governed by super-exchange interactions, depended on the metal cations and their distribution over the two interstitial (tetrahedral and octahedral) sites. Francesco[71] and Giovanni[40] explained that knowledge of cation distribution process in spinels might provide important information on the cooling history of rocks, and elucidate constraints on diamond growth, since spinels were often found as inclusions in diamonds[72].

Cation distribution in spinel solid solution was shown to strongly depend on the composition of the end-member spinels; for instance $MgAl_2O_4$, which has a normal structure over a wide range of temperatures, and $MgFe_2O_4$, which has an inverted structure with Mg^{+2} in the octahedral sites and Fe^{+3} in the tetrahedral sites, form inverted solid solutions [$MgAl_{2-x}Fe_xO_4$ $(0\leq x\leq 2)$][73].

Nakatsuka et al.[20] investigated the cation distribution in $MgAl_2O_4$-$MgFe_2O_4$ solid solutions using single crystal diffraction intensity, and showed that Al^{+3} and Fe^{+3} could occupy both the tetrahedral and octahedral sites. In contrast, Mg^{+2} occupied the tetrahedral sites in the $MgAl_2O_4$ rich compositions and octahedral sites in the $MgFe_2O_4$ rich compositions. Nakatsuka also showed that for the range of compositions $0.7\leq x\leq 1.2$, two spinel phases were stable, implying a probable low temperature miscibility gap between $MgAl_2O_4$ and $MgFe_2O_4$[20]. The same

phenomenon has been reported by Jacob[74] in the MgO-Al_2O_3-Cr_2O_3 system. He demonstrated that the intracrystalline ion exchange was ruled by the site preference energies of the cations, and introduced a critical temperature (T=530±20°C) and a composition ($x_{MgCr_2O_4} = 0.46 \pm 0.02$) above which some phase separation would occur.

Investigating the thermodynamics of complex spinel solid solutions, $(Mg_xFe_{1-x})[Al_yCr_{1-y}]_2O_4$, Jacob and Behera[75] explained that the cation distribution relied on temperature and composition; however, they developed a model predicting the cation distribution independent of these two factors, based on the octahedral site preference energies of the cations.

2.2.3 Sintering of chromite spinels

Sintering of ceramics is the most important stage of ceramic processing, since the properties of the final product, including mechanical, physical, electrical properties, etc., are influenced by the sintering parameters[5]. Sintering of $MgAl_2O_4$ spinels is well documented, due to the enormous potential for $MgAl_2O_4$ application in many industries[1].

Pal et al.[76] showed that there was about 40-50 wt% solubility of alumina in $MgAl_2O_4$ at 1600°C, which reduced rapidly with temperature decrease, implying precipitation of alumina during cooling. In spite of the high solid solubility of alumina in spinel, only 5-10 wt% alumina as a sintering additive is considered optimum[76]. The addition of alumina in the mentioned range resulted in about 25% densification, and ~3.1g/cm^3 bulk density at 1600°C. Although no microstructural evidence was shown in their report, the decreased density and increased open and closed porosity beyond these values were attributed to the precipitation of alumina during cooling.

Bratton[77] has also investigated the initial stage sintering of $MgAl_2O_4$, and demonstrated that the volume diffusion was the controlling mechanism. In order to understand which species

was the rate-controlling one, the self-diffusion coefficients of O^{-2}, Mg^{+2}, and Al^{+3} in $MgAl_2O_4$, Al_2O_3 and MgO were compared to the measured data. It was shown that Al^{+3} and O^{-2} were the rate-controlling species in the initial stage of sintering. In another study, Rozenburg [78] studied the sintering kinetics of $MgAl_2O_4$ and LiF-doped $MgAl_2O_4$, using the master sintering curve techniques (MSC).

It was demonstrated that the addition of a small amount of LiF (0.5 wt%) reduced the activation energy of densification. Figure 2-11 illustrates that increasing LiF up to 1 wt% decreased the densification activation energy from 470 to 190 kJ/mol. The activation energy for LiF-free samples is close to the lattice diffusion of oxygen in spinel, 430-490 kJ/mol, in agreement with Ting and Lu's results[79]. In addition, the activation energy of densification for the LiF-containing samples is very close to the activation energy of formation of $MgAl_2O_4$ in the presence of LiF (165 kJ/mol)[80].

In a former study by Rozenburg[10] it was explained that the reaction between LiF and $MgAl_2O_4$, which resulted in the formation of $LiAlO_2$ and MgF_2, may promote sintering of $MgAl_2O_4$ due to the liquid phase formation. However, the calculated activation energies in the later study proposed that the vacancy formation via the following reaction (Equation 2-9) may be responsible for the reduced activation energy in the presence of LiF. Since sintering process was coupled with diffusion, the increased population of oxygen vacancies would reduce the activation energy.

$$3LiF \xrightarrow{MgAl_2O_4} Li'_{Mg} + 2Li''_{Al} + 3F_O^{\bullet} + V_O^{\bullet\bullet} \qquad 2\text{-}9$$

Bratton[81] also studied the intermediate stage sintering of $MgAl_2O_4$ at 1300-1600°C and showed that volume diffusion was the active sintering mechanism; the activation energy of the

intermediate stage of sintering was 118 kJ/mol, close to that of the initial sintering stage, implying that the same mechanism was responsible for the densification.

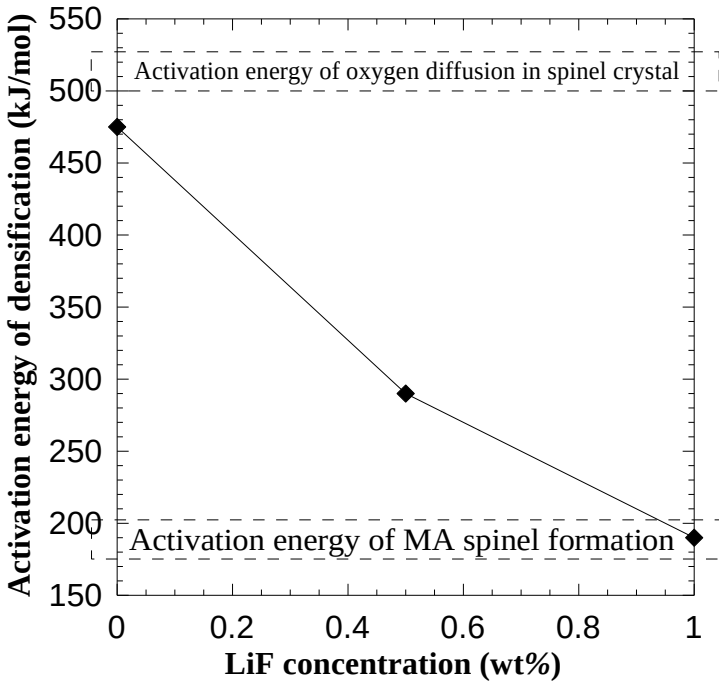

Figure 2-11. The effect of LiF concentration on activation energy of densification of $MgAl_2O_4$; the applied pressure was 33MPa[10].

Investigation of the $MgCr_2O_4$ sintering was initiated by Anderson[82] by studying the influence of the oxygen partial pressure. It was shown that $MgCr_2O_4$ could not densify to more than 70 % of theoretical density even at 1700°C, when the partial pressure of oxygen was higher than 10^{-10} atm, which is close to the equilibrium partial pressure for the following reaction 2-10 ($P_{O_2}^{eq} = 10^{-12}$ atm). Although it was shown that at $P_{O_2} \leq 10^{-10}$ atm the $MgCr_2O_4$ densified to more than 98 % of theoretical density, it was also shown that $MgCr_2O_4$ might dissociate at 1600°C and $P_{O_2} \leq 10^{-13}$ atm.

$$MgCr_2O_4(solid) + 1.5O_2(g) \longrightarrow 2CrO_3(gas) + MgO(solid\ or\ gas) \qquad 2\text{-}10$$

As a result of this decomposition, the small particles become smaller and large particles become larger, leading to $MgCr_2O_4$ grain growth with no densification[82]. The reaction showed in equation 2-10 plays two different roles in the densification of $MgCr_2O_4$: in the initial stages of sintering, the rapid grain growth results in pores entrapment inside grains, and these pores could not be eliminated[82]. In the final stage of sintering, when grains grow through lattice and grain boundary diffusion, the evaporation/condensation increases the grain growth rate more than the densification rate, leading to limited densification. A similar phenomenon was observed in the sintering of the Cr_2O_3 in air[11, 83].

Studying the final stage of sintering of Cr_2O_3, Ownby[11] showed that the densification of Cr_2O_3 was influenced by the oxygen partial pressure, and concluded that the maximum relative density (95%) was obtained when the oxygen partial pressure was equal with the equilibrium partial pressure of oxygen in the following reaction:

$$\frac{4}{3}Cr(solid) + O_2 \longrightarrow \frac{2}{3}Cr_2O_3\ (solid) \qquad 2\text{-}11$$

As shown in Figure 2-12, at P_{O2} higher or lower than $P_{O2}=10^{-12}$ atm (the equilibrium partial pressure for reaction 2-11) the density of Cr_2O_3 decreases considerably; this behavior, according to Graham and Davis[84], is related to the stability of different oxidation states of chromium. Cr^{+3} is the most stable form of chromium oxide, and its oxidation results in the formation of higher oxidation states Cr^{+4}, Cr^{+6}, which evaporate at $PO_2>10^{-3}$ atm as CrO_2 and CrO_3. At $PO_2<10^{-11}$ atm the metallic Cr leaves the sample; in the region between the mentioned pressures, evaporation was governed by the volatilization of CrO and CrO_2.

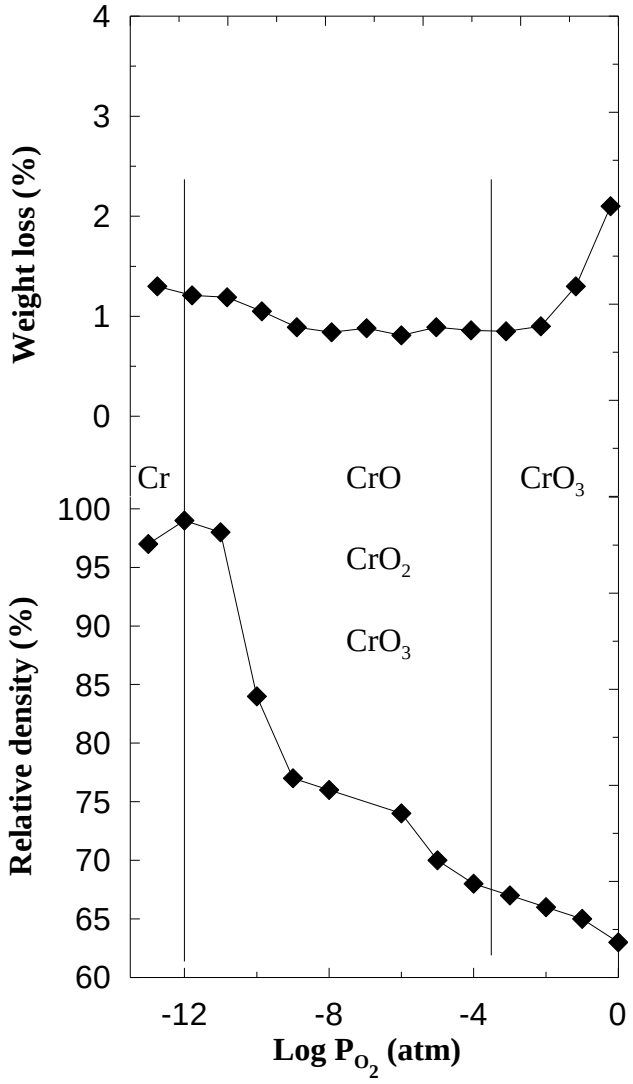

Figure 2-12. PO_2 vs. density and weight loss of pure Cr_2O_3; the dominant species stable at various oxygen partial pressures are also indicated[11].

Ownby et al. added 0.1 wt% and 1 wt% of MgO to retard grain growth during the final stage of sintering. The addition of 0.1 wt% of MgO at $PO_2=10^{-11}$ atm increased the density to 99.8 % of theoretical density, while adding 1 wt% of MgO limited the extent of densification to about 97 % of theoretical density, due to the formation of a continuous layer of $MgCr_2O_4$ at the grain boundary, resulting in reduced atom diffusion.

As reported by Graham[84], Hench indicated that both the volume diffusion, and evaporation and condensation, were responsible for the sintering of Cr_2O_3. It was also shown that Cr^{+3} was the most stable oxidation state of Cr involved in the sintering of Cr_2O_3. Accordingly, the limited densification (relative density <75 %) of Cr_2O_3 in air and O_2 atmospheres was attributed to the volatility of other oxidation states of chromium oxide, such as Cr^{+2}, Cr^{+4}, Cr^{+6}. Roy[85] found that the isothermal sintering of Cr_2O_3 in the presence of MgO was predominantly governed by grain boundary (*GB*) diffusion and simultaneous vapor transport at the sintering temperatures (1350-1500°C).

He also calculated the activation energy of sintering (125-272 kJ/mol) and stated that this very low value, compared to the activation energy for alumina sintering (628 kJ/mol), was caused by the *GB* diffusion as a result of departure of the oxide from the stoichiometric composition. Stone[86] explained that the off-stoichiometry increased the lattice diffusion, which was very important in the sintering of Cr_2O_3. However, both studies pointed out that the role of the initial vapor transport should always be considered in Cr_2O_3. Stone[87,86] investigated the effect of the reducing atmosphere, and found that the Cr_2O_4 layer formed on the Cr_2O_3 surface in oxygen atmosphere would be reduced in the presence of carbon, which resulted in enhanced densification at partial pressure of oxygen lower than 10^{-7} atm.

Hagel et al.[88] studied the initial stage of sintering of Cr_2O_3 in Ar at $PO_2 \sim 10^{-2}$ atm, but they were not able to obtain more than 78 % of theoretical density. They concluded that the volume diffusion of lattice oxygen was the rate controlling factor. J.M. Neve and R. L. Coble[83] studied the initial stage of Cr_2O_3 sintering at 1400°C and various oxygen partial pressures, and the maximum relative density of 75 % was obtained at the same PO_2 as reported by Ownby[11]. Particle coarsening through the evaporation-condensation mechanism in the early stage of

sintering was attributed to poor densification. The results of sintering studies on $MgCr_2O_4$ and Cr_2O_3 show that the volume diffusion, grain boundary diffusion and evaporation-condensation govern the densification process and grain coarsening during sintering.

Several researchers investigated the role of sintering additives on the sintering temperature of $MgCr_2O_4$. Yamaguchi et al.[12] investigated the role of TiO_2 on the densification of $MgCr_2O_4$, and showed that the addition of up to 20 mol% of TiO_2 can increase the extent of densification at 1500°C to 80 %TD in air and 96 %TD in reducing atmosphere. In spite of the limited density of samples sintered in air, the increase in density with increasing TiO_2 content was also observed. Phase evolutions and lattice parameter calculations revealed that in both situations (sintering in air and carbon bed) the added TiO_2 dissolved in $MgCr_2O_4$, although the solubility in air (15 wt%) was less than in reducing atmosphere (30 wt%) (Figure 2-13). The formed solid solution was attributed to the better densification in reducing atmosphere. It was proposed that in reducing atmosphere at 1500°C the $MgCr_2O_4$ was thermodynamically unstable and decomposed by the following reaction:

$$MgCr_2O_4 \longrightarrow 2Cr(s) + MgO(s) + 1.5O_2 \qquad 2\text{-}12$$

Moreover, TiO_3 also became unstable in reducing atmosphere and reduced to TiO_2. In the early stage of sintering, this instability acts as driving force for the higher diffusion rates of cations and enhanced densification. In oxidizing atmosphere, $MgCr_2O_4$ vaporized according to the equation 2-12, and resulted in grain growth through evaporation of Cr species and their condensation on the neck area. This decreased the driving force of sintering and suppressed the densification.

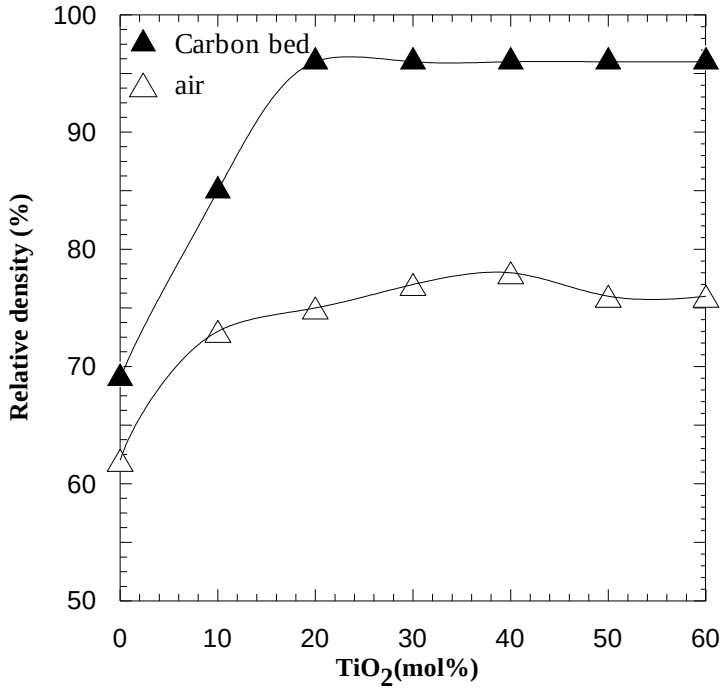

Figure 2-13. Relative density of the samples obtained from $MgCr_2O_4$-TiO_2 compacts by heating in a carbon bed and in air at 1500°C for 2h[12].

Ghosh et al.[13] investigated the effect of magnesia reactivity and unstabilized ZrO_2 on the sintering of magnesia-chrome ceramics. Two types of magnesia grains with 95 wt% purity and different grain sizes (sintered magnesia with 1 m^2/g) and caustic magnesia with 13.5 m^2/g) were used. The chromium oxide was provided by chrome ore, which contained Cr_2O_3:62 wt%, MgO:15 wt%, Fe_2O_3:12 wt% and Al_2O_3:10 wt%. Figure 2-14 shows the variation of bulk density and apparent porosity of magnesia-chrome samples sintered at 1700 and 1750°C versus the ZrO_2 content.

Regardless of the type of magnesia grains, the addition of zirconia progressively increased the bulk density and decreased the apparent porosity of the magnesia-chrome samples. However, the bulk density of the compositions made with caustic magnesia was considerably lower than the one with sintered magnesia. Sintering was accompanied by spinel formation along with densification. Therefore, since caustic magnesia was finer than sintered magnesia, spinel

formation was enhanced, which delayed densification. The authors correlated the densification with the effect of ZrO_2 on changing the grain boundary of magnesia-chrome samples, which decreased the dihedral angle. According to the investigation by Halder[89], it appears that ZrO_2 decreases the dihedral angle in the magnesia chromite spinel, which facilitates the direct bond (grain-grain contact) formation.

As shown in Figure 2-14, increasing the sintering temperature to 1750°C did not increase the density in samples containing caustic magnesia and 5 wt% ZrO_2, but decreased the apparent porosity. Unfortunately, the authors did not explain these observations; hence the mechanism which resulted in this behavior must be further investigated. Moreover, the hot modulus of rupture at 1300°C was also evaluated. As seen in Figure 2-15 the HMOR increased about 80% in samples containing 5 wt% ZrO_2 compared to the samples without ZrO_2. This behavior is correlated with increased densification as well as the grain-to-grain bonding, due to the ZrO_2 addition. In both cases the HMOR rose progressively by increasing the ZrO_2 content, and reached a plateau at 3 %ZrO_2.

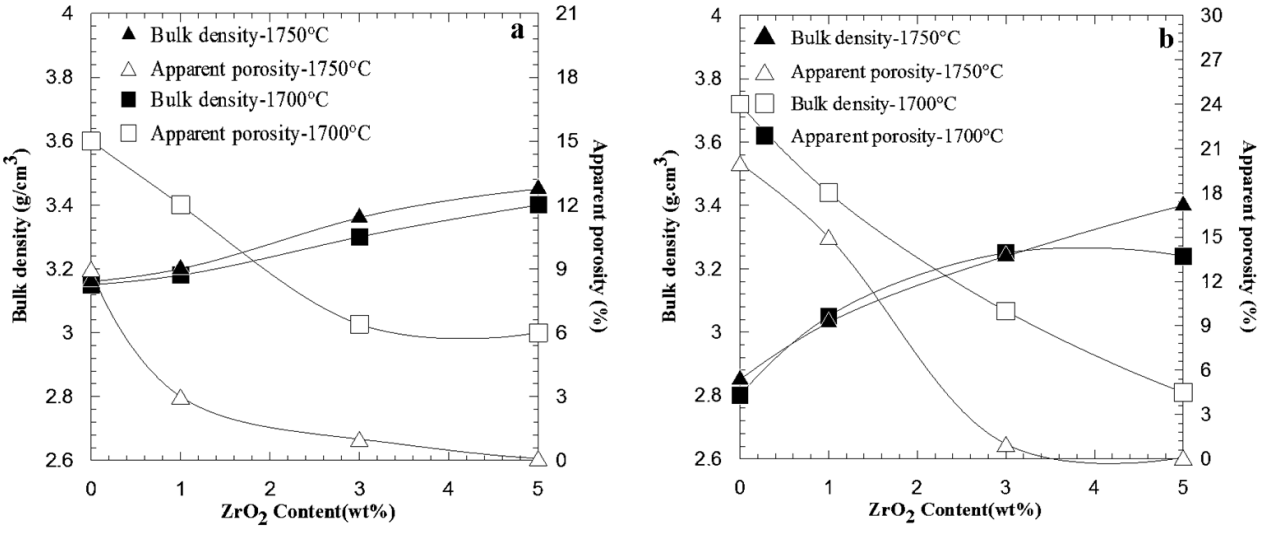

Figure 2-14. Bulk density and apparent porosity of magnesia-chrome grains developed from a) sintered magnesia, b) caustic magnesia[13].

It can be concluded that higher amounts of ZrO_2 increase the direct bond between magnesia-magnesia or chrome grains, which resulted in improved high temperature strength. The temperature influenced more the samples containing caustic magnesia grains than the ones with sintered magnesia grains; also, the rate of increase in *HMOR* with increasing ZrO_2 for the samples containing sintered grains was higher than that of the ones with caustic magnesia grains[13]. This behavior correlates well with the spinel formation rate in caustic magnesia grains and sintered magnesia grains. In fact, the smaller crystal size of caustic magnesia grains compared to that of sintered magnesia grains resulted in higher activity of caustic grains and higher spinel formation rate compared to sintered magnesia grains. The same results have been reported for the hot modulus of rupture (*HMOR*) by Singh[14].

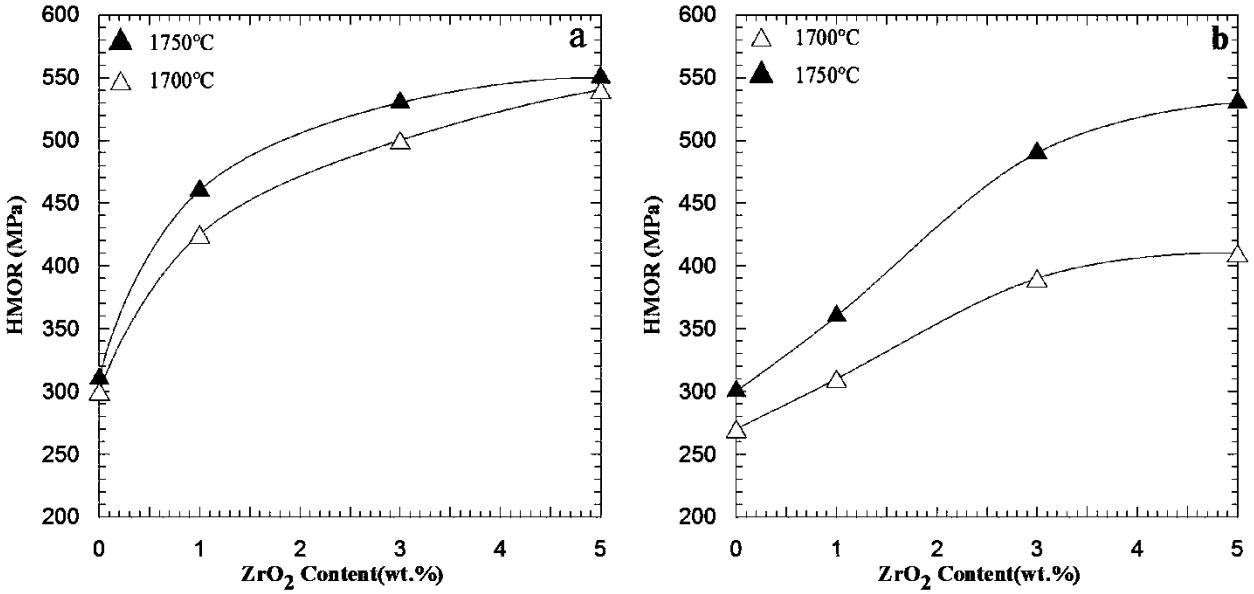

Figure 2-15. *HMOR* of magnesia-chrome aggregates developed from a) sintered magnesia and b) caustic magnesia[14].

Zhao[90] studied the addition of nano Fe_2O_3 into the matrix of magnesia-chrome ceramics and reported that the sintering temperature was reduced by about 150°C. The bulk density of samples containing 1.5 wt% nano Fe_2O_3 sintered at 1550°C (3.06 g/cm^3) was 0.7 % higher than

that of samples without nano Fe_2O_3 (3.04 g/cm^3). It was also shown that the amount of nano Fe_2O_3 up to 2 wt% progressively increased the *CCS* (cold crushing strength) and *MOR* (modulus of rupture) at every sintering temperature. For instance, *MOR* of the samples sintered at 1550℃ (6.5 MPa) was considerably higher than that obtained in samples without nano Fe_2O_3 (4.75 MPa).

Recently, Azhari et al.[56] found that adding nano iron oxide can enhance the formation of magnesioferrite spinel at temperatures as low as 1350°C compared to 1550°C for samples without nano Fe_2O_3. The dilatometry results showed that the onset sintering temperature, where the shrinkage started, was ~1150°C for samples without nano Fe_2O_3 and it was ~1100°C for samples containing 4 wt% nano Fe_2O_3. The low sintering temperature of the samples containing nano Fe_2O_3 was attributed to the decrease in the dihedral angle between magnesia grains.

To the best of our knowledge, there is very limited information about the application of nano particles to lower the sintering temperature of Cr_2O_3 containing ceramics. Moreover, existing sources are only limited to the application of nano Fe_2O_3, with no mechanism being proposed by the authors. Reviewing the literatures on sintering $MgCr_2O_4$ also indicates that there is a lack of studies on the lattice changes during the densification of $MgCr_2O_4$ and $MgCr_2O_4$ containing composites. Information on the lattice changes during sintering would help us evaluate transformation assisted sintering, which could considerably reduce $MgCr_2O_4$ and $MgCr_2O_4$ composite sintering temperatures. Reducing the sintering temperature of $MgCr_2O_4$-containing composites is very important for steel and non-ferrous industries, where they are extensively being used as refractory linings.

Chapter 3. Research scope and objectives

Sintering of magnesia-chromite refractory composites ($MgO\text{-}MgCr_2O_4$), is currently a viable process to make ceramics for refractory linings in non-ferrous metal smelting and refining furnaces. The goals of sintering of the magnesia-chromite refractory composites are to (i) achieve significant densification (i.e. 85-95% relative density) and (ii) to achieve engineered microstructure of a desired phase composition, with the highest $MgCr_2O_4$ content which can withstand the harsh working environments. The challenge of processing magnesia-chromite refractory composites is the required high sintering temperature (~1750°C) that increases the complexity of the production processes and costs. While much attention has been paid to sintering of Cr_2O_3, there are only a few recent publications addressing the sintering and densification of magnesia-chromite refractory composites[19, 91].

The broad goal of the present work was to determine the kinetics of sintering and microstructural development of magnesia-chromite refractory composites and based on these results, to reduce their sintering temperature below 1500°C in air. Within this broad scope, the specific objectives of this research were as follows:

1. Investigation of the influence of trivalent ions (used as Al_2O_3, Fe_2O_3) on the sintering behavior of $MgCr_2O_4$.

2. Study of the effects of the spinel-forming tetravalent metal oxide (SnO_2) as sintering additives, on the sintering behavior and crystal structure of the $MgCr_2O_4$.

3. Investigation of the role of the inversion phenomenon on the densification of $MgCr_2O_4$ by comparing the effects of SnO_2 and Fe_2O_3 on the densification of $MgCr_2O_4$ and Cr_2O_3.

4. Study of the effect of Al_2O_3 and Fe_2O_3 as spinel forming sintering additives on the densification of magnesia-chromite refractory composites.

5. Investigation of the sintering mechanisms of micron sized and nano sized magnesia-chromite refractory composites, in particular the kinetics of sintering of the nano and micron sized magnesia-chromite refractory composites to understand the sintering rate controlling mechanisms.

The following activities have been carried out within the scope of this research in order to address the above objectives:

- The effects of the sintering additives including Fe_2O_3, Al_2O_3, and SnO_2 on the formation and the densification of $MgCr_2O_4$ were investigated by simultaneous thermal analysis (STA: *DSC*/*TGA*). To explain the mechanism through which the sintering additives affected the densification of $MgCr_2O_4$ their influence on the $MgCr_2O_4$ unit cell including the lattice parameter and cation distribution (inversion degree) were investigated based on the *XRD* method.
- The effects of the Cr_2O_3, Fe_2O_3 and Al_2O_3 on the densification of magnesia-chromite refractory composites were investigated by comparing the microstructure and densification results of 12 compositions called *MKi* ($1 \leq i \leq 12$). The composition with the density above 95% at the lowest sintering temperature was considered as the best composition and was used for sintering kinetics studies.
- The best composition of magnesia-chromite refractory composites powders was synthesized with two different particle sizes via two different methods including (i) sol-gel (termed "nano" magnesia-chromite refractory composite powders (*NMK*)) and (ii) conventional powder processing (termed "micro" magnesia-chromite composite powders (*MK*)). The powders synthesized by these two methods had average particle sizes of ~20 nm and ~1.27 μm respectively. The phase analysis,

microstructure and particle size of prepared composites were investigated by *XRD* and *SEM*.

- The densification and the kinetics of sintering the synthesized *NMK* and *MK* composites were investigated via isothermal sintering techniques. The composite powders were pressed uniaxially and sintered at different temperatures (950-1750°C), for various durations (20-300 minutes) in air. The densification behavior of magnesia-chromite refractory composites has been investigated by comparing the density and the microstructure of the sintered composites. The activation energy of sintering was calculated based on the isothermal sintering technique results and applying the master sintering curve theory on the data.
- The best magnesia-chromite refractory composition, selected according to the criterion of the maximum density (~95 % of theoretical density) at optimum microstructure, was used as a binding system in refractory brick samples containing additionally fused mag-chrome grains. The bricks were sintered at 1475°C for 5 hours. The physical and mechanical properties of the bricks were used to estimate their in-field performance.

It is anticipated that the findings of this project will contribute to the fundamental understanding of sintering magnesia-chromite composites, and will also provide the Canadian non-ferrous industry with a new technology for the low-temperature sintering of magnesia-chromite composites.

Chapter 4. Experimental

4.1 Introduction

This chapter describes in detail the techniques and procedures employed to study the sintering of magnesia-chromite refractory composites. The role of Al_2O_3, Fe_2O_3, and SnO_2 on the formation and the densification of pure $MgCr_2O_4$ were first thoroughly investigated. To understand the effects of the inversion phenomenon on the sintering of $MgCr_2O_4$, the densification results of Cr_2O_3-Fe_2O_3 and Cr_2O_3-SnO_2 were compared with $MgCr_2O_4$-SnO_2 and $MgCr_2O_4$-Fe_2O_3.

Based on the results of the above experiments with the intension of designing a refractory grade magnesia-chromite composite, 12 compositions (called *MKi*; $1 \leq i \leq 12$) were designed in order to investigate the effect of the Fe_2O_3, Cr_2O_3 and Al_2O_3 on the densification of magnesia-chromite refractory composites. The composition with the relative density above 95% at the lowest sintering temperature and time was considered as the best composition and used for sintering kinetics analysis. The best composition was synthesized in two particle sizes, 1.27 µm and 20 nm. The micron and nano sized composite powders were called *MK* and *NMK* composites and were used to study the sintering kinetics and understand the sintering mechanism of magnesia-chromite refractory composites and optimize their sintering conditions, including time, temperature, and additives, as well as to produce refractory grade magnesia-chromite refractory composites at temperatures below 1500°C in air.

4.1.1 Synthesis of doped and undoped $MgCr_2O_4$ spinels

These materials were prepared in order to study the effect of trivalent (Al_2O_3 and Fe_2O_3) and tetravalent oxide (SnO_2) in the densification of $MgCr_2O_4$, to test our hypothesis that Fe_2O_3 or Al_2O_3 induces inversion in the $MgCr_2O_4$ lattice. Analytical grade magnesium nitrate hexahydrate ($Mg(NO_3)_2.6H_2O$, purity >99.9%), chromium nitrate nonahydrate ($Cr(NO_3)_3.9H_2O$, purity >99.9%), aluminum nitrate nonahydrate ($Al(NO_3)_3.9H_2O$, purity >99.9%) and ferric nitrate nonahydrate ($Fe(NO_3)_3.9H_2O$, purity >99.9%), and nano tin oxide (SnO_2, purity> 99.9%) have been used as raw materials, in order to minimize the introduction of impurities during processing. The required amounts of raw materials were dissolved in 100 cm^3 of distilled water.

The solution was stirred at 400 rpm and evaporated until the formation of a dark "spongy" mix of salts that was later dried at 250°C for 24 hours and calcined at 850°C for 6 hours, in order to form synthetic powders. The average particle size of such processed oxides was determined through *SEM* observations to be about 0.7 μm. The general formula of these specimens is $Mg[Cr_{1-x}Me_x]_2O_4$, where x is the amount of Me cation (Me = Al, Fe, Sn) replacing chromium, and varies between 0 and 0.2 with 0.05 mol% intervals. It has been verified that in all cases the whole amount of magnesia used reacted with the sintering additive to form spinel.

Based on the results of analyzing the effect of sintering additives on the sintering of $MgCr_2O_4$, and the intention of designing a magnesia-chromite composite for refractory applications 12 compositions called *MKi* ($1 \leq i \leq 12$) were designed and synthesized following the same procedure. The chemical compositions of all the synthesized samples are presented in Table 4-1.

4.1.2 Synthesis of nano magnesia-chromite refractory composites

These sets of samples were prepared to investigate the effect of particle size on the densification of *MK* composites. Nano-particles of *MK* composites were prepared via Pechini's method[15]. Magnesium nitrate hexahydrate ($Mg(NO_3)_2.6H_2O$, purity >99.9%), chromium nitrate nonahydrate ($Cr(NO_3)_3.9H_2O$, purity >99.9%), aluminum nitrate nonahydrate ($Al(NO_3)_3.9H_2O$, purity >99.9%) and ferric nitrate nonahydrate ($Fe(NO_3)_3.9H_2O$, purity >99.9%), citric acid ($C_6H_8O_7 \cdot H_2O$), and ammonia solution (NH_4OH, 30%) were used as the starting materials. All starting materials were purchased from Fisher Scientific Ltd. The required amounts of raw materials were first dissolved in 100 ml of distilled water. Then citric acid was added to the solution, with the ratio of citrate to metal ions of 0.5:1. Citric acid plays two major roles: (1) as a chelating agent it binds metal ions and preserves them from precipitation during pH changes (the schematic of chelation mechanism is shown in Figure 4-1); (2) as a fuel, owing to the presence carbohydrate chains in its structure, burns fast in air and generates heat, thus reducing the synthesis temperature.

In order to increase the efficiency of citric acid as a chelating agent, pH of the solution was adjusted to 6 by adding ammonia[92]. The solution was homogenized for half an hour on a hot plate while mixing with a magnet stirrer, and then it was heated to achieve evaporation of water and formation of a concentrated viscous solution. The solution was heated at 200°C for 24 hours. As a result, a dark brownish sponge-like precursor formed; this was pulverized with pestle and mortar and calcined at 850°C in order to form a nano size magnesia-chromite refractory composite.

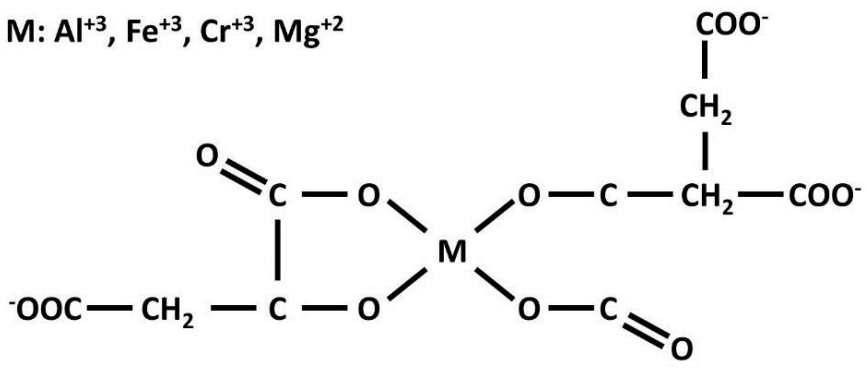

Figure 4-1. Schematic of chelation mechanism during synthesis of *MKi* composite[15]

It is expected that due to the chelating effect of citric acid, the particle size remains in the range of nano size, and in fact a particle size in the range of 20 nm was obtained. With respect to the formation of the sol and gel during the Pechini's synthesis procedure, Jeng[92] reported that during heating, a polyacrylamide network would form in the primary sol at 120°C. Further heating melts the citric acid at about 173°C and convert it to aconitic acid, then itaconic acid, which undergoes polymerization and swells with the decarboxylation at higher temperatures[60]. Since the decarburization at high calcination temperature involves CO_2 evolution, the resulting powder would form soft agglomerates.

4.1.1 Preparation of green ceramic bodies

In all cases except for the laboratory scale bricks, the calcined powder was de-agglomerated using pestle and mortar, mixed with 5 wt% polyvinyl alcohol (*PVA*) solution, and subsequently pressed uniaxially to form cylindrical specimens, 14 mm in diameter and 2-4 mm in height. The compaction pressure was selected on the basis of achieved maximum density of pressed composites sintered at 1500°C for 2 hours.

Table 4-1.The summary of starting powders compositions

	MgO (mol%)	Al_2O_3 (mol%)	Cr_2O_3 (mol%)	Fe_2O_3 (mol%)	SnO_2 (mol%)
$Mg[Cr]_2O_4$	50		50		
$Mg[Cr_{0.95}Fe_{0.05}]_2O_4$	50		47.5	2.5	
$Mg[Cr_{0.9}Fe_{0.1}]_2O_4$	50		45	5	
$Mg[Cr_{0.8}5Fe_{0.15}]_2O_4$	50		42.5	7.5	
$Mg[Cr_{0.8}Fe_{0.2}]_2O_4$	50		40	10	
$Mg[Cr_{0.95}Al_{0.05}]_2O_4$	50	2.5	47.5		
$Mg[Cr_{0.9}Al_{0.1}]_2O_4$	50	5	45		
$Mg[Cr_{0.85}Al_{0.15}]_2O_4$	50	7.5	42.5		
$Mg[Cr_{0.8}Al_{0.2}]_2O_4$	50	10	40		
$Mg[Cr_{0.95}Sn_{0.05}]_2O_4$	50		47.5		2.5
$Mg[Cr_{0.9}Sn_{0.1}]_2O_4$	50		45		5
$Mg[Cr_{0.85}Sn_{0.15}]_2O_4$	50		42.5		7.5
$Mg[Cr_{0.8}Sn_{0.2}]_2O_4$	50		40		10
Cr_2O_3-2.5Fe_2O_3			97.5	2.5	
Cr_2O_3-5Fe_2O_3			95	5	
Cr_2O_3-7.5Fe_2O_3			92.5	7.5	
Cr_2O_3-10Fe_2O_3			90	10	
Cr_2O_3-2.5SnO_2			92.5		2.5
Cr_2O_3-5SnO_2			95		5
Cr_2O_3-7.5SnO_2			92.5		7.5
Cr_2O_3-10SnO_2			90		10
MK	83.5	6.9	6.9	2.7	
NMK	83.5	6.9	6.9	2.7	
MK1	85.49	6.9	2.71	4.9	
MK2	84.49	6.9	2.71	5.9	
MK3	83.49	6.9	2.71	6.9	
MK4	82.49	6.9	2.71	7.9	
MK5	81.49	6.9	2.71	8.9	
MK6	85.49	4.9	2.71	6.9	
MK7	84.49	5.9	2.71	6.9	
MK8	82.49	7.9	2.71	6.9	
MK9	81.49	8.9	2.71	6.9	
***MK*10**	81.49	6.9	3.71	6.9	
***MK*11**	82.49	6.9	1.71	6.9	
***MK*12**	84.49	6.9	0.71	6.9	

The influence of green density on the densification of composites has been discussed in Section 5.1. All compositions have been pressed with the same pressure of 120 MPa, since the same materials with similar particle size and particle size distribution (except *NMK*) have been used in all experiments. The difference between composites is limited to their compositions.

To prepare the specimens for the sintering studies, all formed pellets were heat treated at 850°C for 1 hour and furnace cooled to assure a complete dissociation of *PVA* and burning of the residual carbon from *PVA*[58,93]. To minimize moisture absorption by the pellets, they were kept at 150°C before sintering.

4.2 Sintering of ceramic bodies

In order to study the effects of Fe_2O_3, Al_2O_3 and SnO_2 the sintering of $MgCr_2O_4$, pellets made of $Mg[Cr_{1-x}Me_x]_2O_4$ compositions were heated in a box furnace with 5°/min up to the sintering temperatures (1250-1500°C with 50°C intervals), soaked for 2 hours and cooled inside the furnace to room temperature. From each composition, one specimen was air quenched to room temperature after being soaked at the sintering temperature, to preserve the phase composition and the microstructure at the sintering temperature. This enabled us to determine any changes taking place during materials cooling, to calculate the inversion parameter at the sintering temperature and to correlate it to the sintering behavior of $MgCr_2O_4$ spinel.

A series of isothermal sintering experiments was carried out to study the densification and grain growth of magnesia-chromite refractory composites. The isothermal sintering was conducted at 850-1600ºC with 50°C intervals. The temperature of the furnace was first increased to the desired sintering temperature, and the pellets were placed in the hot furnace for 20, 70, 180 and 300 minutes. The samples did not show any signs of thermal shock experience in this process, as no micro cracks were observed on the surface and cross section of sintered samples. The samples used for each condition were air-quenched to preserve the high temperature structure, for the phase evolution. The characteristics of the sintered samples were determined and used for the sintering mechanism analysis, as described in the following sections.

The densification behavior of magnesia-chromite refractory composites was evaluated both non-isothermally and isothermally. As described in section 4.2, each data point including density, grain size, porosity, etc. is representative of an average value for 3 samples quenched from the sintering temperature. This indicates that all sintering experiments were performed isothermally, but some of the results were reported in the form of non-isothermally collected data.

4.3 Materials characterization

4.3.1 Density, water absorption and apparent porosity

Polished samples were used for bulk density (*BD*), water absorption (*WA*), and apparent porosity (*AP*) measurements, using the Archimedes immersion test. The test was performed on the furnace-cooled sintered samples. The weight of the dry samples (W_d) was measured first.

The samples were impregnated with a wetting agent solution (Kerosene; ρ_k: 0.78 g/cm^3) in a vacuum chamber for 2 hours, to ensure that all pores were filled with the solution. The impregnated samples were then suspended in the solution and the immersed weight (W_i) was measured. The samples were removed from the solution and wiped with a piece of kerosene-saturated paper, to ensure that the excess solution was removed only from the surface, but not from the surface pores. The weight of the kerosene-saturated samples (W_w) was then measured quickly. All density measurements were performed at room temperature. The bulk density, water absorption and apparent porosity were calculated using the equations 4-1 to 4-3 respectively:

$$BD = \frac{W_d \times \rho_k}{W_w - W_i} \qquad 4\text{-}1$$

$$AP = \left[\frac{W_w - W_d}{W_w - W_i}\right] \times \rho_k \times 100 \qquad 4\text{-}2$$

$$WA = \frac{W_w - W_d}{W_d} \times 100 \qquad 4\text{-}3$$

The standard error of the density determination was about ± 0.1%. In order to compare the results, the relative density (*RD*) was calculated by dividing the measured bulk density by the theoretical density of the composition. The theoretical density of each composition was calculated from the *XRD*-determined unit lattice parameter for the samples sintered at 1500°C and quenched in air. It was assumed that the microstructure consists of a single phase spinel solid solution, with no excess spinel-forming oxides. This assumption was *XRD*-validated for all the samples sintered above 1250°C. The calculated theoretical densities of all compositions used in the present study are presented in Table 4-1.

4.3.2 X-ray diffraction

Phase analyses were performed on pulverized specimens (d< #200 mesh) using a Rigaku-Multiflex X-ray diffractometer (Tokyo, Japan), with Cu-Kα radiation (λ: 0.154056 nm) functioning at a voltage and current of 40 kV and 20 mA respectively. The *XRD* patterns were built from data collected for 2θ in the 15-80 degrees range, with a scan rate of 0.5 degree per minute. All the X-ray diffraction (*XRD*) patterns were analyzed with the JADE program for phase identification.

4.3.2.1 Lattice parameter measurement

The lattice parameter was calculated using the following equation.

$$a = \frac{\lambda(h^2 + k^2 + l^2)^{1/2}}{2\,sin\,\theta} \qquad 4\text{-}4$$

where λ is the wavelength of the incident beam (0.1542 nm), h, k, and l are the plan indexes and θ is the Bragg's diffraction angle.

4.3.2.2 *XRD* density measurement

Knowing the value of the unit cell and the number of atoms per unit cell, the theoretical density of samples was calculated as follow:

$$\rho_{th} = \sum AM/NV \qquad 4\text{-}5$$

where ΣA is sum of the atomic weights of the atoms in the unit cell, *M* is molecular weight of sample, *N* is the Avogadro number, and *V* is the volume of unit cell. The *XRD* data was used for inversion parameter measurements as detailed in section 5.2.

4.3.3 Scanning electron microscopy

Due to the non-conductivity of the samples, they were coated with 5 nm of gold using a spattering machine to prevent the charging effect caused by the ceramics and electron beam interactions. The microstructures were then studied using a scanning electron microscope (*SEM*, Hitachi S-3000N, Japan) with an accelerating voltage of 15 kV. The average grain size (*G*) was measured based on the conventional image analysis technique of the linear intercept method (ASTM E112)[95]. For each sample at least three images were assessed by drawing 5 line segments. The average grain size of the sintered samples (*G*) was determined by multiplying the average linear intercept by 1.571[96].

4.3.4 Simultaneous thermal analysis (*STA*)

To determine the activation energy (E_a) for the $MgCr_2O_4$ spinel formation in the presence of sintering additives, 25 mg of precursors were used for *STA* analysis. The precursors were heated to 900°C in air with three different heating rates (10, 20 and 25°/min) using PerkinElmer

STA 6000. The data was fitted to the Kissinger[106] model in order to find the activation energy of spinel formation.

$$ln(T_P^2/\emptyset) = E_a/RT_P + constant \quad (4\text{-}6)$$

where ϕ is heating rate, T_p is the temperature of the maximum *DSC* formation peak and *R* is the universal gas constant. The activation energy (E_a) was calculated from the slope of the plot of $\ln(T_P^2/\emptyset)$vs. $1/T_P$.

4.3.5 Thermal etching

The sintered samples were polished using 6 and 1 micron diamond solutions, and returned to the box furnace for thermal etching to reveal the grain boundaries. This was accomplished at a temperature 50-300°C lower than the sintering temperature, for a short duration of 15 minutes in air. Both the heating and cooling rates for the etching treatment were 10°C/min.

4.3.6 Dimension change and weight loss

The dimensions were measured by a digital caliper with the precision of ±0.001 mm. The weight loss was measured with the precision of ±0.001 g.

Chapter 5. The influence of spinel forming oxides on sintering of $MgCr_2O_4$

5.1 The influence of green density on sintering process

It is well known that the processing of primary powders before sintering significantly affects the densification and the physical properties of sintered ceramics[97,98]. Krell et al.[98] sintered submicron alumina grains and showed that the conventional sintering of submicron alumina was affected by the shaping procedure. They compared the density of uniaxially pressed submicron alumina with the density of the same composition shaped by *CIP* (Cold Isostatic Pressing) in addition to uniaxial pressing. It was shown that addition of *CIP* shaping procedure reduced the sintering temperature from 1450°C to 1400°C and also increased the final density from 98% to 99%. The enhanced densification was attributed to the higher homogeneity of particle coordination in the *CIP* processed specimens.

In the present study, the uniaxial pressing has been used to form pellets for densification studies. As shown in Figure 5-1, no considerable change in both the green and sintered densities was observed at compaction pressure of above 120 MPa. Due to the similarity between the pressing pattern of magnesia chromite refractory composites and other samples, only the variation of density versus compacting pressure for the best magnesia-chromite refractory composite (*MK*) is presented. In the case of *NMK* composites, which were made of nano composite particles, cracks in specimens were observed at compacting pressures higher than 100 MPa. It is expected that the very small particle size of *NMK* sample (<20 nm) generates large friction forces between the nano sized particles[99,100], which limits the particle rearrangement, resulting in a very low green density of 35%±0.1%. Increasing the compaction pressure in this

situation increases the stress and eventually forms cracks in the compact. Figure 5-1 also shows that the final density of the *MK* composite is affected by their green density, as also reported by others. Woolfrey[101] showed that the final density of UO_2 powder decreased considerably for the compacts with green densities below 40%. He related this behavior to a critical value of the ratio of pore size to the particle size, above which pores stabilized and inhibited local shrinkage. He also showed that the green density did not change the sintering mechanism and the activation energy of sintering.

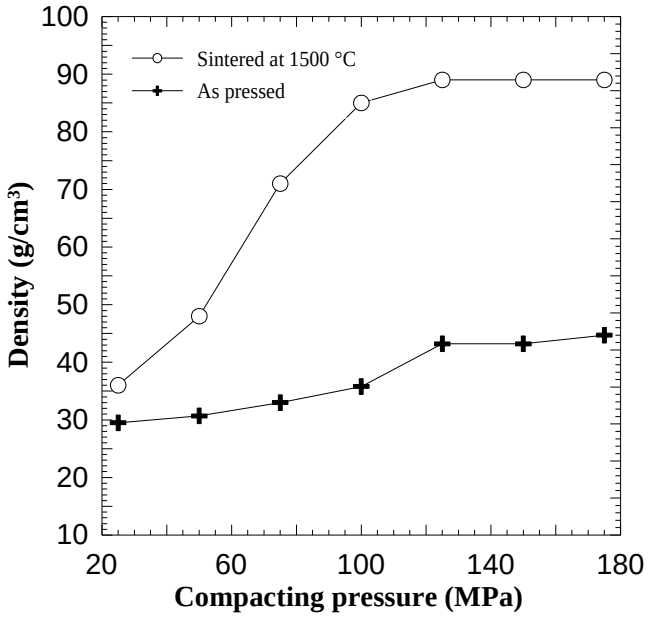

Figure 5-1. The variation of density versus compacting pressure for as-pressed *MK* composites and *MK* composites sintered at 1500°C for 20 minutes; error bars are smaller than symbols

In contrast to *MK*, densification of *NMK* composite was not affected by the green density. The same phenomenon has been reported by Neves et al.[100]; they found that the green density had no influence on the densification of the nano ZnO, while a significant reduction in the final density was recorded for the micro ZnO with the low green densities. They attributed this to the

higher specific surface area and also to the higher rate of grain boundary diffusion of nano particles in comparison to micron sized particles.

Based on the results obtained in this section, specimens made by nano and micron sized powders were pressed uniaxially under the 100 MPa and 125 MPa respectively.

5.2 The influence of trivalent oxides (Fe_2O_3 and Al_2O_3) on the sintering of $MgCr_2O_4$

SEM images of the powder calcined at 850°C are shown in Figure 5-2. Grains with the average size of 0.2, 0.7, and 0.3 μm were observed for $Mg[Cr]_2O_4$, $Mg[Cr_{0.8}Fe_{0.2}]_2O_4$ and $Mg[Cr_{0.8}Al_{0.2}]_2O_4$ compositions calcined at 850°C. Since the calcination temperature was significantly higher than the decomposition temperature of nitrates, it is believed that fewer agglomerates were formed. In fact, the formation of NO_X gas did not allow the formation of agglomerates, assured a homogenous compaction, and reduced stress development during sintering.

The typical *XRD* patterns of $Mg[Cr_{0.8}Fe_{0.2}]_2O_4$ composition calcined at various temperatures are shown in Figure 5-3. It is seen that spinel starts to form at 550°C and is accompanied by MgO, Fe_2O_3 and Cr_2O_3 at 650°C, indicating that nitrates first oxidize and then react to form spinel or spinel solid solutions. When the calcination temperatures were increased to 850˚C and 1050°C, the oxides reacted further to form spinel products, therefore, the intensities of identification peaks decreased for the unreacted oxides and increased for the spinel products.

A -0.352±0.003 degree shift in the position of the (311) identification peaks of spinel is also observed, which can be attributed to the formation of spinel solid solutions. There are similarities between the *XRD* patterns of Al_2O_3 and Fe_2O_3 containing compositions, but at 1050°C a comparison in the peak intensities ratios indicates that the unreacted oxide content in

the $Mg[Cr_{0.8}Al_{0.2}]_2O_4$ compositions ($I_{Cr2O3(104)}/I_{MgCr2O4(311)}$:0.072) is higher than that of $Mg[Cr_{0.8}Fe_{0.2}]_2O_4$ compositions ($I_{Cr2O3(104)}/I_{MgCr2O4(311)}$: 0.033).

In addition, the shift in the position of (311) spinel peaks in $Mg[Cr_{0.8}Al_{0.2}]_2O_4$ composition is +0.214±0.003 degree smaller than that of $Mg[Cr_{0.8}Fe_{0.2}]_2O_4$. The difference between the formation of spinel products in Al_2O_3 and Fe_2O_3 containing compositions is explained by the formation mechanism and kinetics of spinel formation.

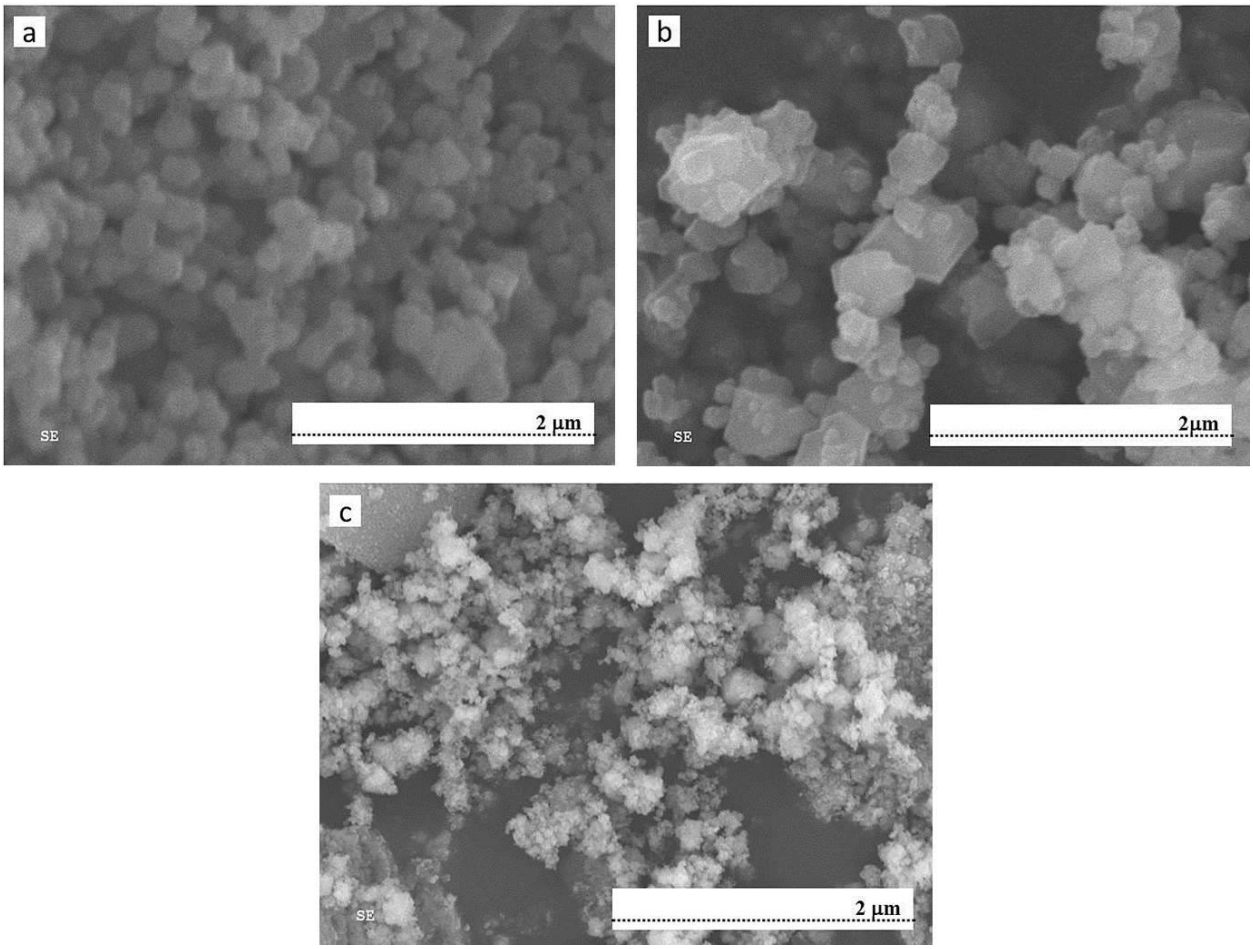

Figure 5-2. *SEM* images of synthesized spinel powders calcined at 850°C a) $MgCr_2O_4$, b) $Mg[Cr_{0.8}Fe_{0.2}]_2O_4$ and c) $Mg[Cr_{0.8}Al_{0.2}]_2O_4$

The formation mechanism of spinels has been explained by the Wagner theory[59]. According to it, spinel formation initiates at the interfaces of the primary oxides and continues by

counter diffusion of cations at the interface of oxides. In this mechanism the formed spinel layer is considered as a barrier to the cations diffusion, and suppresses the formation of spinel, therefore decreasing the formation rate. In the presence of Al_2O_3, $MgAl_2O_4$ spinel forms faster than $MgCr_2O_4$ due to its lower activation energy of formation (171 kJ/mol)[102]. This layer, therefore, should decrease the diffusion rate of cations and decrease the rate of spinel or spinel solid solution formation. However, in the case of $Mg[Cr_{0.8}Fe_{0.2}]_2O_4$ a solid solution formation between $MgFe_2O_4$ and $MgCr_2O_4$ should be faster than the $Mg[Cr_{0.8}Al_{0.2}]_2O_4$ formation, since $MgCr_2O_4$ and $MgFe_2O_4$ form almost in the same time due to their similar activation energies (337 and 323 kJ/mol)[103,104].

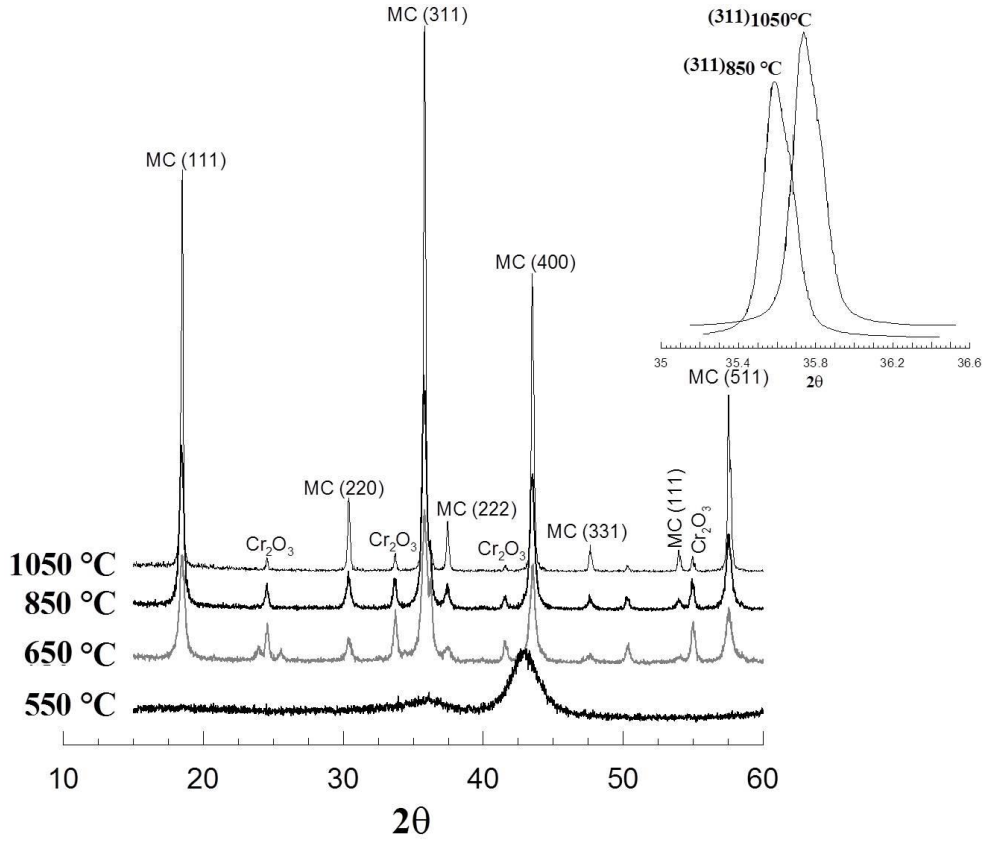

Figure 5-3. *XRD* patterns of $Mg[Cr_{0.8}Fe_{0.2}]_2O_4$ samples calcined at various temperatures

Simultaneous thermal analysis (*DSC*/*TGA*) was used to study the effect of Al_2O_3 and Fe_2O_3 on the kinetics of $MgCr_2O_4$ formation. The typical *STA* plot of $MgCr_2O_4$ is shown in Figure 5-4. The first two endothermic peaks at 150 and 350°C with the corresponding weight loss are attributed to the oxidation of nitrates to magnesium and chromium oxides respectively[105]. The exothermic peak at about 650°C with no weight loss is attributed to the formation of pure $MgCr_2O_4$ formation, since the *XRD* patterns have shown the presence of $MgCr_2O_4$ at 650°C.

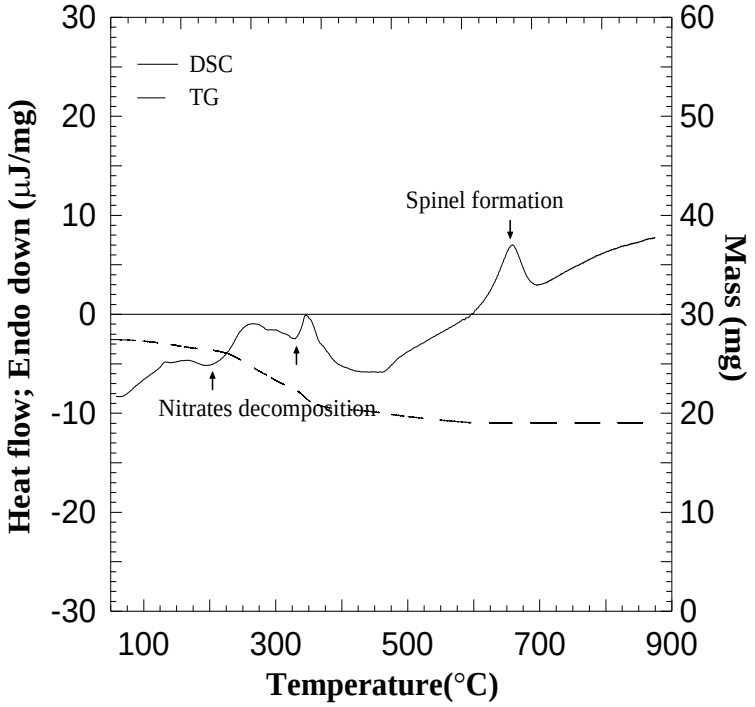

Figure 5-4. The typical *STA* pattern of precursors for $Mg[Cr_{0.8}Fe_{0.2}]_2O_4$ composition

To determine the activation energy (E_a) for the $MgCr_2O_4$ spinel formation in the presence of sintering additives, 25 mg of $Mg[Cr]_2O_4$, $Mg[Cr_{0.8}Fe_{0.2}]_2O_4$ and $Mg[Cr_{0.8}Al_{0.2}]_2O_4$ precursors were used for *STA* analysis. The precursors were heated to 900°C in air with three different heating rates (10, 20 and 25 °/min). It was observed that increasing the heating rate moved the

correlated exothermic peak of spinel formation toward higher temperatures. Figure 5-5 shows the position change with increase in heating rate.

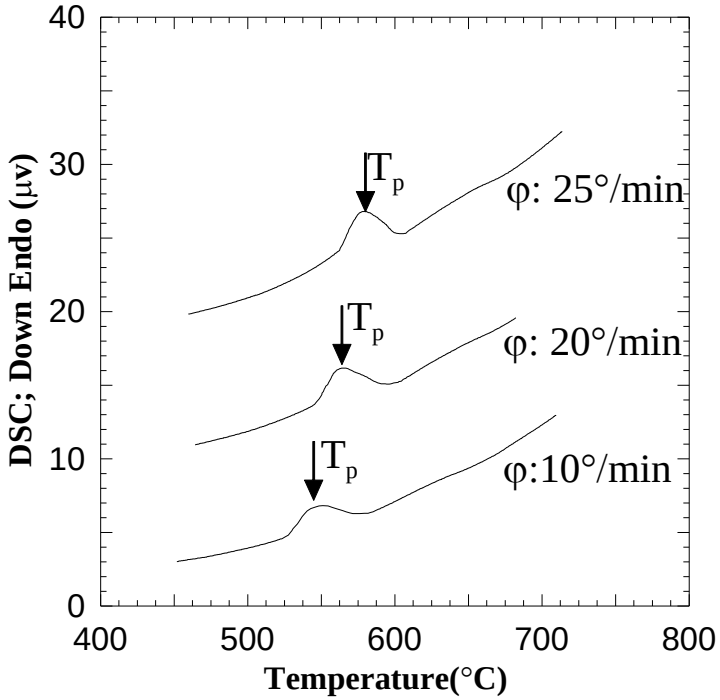

Figure 5-5. The effect of heating rate on the *STA* peak position for $Mg[Cr_{0.8}Fe_{0.2}]_2O_4$ composition

The maximum temperature of the exothermic peak was recorded and analyzed using the Kissinger equation in order to find the activation energy (E_a) of spinel formation [106]:

$$ln(\emptyset/T_P^2) = -E_a/RT_P + constant \qquad 5\text{-}1$$

where T_p (K) is the temperature of the maximum *DSC* formation peak, *R*(J/K.mol) is the universal gas constant, and $\emptyset$ (K/min) is the heating rate. The activation energy (E_a) was calculated from the plot of $\ln(\emptyset/T_P^2)$ vs. $1/T_P$. The Kissinger plot of $MgCr_2O_4$ as a function of composition is shown in Figure 5-6. Based on these plots, the activation energy of the formation of $Mg[Cr]_2O_4$, $Mg[Cr_{0.8}Fe_{0.2}]_2O_4$ and $Mg[Cr_{0.8}Al_{0.2}]_2O_4$ are 329±7 kJ/mol, 298±11 kJ/mol and 206±3 kJ/mol respectively. Since the reported activation energies are the average of 2

measurements, the confidence intervals were set as $2\sigma^*$. The crystallization mechanism is determined by calculating the Avrami constant (n)[107] of the exothermic peak using equation5-2:

$$n_A = \left(2.5T_P^2 R / w_{1/2}\, E_a\right) \qquad 5\text{-}2$$

where $w_{1/2}$ is the full width at half maximum (semi-breath) of the exothermic peak. When n_A is low value (i.e. n_A <2) it implies that surface crystallization is the dominant crystallization mechanism. In contrast, high n value is the indication of high nucleation rate, i.e. n>2.5 for diffusion controlled reactions or n_A >4 for polymorphic transformation[107].

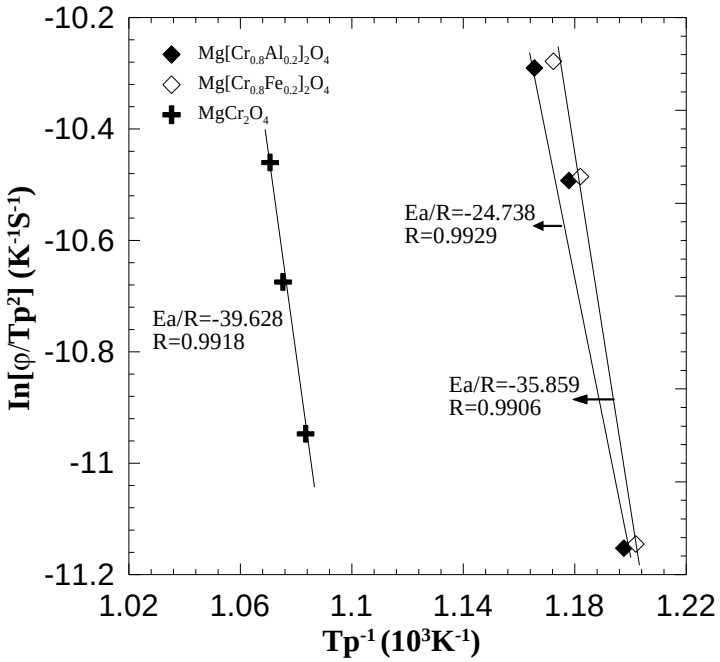

Figure 5-6. Kissinger plot of $\ln\left(\emptyset/T_P^2\right)$vs. $10^3/T_P$ of $MgCr_2O_4$ as a function of composition

Table 5-1 shows the kinetic parameters of the three studied compositions. As seen the Avrami constant of all compositions is above 2.5, as an indication of diffusion controlled spinel formation reaction. The obtained activation energies for $MgCr_2O_4$ and $Mg[Cr_{0.8}Fe_{0.2}]_2O_4$ are close to the value reported by Paik et al. for $MgCr_2O_4$ (323 kJ/mol)[103]. This indicates similar

* σ: Standard deviation

kinetics and mechanism of the formation of these spinels. For the $Mg[Cr_{0.8}Al_{0.2}]_2O_4$ the activation energy is close to the pure $MgAl_2O_4$ (171 kJ/mol)[102], but much lower than for pure $MgCr_2O_4$. In order to find out the reasons, the activation energies of diffusion of cations involved in spinel formation, in their oxides, are compared to the obtained activation energies for each composition.

Table 5-1. Experimental conditions the measured parameters of the spinel formation kinetic studies

	φ (°/min)	*Tp* (K)	$W_{1/2}$ (K)	E_a (kJ/mol)	n_A	Average(n_A)
$Mg[Cr_{0.8}Al_{0.2}]_2O_4$	25	858	28.3	206±3	2.6	2.6
	20	849	29		2.5	
$Mg[Cr_{0.8}Fe_{0.2}]_2O_4$	25	853	22	298±11	2.4	2.6
	20	846	19		2.8	
$Mg[Cr]_2O_4$	25	934	22	329±7	2.5	2.5
	15	930	27		2.5	

The spinel forms by the counter diffusion of cations, so the activation energy of the whole reaction should be close to the activation energy of the diffusion of the slowest cation. A comparison between the activation energies of diffusion of Mg^{+2}(327 kJ/mol), Fe^{+3}(419 kJ/mol)[102], Al^{+3}(477kJ/mol)[108], and Cr^{+3} (~500 kJ/mol)[46] in their oxides and the activation energy of the formation of pure $MgCr_2O_4$ (323 kJ/mol), $MgFe_2O_4$ (337 kJ/mol) and $MgAl_2O_4$ (171 kJ/mol) indicates that the formation of spinel is mostly controlled by the diffusion of trivalent oxides.

The difference in the activation energy of the formation of $MgAl_2O_4$ and $MgCr_2O_4$, or $MgFe_2O_4$ and $MgCr_2O_4$, can be attributed to the type of the trivalent cations. As reported by Fernandez et al.[102] the rate of formation of aluminate spinels is influenced by the site preference energies of divalent cations. They showed that $MgAl_2O_4$ formed faster than $ZnAl_2O_4$ and

$NiAl_2O_4$ because on the one hand, the tetrahedral site preference energy of Mg^{+2} was less than of Zn^{+2} and on the other hand, the octahedral site preference energy of Ni^{+2} was very high (-59 J/mol). As a result, Mg^{+2} moved more readily than Zn^{+2} and Ni^{+2} and increased the rate of $MgAl_2O_4$ formation.

Considering the same analogy, $MgAl_2O_4$ would form before $MgCr_2O_4$ because of the smaller size of Al^{+3} (0.54 Å)[109] than Cr^{+3} (0.62 Å)[109], and because of the smaller octahedral site preference energy of Al^{+3} (-41.9 kJ/mol) than of Cr^{+3} (-87.9 kJ/mol)[38]. The same reason is considered for the small activation energy of $MgCr_2O_4$ in the presence of Fe_2O_3 298 kJ/mol. According to the above discussion, it is hypothesized that $MgAl_2O_4$ and $MgFe_2O_4$ form before $MgCr_2O_4$ via an exothermic reaction[60]. Therefore, the reduction in the activation energy could be attributed to the compensation of part of the activation energy of $MgCr_2O_4$ with the generated heat from the formation of $MgFe_2O_4$ and $MgAl_2O_4$.

The results of kinetic studies of spinel formation indicate that during the formation of both $Mg[Cr_{0.8}Al_{0.2}]_2O_4$ and $Mg[Cr_{0.8}Fe_{0.2}]_2O_4$ solid solutions, the diffusion of Cr^{+3} is controlling the spinel formation rate; however, in $Mg[Cr_{0.8}Al_{0.2}]_2O_4$, due to the fast formation of $MgAl_2O_4$, the $MgCr_2O_4$ formation was more suppressed and resulted in the higher concentration of unreacted oxides at the calcination temperature (850°C).

The influence of the sintering temperature and Fe_2O_3 content on the relative density of the $Mg[Cr_{1-x}Fe_x]_2O_4$ (x=0, 0.15 and 0.2) is presented in Figure 5-7. The results show that for the Fe_2O_3 free samples (x=0), practically no significant densification (<7 % of theoretical density) was observed at 1250˚C-1500˚C. However, densification increased by ~20% in the same sintering temperature range, for the $Mg[Cr_{0.8}Fe_{0.2}]_2O_4$ specimens. Figure 5-9 shows the typical microstructure of the samples sintered at 1250 and 1500°C. It is observed that the higher

sintering temperature reduced the overall porosity of both types of sintered samples; however, the effect of Fe_2O_3 on increasing the density was more significant than the sintering temperature.

This can be explained based on the MgO-Cr_2O_3-Fe_2O_3 phase diagram[110], where there is unlimited solid solubility between $MgCr_2O_4$ and $MgFe_2O_4$, Figure 5-8. Considering 100% conversion of Fe_2O_3 to $MgFe_2O_4$ at the sintering temperatures, the $Mg[Cr_{0.95}Fe_{0.05}]_2O_4$ and $Mg[Cr_{0.8}Fe_{0.2}]_2O_4$ compositions contain about 8.8 and 12.5 wt% $MgFe_2O_4$ respectively.

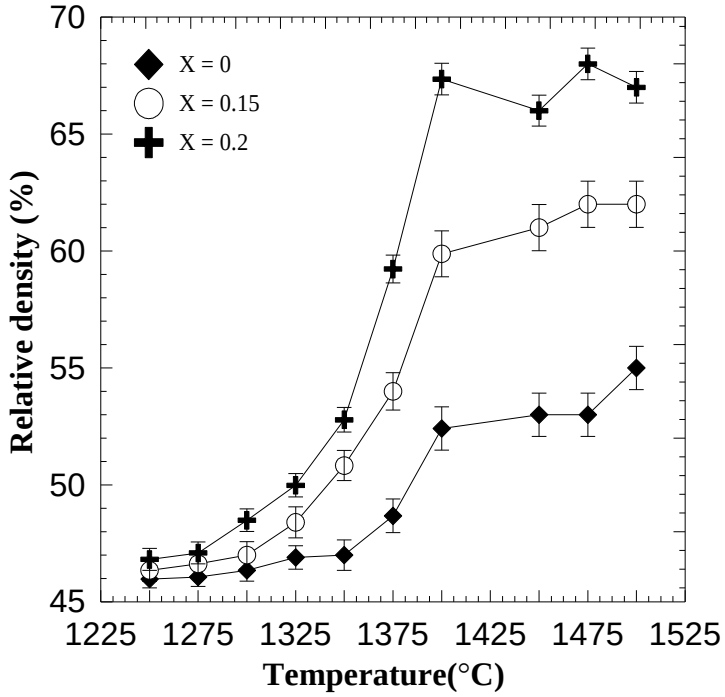

Figure 5-7. The variation of relative density of sintered $Mg[Cr_{1-x}Fe_x]_2O_4$ compositions at different temperatures for 2 hours

Since the phase diagram, Figure 5-8, predicts that $MgCr_2O_4$-$MgFe_2O_4$ solid solution is the thermodynamically stable phase at the sintering temperatures of 1250 and 1500°C, the solid solution should also form during the sintering process studied in this work.

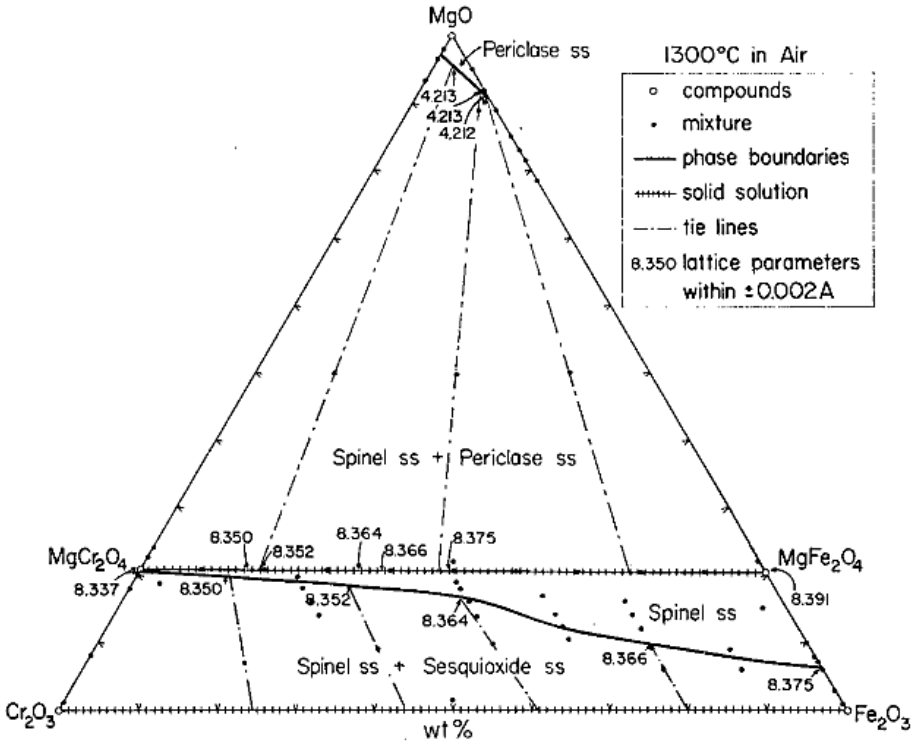

Figure 5-8. The MgO-Cr_2O_3-Fe_2O_3 phase diagram at 1300°C[110]

The *XRD* patterns of specimens containing Fe_2O_3, Figure 5-10a, show indeed the formation of $MgCr_2O_4$-$MgFe_2O_4$ solid solution since no peaks other than shifted $MgCr_2O_4$ peaks are detected. Similar results were also observed in the *XRD* patterns of Al_2O_3 added samples. Figure 5-10b displays the change in $MgCr_2O_4$ lattice parameter with increased sintering additives contents, confirming the formation of solid solutions between $MgCr_2O_4$ and the sintering additives. Considering ±0.0002Å (equivalent to 2σ) error for lattice parameter values, the linear change indicates that the formed solid solutions obey the Vegard's law[111,112]. It has not been reported that $MgCr_2O_4$-$MgAl_2O_4$ or $MgCr_2O_4$-$MgFe_2O_4$ solid solutions indeed obey the Vegard's law, although it has been reported by Amelie[111] for $MgAl_2O_4$-Cr_2O_3 solid solutions. Since the solid solution obeys the Vegard's law, it can be inferred that that the $MgFe_2O_4$ and $MgAl_2O_4$ substitutionally dissolved in $MgCr_2O_4$.

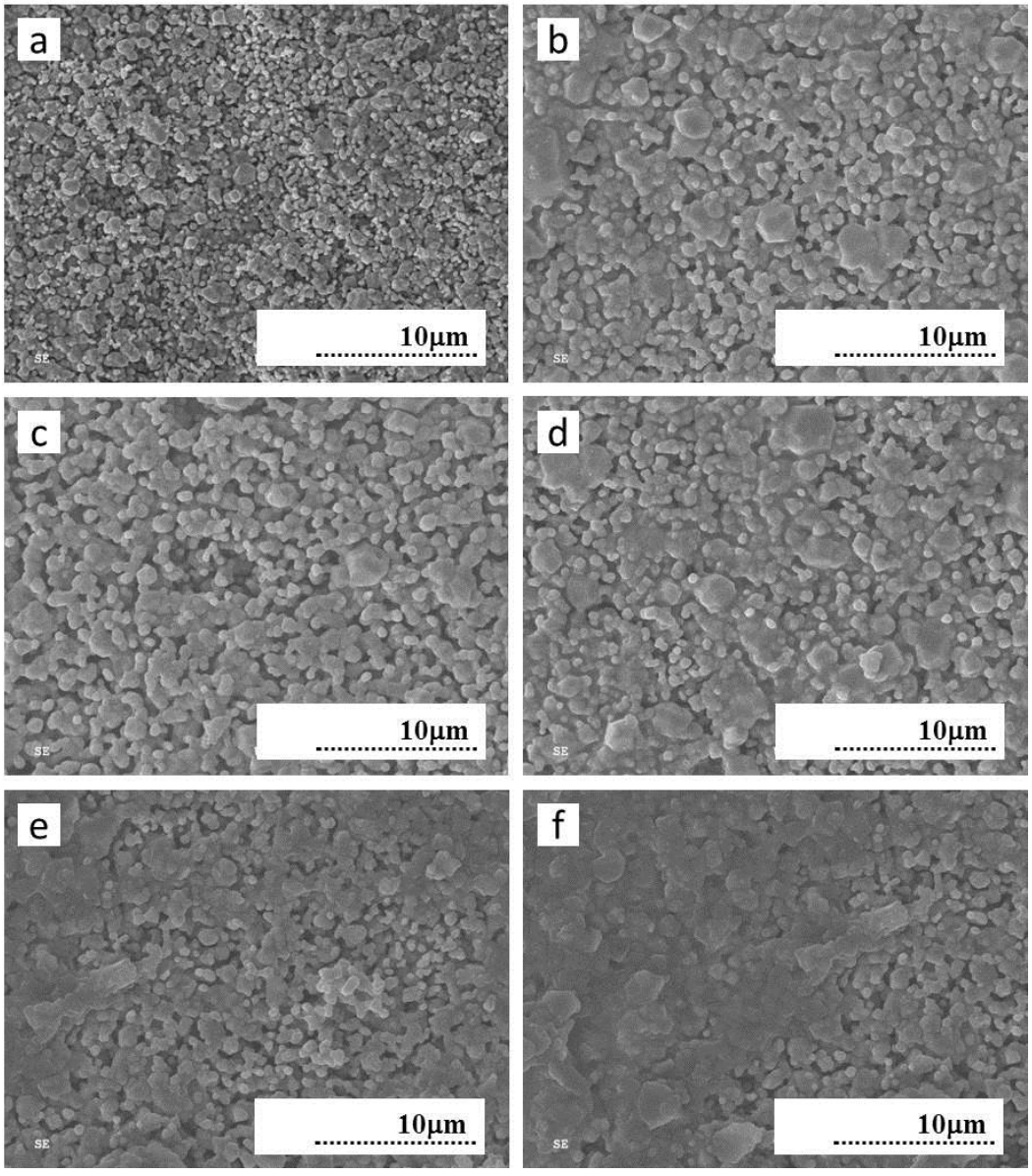

Figure 5-9. SE-*SEM* image of fracture surface of a) $MgCr_2O_4$ sintered at 1250°C, b) $MgCr_2O_4$ sintered at 1500°C, c) $Mg[Cr_{0.8}Al_{0.2}]_2O_4$ sintered at 1250 °C, d) $Mg[Cr_{0.8}Al_{0.2}]_2O_4$ sintered at 1500 °C, e) $Mg[Cr_{0.8}Fe_{0.2}]_2O_4$ sintered at 1250°C, and f) $Mg[Cr_{0.8}Fe_{0.2}]_2O_4$ sintered at 1500°C

Figure 5-10b also shows that the addition of Fe_2O_3 increases the lattice parameter, while Al_2O_3 addition results in lattice parameter decrease. In both cases, due to the presence of the solute cation in the host structure, $MgCr_2O_4$ lattice is expected to be under stress caused by the cation size mismatch[1]. The generated stresses could make the host lattice unstable, causing the

cations to move in a way that reduces the stress. In other words, the stress in the lattice generated due to solid solution formation could work as an additional driving force for sintering[1].

It has been previously shown by Anderson[82] that the $MgCr_2O_4$ spinel cannot be fully densified in air due to its decomposition according to the reaction 2-10. On the contrary, Yamaguchi[12] showed that by introducing TiO_2 to $MgCr_2O_4$, a solid solution would form between $MgCr_2O_4$ and TiO_2 that causes the increase of the cationic mobility and densification. Figure 5-11 shows the variation of the relative density of $Mg[Cr_{1-x}Me_x]_2O_4$; (Me: Al and Fe; $0 \leq x \leq 0.2$) with the sintering temperature. Although the same trend is observed for both compositions, the obtained relative density for the specimens containing Al_2O_3 was smaller than for the specimens containing Fe_2O_3. This suggests different interaction mechanisms between the sintering additives (Fe_2O_3 and Al_2O_3) and $MgCr_2O_4$. There is unlimited solid solubility between $MgCr_2O_4$ and sintering additive derived spinels (both $MgFe_2O_4$ and $MgAl_2O_4$), which indicates that the formation of solid solution is not the only reason for the enhanced densification.

Later in this thesis it is discussed that the unit cell volume of the spinels increases in the presence of Fe_2O_3, and decreases in the presence of Al_2O_3. As a result, it is estimated that cation mobility in Al_2O_3 containing samples is less than in the samples containing Fe_2O_3, and thus the densification rates change in the same manner.

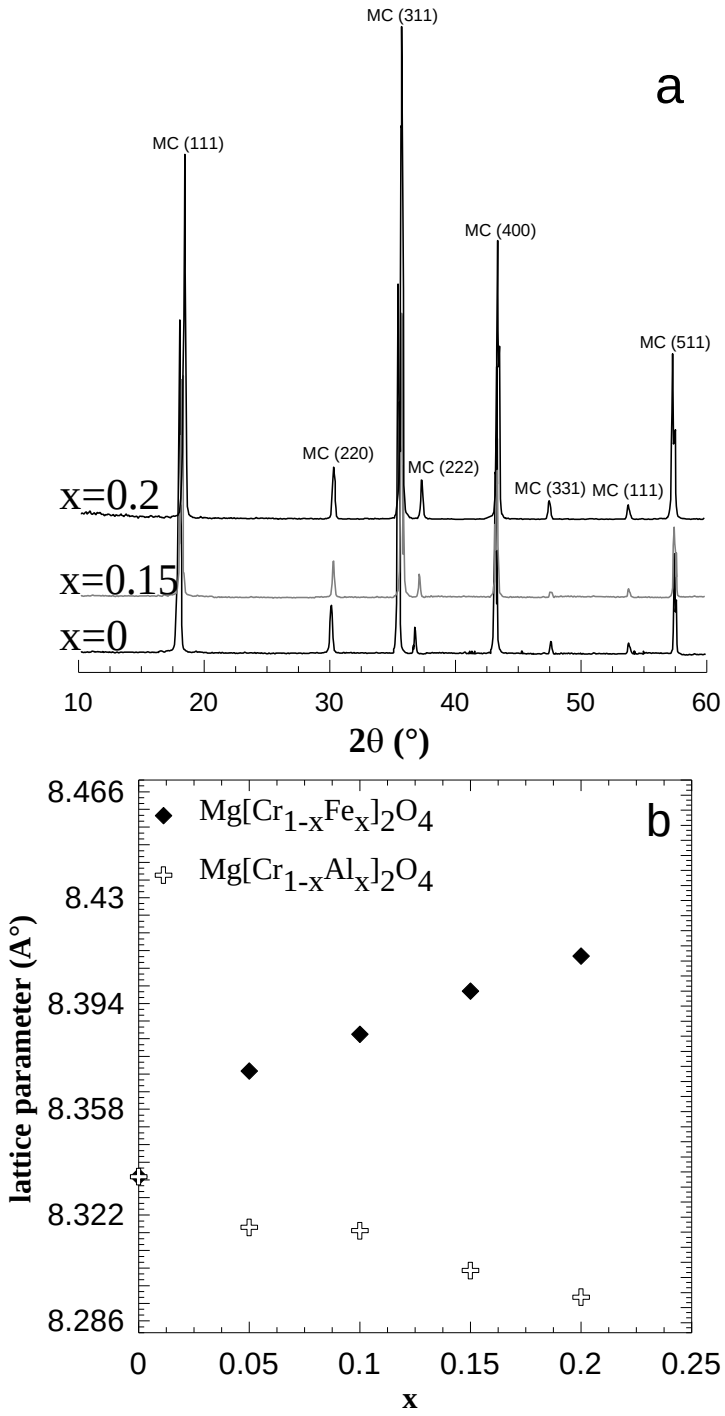

Figure 5-10. a) *XRD* pattern of $Mg[Cr_{1-x}Fe_x]_2O_4$ quenched from 1475°C in air b) the variation of lattice parameter versus Al_2O_3 and Fe_2O_3 concentration; error bars are smaller than symbols

$MgAl_2O_4$ is a normal spinel while $MgFe_2O_4$ is an inverse spinel[3,49,113]. Therefore, in the presence of Fe^{+3}, some degree of inversion in $MgCr_2O_4$ lattice should also occur. Since at the sintering temperatures the inversion process of $MgCr_2O_4$ in the presence of Fe_2O_3 is thermodynamically favorable and inversion is a diffusion controlled process, then it likely adds to the driving force of sintering. It is therefore suggested that Fe^{+3} increases the cationic mobility in $MgCr_2O_4$ to a higher degree than Al_2O_3 because it forms an inverse solid solution, while Al_2O_3 forms a normal solid solution with $MgCr_2O_4$.

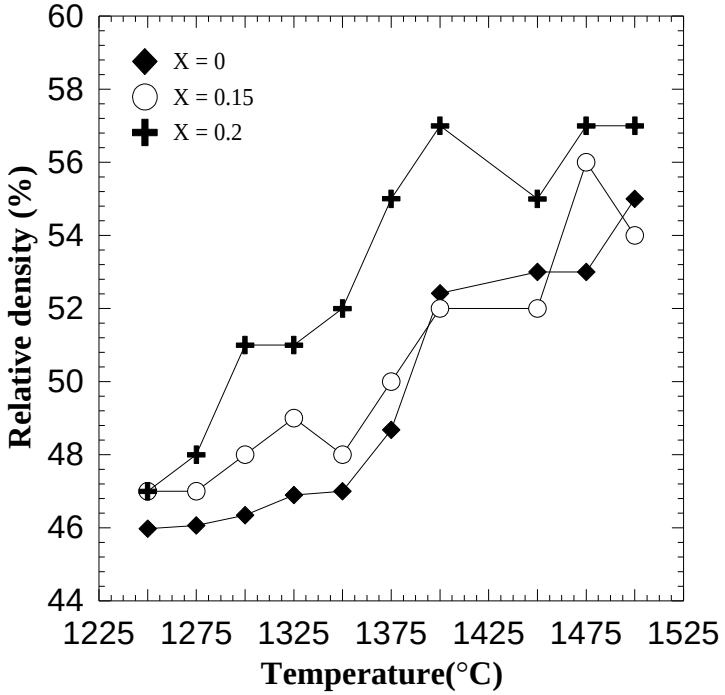

Figure 5-11. The variation of the relative density of $Mg[Cr_{1-x}Al_x]_2O_4$ specimens sintered at different temperatures for 2hours; the lines connect the data points only for the purpose of easier readability

To investigate the influence of inversion on the densification behavior of $Mg[Cr_{1-x}Me_x]_2O_4$ (Me: Al and Fe; $0 \leq x \leq 0.2$) compositions, the *XRD* patterns of sintered specimens were analyzed using the method introduced by Porta[3]. The specimens quenched from the sintering temperature were pulverized to less than 5 µm particle size to assure the homogenous distribution of planes in

the *XRD* specimens. The distribution of cations between the tetrahedral and octahedral sites was estimated by comparing the intensity ratios of the experimental and the calculated data.

It was described by Patange et al.[114] that a comprehensive information on the distribution of cations between the tetrahedral and octahedral sites of a spinel structure can be achieved by comparing the experimental and theoretical intensities of peaks whose intensities were (i) independent of oxygen parameter, (ii) did not differ dramatically, and (iii) were proportional to the reciprocal of cation distribution. In spinels, the (220), (311), (400), and (422) planes have such characteristics; therefore in this work the inversion parameter was estimated based on the comparison between the intensity ratios of the peaks related to these planes. The theoretical intensities were calculated using the following equation[94]:

$$I_{hkl} = |F|^2_{hkl}.P.L_p \qquad 5\text{-}3$$

where I_{hkl} is the intensity, F is the structure factor, P is the multiplicity factor and L_p is the Lorentz-polarization factor. The values for the F, P and L_p factors were extracted from literature[94]. As mentioned by Cullity[94], the equation 5-3 gives the peaks intensity for 0 K, where there is no atomic vibration.

For accurate intensity measurement at room temperature, several authors[3,94] studied the effect of the temperature factor on the calculated intensity and reported that for high melting point crystals the thermal vibration of atoms at room temperature is low enough that would not influence the calculated intensity. For this reason the effect of temperature on the intensity has not been investigated in this study. The structural factors were calculated using the equation used by Porta[3] as follows:

$$F = F_O + \lambda \Delta F_1 \qquad 5\text{-}4$$

where F_o is the structural factor for normal spinel; λ is related to the inversion parameter (equals 0.5 and zero for inverse and normal spinels), Δ is the atomic scattering factor and F_1 is defined as a numerical factor. Table 5-2 shows the scattering factors for selected reflections as reported by Porta[3].

Table 5-2. Scattering factors for selected *XRD* reflections[3]

Reflection	$h^2+k^2+l^2$	*P*	F_O	F_1
311	16*n*+11	24	$f_y+f_x/\sqrt{2}$	$-(\sqrt{2}-1)$
400	16(2*n*+1)	6	$2f_y-f_x+4f_{ox}$	4
220	16*n*+8	12	f_x	-2
422	16*n*+8	24	f_x	-2

f_x*, f_y, f_{ox} are atomic scattering factor of cations in tetrahedral and octahedral sites, and oxygen ions; *n* is an integer

Based on the model developed by Porta[3], the composition of $MgAl_2O_4$-$NiFe_2O_4$ solid solution is considered as $Ni_{x\alpha}Mg_{(1-x)}\beta Al_{2\lambda}[Ni_{x(1-\alpha)}Mg_{(1-x)(1-\beta)}Al_{2-2\lambda}]O_4$ in which α, β, and λ were the fractions of Ni^{+2}, Mg^{+2}, Al^{+3} in the tetrahedral sites respectively. Porter related λ to α, β, and *x* as follows:

$$2\lambda = 1 - x\alpha - (1-x)\beta \qquad 5\text{-}5$$

It should be mentioned that based on the definition, the inversion parameter is the fraction of trivalent cations in tetrahedral site; therefore λ has the same definition in both 5-4 and 5-5 equations.

In our study, to further simplify the inversion parameter calculation, it was assumed that the final spinel solid solution maintained the stoichiometric composition of the spinel structure. The Cr^{+3} was assumed to fill only the octahedral sites due to its high octahedral site preference

* Weighted values were used for calculation of f_x and f_y.

energy (-87.6 kJ/mol). Based on these assumptions the composition of solid solution in the studied systems, $MgCr_2O_4$-$N_A MgFe_2O_4$ and $MgCr_2O_4$-$M_A MgAl_2O_4$, is defined as $(Mg_{1-\xi}Me_{\xi})[Mg_{\xi}Me_{2NA-\xi}Cr_{2-2NA}]O_4$ in which ξ and N_A are the fractions of Me^{+3} in the tetrahedral sites and M_A *is* the mol fraction of $MgFe_2O_4$ and $MgAl_2O_4$.

The intensity ratios for I_{311}/I_{220} were calculated by changing ξ for various intervals for compositions with x=0, 0.05, 0.2. The intervals for ξ were selected between 0.01 and 0.1 based on the convergence of the calculated and experimental data. The resulting inversion parameter was considered the value at which the closest fit with the experimental results was obtained.

The typical graphs that were constructed to estimate the inversion parameter are shown in Figure 5-12. At ξ values close to 0.24 the calculated intensity ratio curves converge with the experimentally obtained intensity ratio curves. As we defined the inversion parameter as the fraction of trivalent cations in the tetrahedral sites, the inversion parameter equals ξ. The value inversion parameter in this study is an average of three values obtained from I_{311}/I_{220}, I_{400}/I_{220}, and I_{311}/I_{422} intensity ratios. The confidence intervals for inversion parameter is estimated based on $\sigma/\sqrt{3}$ (i.e. assumes uniform distribution of the results) and was about the same value (0.0003) for all three measurements.

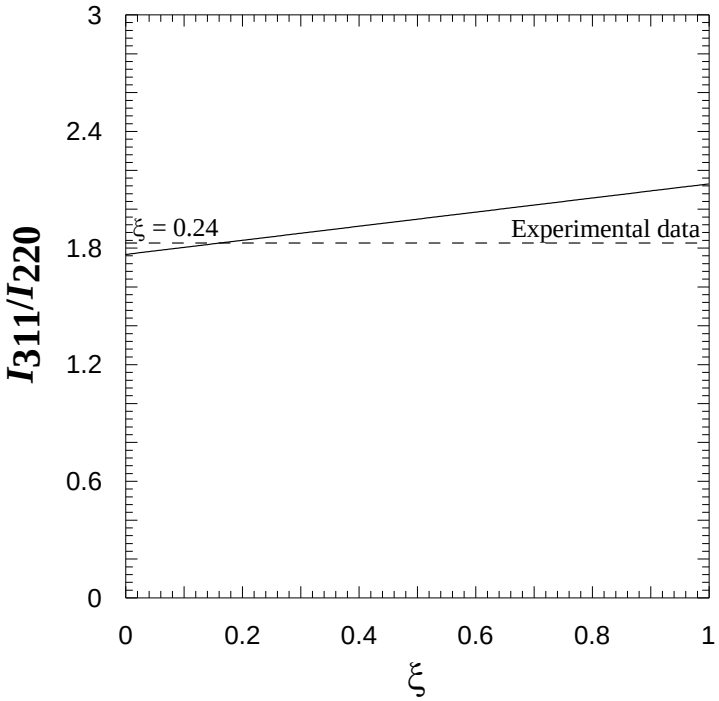

Figure 5-12. The comparison between the intensity ratios, I_{311}/I_{220}, of calculated and experimental results for inversion parameter mesurement. The results in this graph relate to $Mg[Cr_{0.8}Fe_{0.2}]_2O_4$ which was quenched from 1300°C.

The inversion parameter for other selected compositions was calculated in a same way as described above, and plotted as a function of temperature in Fig.5-13 for different concentrations of sintering additives (Al_2O_3, Fe_2O_3). It is clear that the inversion parameter increases with temperature regardless of the type of sintering additives. The same behavior was also observed by Martingo et al.[115] investigating the kinetics of natural and synthetic $Mg(Al,Fe)_2O_4$ system. They showed increasing the temperature increased the degree of inversion.

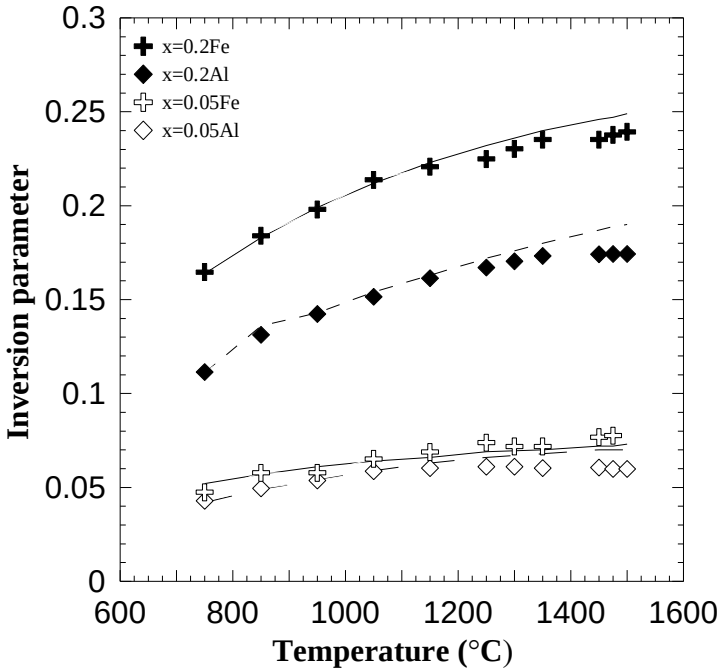

Figure 5-13. The variation of the inversion parameters in $Mg[Cr_{1-x}Fe_x]_2O_4$ and $Mg[Cr_{1-x}Al_x]_2O_4$ with concentration of the sintering additives and sintering temperature (the lines represent the thermodynamic model and not the best fit – refer to text)

Figure 5-13 also illustrates that the degree of inversion is higher for samples containing Fe than for those containing Al, and the increase in the concentration of sintering additives has a significant influence on the degree of inversion. This behavior can be explained by considering the effect of site preference energies of Cr^{+3}, Fe^{+3} and Al^{+3}. Martignago and Negro[116] showed that the degree of inversion of $Mg(Cr,Al)_2O_4$ was lower than that of $Mg(Fe,Al)_2O_4$ at each temperature. Also they showed that the inversion parameter was inversely proportional to the Cr^{+3} content. They attributed this to the high octahedral site preference energy of Cr^{+3}, which limits the Mg-Al cation exchange.

Due to the inversion phenomenon in a spinel structure, $(A^{+2})^{tet}[B^{+3}]^{oct}{}_2O_4$, a fraction of trivalent cations (ξ) move from the octahedral sites to the tetrahedral sites. Based on this

relocation, the chemical formula of the spinel would change to $(A_{1-\xi}B_{\xi})^{tet}[B_{2-\xi}A_{\xi}]^{oct}O_4$ and the inversion reaction could be written as $(1-\xi)(A)_{tet}+(2-\xi)[B]_{oct} \rightarrow \xi(B)_{tet}+\xi[A]_{oct}$.

In the study by O'Neil et. al[39], the equilibrium constant for the above reaction was related to the site preference energy of cations and the entropy change during cations site changes. According to this study, the change in free energy of disordering cation distribution (ΔG_D) is zero at equilibrium, and the equilibrium constant of the interchange reaction between tetrahedral and octahedral sites $(1-\xi)(A)_{tet}+(2-\xi)[B]_{oct} = \xi(B)_{tet}+\xi[A]_{oct}$, is as follows:

$$ln\left(\frac{\xi^2}{(1-\xi)(2-\xi)}\right) = -(\alpha^{A-B} + 2\beta'\xi)/RT \qquad 5\text{-}6$$

where ξ is the inversion parameter, $\alpha^{A\text{-}B}$ is the difference between site preference energies of *A* and *B* respectively and is an indication of configurational entropy, and β' is a constant of about -20 kJ/mol for all 2-3 spinels[49].

The accuracy of the results obtained in our work has been judged by comparing them with the above thermodynamic model, developed by O'Neil et al.[39] In this regard, the chemical formulas of the spinel solid solutions in $MgCr_2O_4$-$M_A MgAl_2O_4$ and $MgCr_2O_4$-$N_A MgFe_2O_4$ systems before inversion were estimated as $(Mg^{+2})^{tet}[Cr^{+3}_{2-2MA}Al^{+3}_{2MA}]^{oct}O_4$ and $(Mg^{+2})^{tet}[Cr^{+3}_{2-2NA}Fe^{+3}_{2NA}]^{oct}O_4$ respectively. N_A and M_A were the mole fractions of $MgFe_2O_4$ and $MgAl_2O_4$ in the solid solution, respectively. The chemical formula of the solid solutions after inversion was also estimated based on the assumption that the Cr^{+3} cations remain in the octahedral site in any conditions. Based on this assumption the chemical formula of the solid solutions after inversion would be $(Mg_{1-\xi}Al_{\xi})^{tet}[Cr_{2-2MA}Al_{2MA-\xi}Mg_{\xi}]^{oct}O_4$ and $(Mg_{1-\xi}Al_{\xi})^{tet}[Cr_{2-2NA}Fe_{2NA-\xi}Mg_{\xi}]^{oct}O_4$. The cation distribution reactions between $MgCr_2O_4$ and $N_A MgFe_2O_4$ and $MgCr_2O_4$ and $M_A MgAl_2O_4$ can be therefore written as follows:

$$(1-\xi)(Mg^{+2})_T + (2_{MA}-\xi)[Al^{+3}]_O \rightarrow \xi[Mg^{+2}]_O + \xi(Al^{+3})_T \quad 5\text{-}7$$

$$(1-\xi)(Mg^{+2})_T + (2_{NA}-\xi)[Fe^{+3}]_O \rightarrow \xi[Mg^{+2}]_O + \xi(Fe^{+3})_T \quad 5\text{-}8$$

According to these reactions, a part of Mg^{+2} in tetrahedral sites is replaced by Fe^{+3} or Al^{+3}, and Mg^{+2} enters into the octahedral sites of the spinel lattice. The resulting increase in the inversion parameter therefore means that more cations are exchanged between the tetrahedral and octahedral sites. Thus the inversion phenomenon likely increases the cation mobility and therefore the sintered density of these materials. A comparison between the values of inversion parameters for Al and Fe containing samples clearly illustrates that the inversion could be an influential factor in the higher densification of $(Mg^{+2})^{tet}[Cr^{+3}_{2-2NA}\ Fe^{+3}_{2NA}]^{oct}O_4$ solid solutions than $(Mg^{+2})^{tet}[Cr^{+3}_{2-2MA}\ Al^{+3}_{2MA}]^{oct}O_4$.

The ONeil's thermodynamic model was modified in this work for the $MgCr_2O_4$-$N_A MgFe_2O_4$ and $MgCr_2O_4$-$M_A MgAl_2O_4$. As mentioned earlier, in order to simplify the calculation of cation distribution, it was assumed that the Cr^{+3} remains in the octahedral site due to its very high octahedral site preference energy (-160 kJ/mol)[49]. Based on this assumption, the equilibrium constant for the cation distribution via equations 5-7 and 5-8 would be the following:

$$ln\left(\frac{\xi^2}{(1-\xi)(2N_A-\xi)}\right) = -(\alpha^{Mg-Fe} + 2\beta'^{Mg-Fe}\xi)/RT \quad 5\text{-}9$$

$$ln\left(\frac{\xi^2}{(1-\xi)(2M_A-\xi)}\right) = -(\alpha^{Mg-Al} + 2\beta'^{Mg-Al}\xi)/RT \quad 5\text{-}10$$

where N_A and M_A are the mole fractions of $MgFe_2O_4$ and $MgAl_2O_4$. The values of $\alpha^{Mg\text{-}Al}$ (26.6 kJ/mol), $\alpha^{Mg\text{-}Fe}$ (23 kJ/mol), $\beta'^{Mg\text{-}Al}$(-21.7 kJ/mol), and $\beta'^{Mg\text{-}Fe}$ (13 kJ/mol) were extracted from literature[39, 49, 67].

It is seen in Figure 5-13 that the experimental results (symbols) correlate well with the thermodynamic model developed by Hugh and O'Neill (lines)[39] at temperatures below 1250°C.

At temperatures above 1300°C there is a small deviation from the model, which is attributed to changes in the materials due to insufficient cooling rates. In fact, the cooling rate usually is not high enough to quench the cation distribution at the soak temperature. This phenomenon is more significant in Fe containing sample as reported by Walters and Wirtz[117]. Fe^{+3} and Al^{+3} substituted for Cr^{+3} occupy both tetrahedral and octahedral sites. The presence of Cr^{+3}, which has the highest octahedral site preference energy among other cations[109], is expected to intensify this site interchange process. Thus Fe^{+3} preferred tetrahedral sites and therefore forced Mg^{+2} to move to the octahedral sites.

The ionic radius of Fe (r_{Fe}^{+3} = 0.67Å) is larger than of Mg^{+2} (r_{Mg}^{+2} = 0.57Å); therefore, it is expected that Fe^{+3}expanded the tetrahedral site size and displaced the oxygen ions toward the octahedral sites and consequently shrank them. The same phenomenon could happen for Al^{+3} but, as its ionic radius (r_{Al}^{+3} = 0.54 Å) is smaller than that of magnesium and chromium ions, it would have caused opposite effect, i.e. shrinkage of the tetrahedral sites and expansion of the octahedral sites. Despite the opposite effect of Al^{+3} and Fe^{+3} on the $MgCr_2O_4$ lattice, it appears that they both caused the displacements, thus increasing ionic mobility, which in turn enhanced the densification of these spinels.

In order to study whether the solid solution formation rate affects the densification, the variation of $MgCr_2O_4$ lattice parameter versus sintering temperature for both types of additives is plotted in Figure 5-14. For the $Mg[Cr_{0.8}Fe_{0.2}]_2O_4$ composition, a solid solution formed at temperatures below 1250°C as no changes in lattice dimension was observed. In contrast, the lattice dimension decreased continuously with the increase in the sintering temperature for $Mg[Cr_{0.8}Al_{0.2}]_2O_4$.

This indicates that at the same sintering temperature more solid solution formed in Fe_2O_3 containing samples than in Al_2O_3 containing samples. This is expected based on the earlier results on the kinetics of spinel formation. As shown later, in the presence of iron oxide both $MgFe_2O_4$ and $MgCr_2O_4$ form almost in the same time. In contrast, in the presence of aluminum oxide, $MgAl_2O_4$ spinel forms faster than $MgCr_2O_4$ and creates a $MgAl_2O_4$ spinel barrier between chromium oxide and magnesium oxide. Thus, it is expected that the solid solution formation rate in the $MgCr_2O_4$-$N_A$$MgFe_2O_4$ samples is higher than in the $MgCr_2O_4$-$M_A$$MgAl_2O_4$ samples.

Wang et al.[118] showed the same result studying the effect of solid solution formation on the sintering of ZrC. He demonstrated that the rate of solid solution formation influenced the extent of ZrC densification. It was shown that VC with 1.3 vol% solid solubility limit with ZrC was more effective in sintering and densification of ZrC than TaC and NbC with unlimited solid solubility in ZrC, due to the faster formation of VC solid solution than TaC and NbC.

At 1250˚C-1500˚C, i.e. at early stages of sintering, a weight loss of 0.08 to 0.1% was observed for all compositions. It is therefore believed that "evaporation-condensation" was the main mass transportation mechanism during the densification in this temperature range, and caused the grain growth in all samples regardless of the type and concentration of additives[86].

The weight loss and the compressive strength of the samples versus the sintering additives content are plotted in Figure 5-15. Each data point in these plots is the average value of the measured property for 3 specimens. The increase in additive content did not change the weight loss considerably but it raised the compressive strength of specimens. The enhancement of the compressive strength, where no significant densification was involved, confirmed that the evaporation-condensation was the mass transfer mechanism[5].The same behavior was observed in

sintering of materials with a high vapor pressure at sintering temperatures, for example Si_3N_4 and SiC with a covalent bond nature[4].

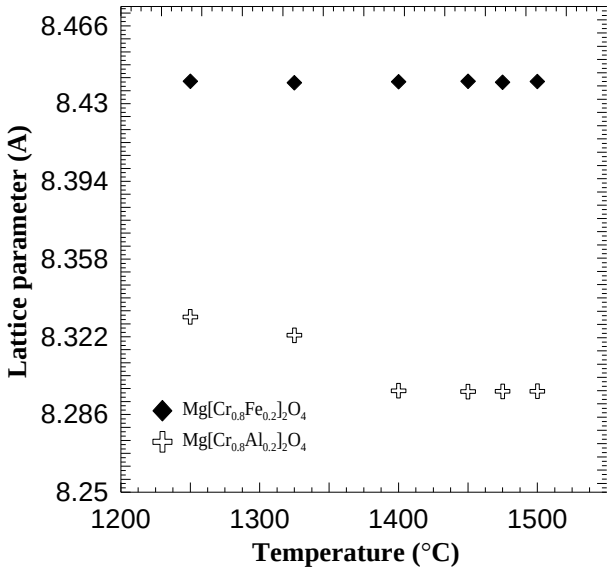

Figure 5-14. The variation of the lattice parameters of $Mg[Cr_{0.8}Al_{0.2}]_2O_4$ and $Mg[Cr_{0.8}Fe_{0.2}]_2O_4$ versus the sintering temperature

In order to better understand how the sintering is influenced by the sintering additives in the systems under consideration, the influence of the possible mechanisms of solid solution formation and the crystalline structures of the solid solutions is discussed. At elevated temperatures, Fe^{+3} and Al^{+3} should diffuse into the $MgCr_2O_4$ lattice through the available tetrahedral and octahedral sites. Assuming that the synthesized $MgCr_2O_4$ has no defects, it would consist of 72 unoccupied lattice sites per unit cell, including 16 octahedral and 56 tetrahedral, available for the introduced sintering additive[119]. Due to this lattice structure, the interaction between the sintering additives and lattice sites can happen in three different scenarios. In the first scenario, substituting Fe^{+3} or Al^{+3} for Mg^{+2} results in the formation of V''_{Mg} and V''_{Al} due to the high affinity of Cr^{+3} to octahedral sites, through the following reactions:

$$Fe_2O_3 \xrightarrow{MgCr_2O_4} 2\dot{F}e_{Mg} + V''_{Mg} + 3O_O^x \quad 5\text{-}11$$

$$Al_2O_3 \xrightarrow{MgCr_2O_4} 2\dot{A}l_{Mg} + V''_{Al} + 3O_O^x \quad 5\text{-}12$$

The formation of vacancies facilitates the overall diffusion rate and eventually the densification. However, the vacancy formation is expected to increase the lattice parameter of $MgCr_2O_4$ when there is an increase in Fe_2O_3 and Al_2O_3 content. Figure 5-10b shows that the addition of Fe_2O_3 resulted in increase in lattice parameter as predicted in reaction 5-12, while a decrease in the lattice parameter was observed when Al_2O_3 was added, implying that the reaction (5-12) may not happen.

In the second scenario, Fe^{+3} and Al^{+3} could substitute for Cr^{+3}. In case of Fe^{+3} this is unlikely, as the octahedral site preference energy* (*OSPE*) of Cr^{+3} [-87.9 kJ/mol] is higher than that of Fe^{+3}[18.8 kJ/mol], which makes substitution process thermodynamically impossible[38]. Therefore in this scenario, Fe^{+3} can form a solid solution with $MgCr_2O_4$ only where there is a partial reduction of Fe^{+3} to Fe^{+2} by the conversion of Cr^{+2} to Cr^{+3}, as predicted by the Ellingham diagram[120]. Only in this case Fe^{+2} could enter either octahedral or tetrahedral sites, or substitute for Mg^{+2}. Due to their very low *OSPE* [4.2 kJ/mol] the Fe^{+2} ions would not be able to enter into octahedral sites in the presence of Cr^{+3}, thus they would rather occupy the available tetrahedral sites, which should increase the lattice parameter of $MgCr_2O_4$ due to the larger tetrahedral bond distance of Fe^{+2} than that of Mg^{+2}[113].

* *OSPE* is defined as the difference between crystal field stabilization energy (*CFSE*) of octahedral and tetrahedral sites[109].

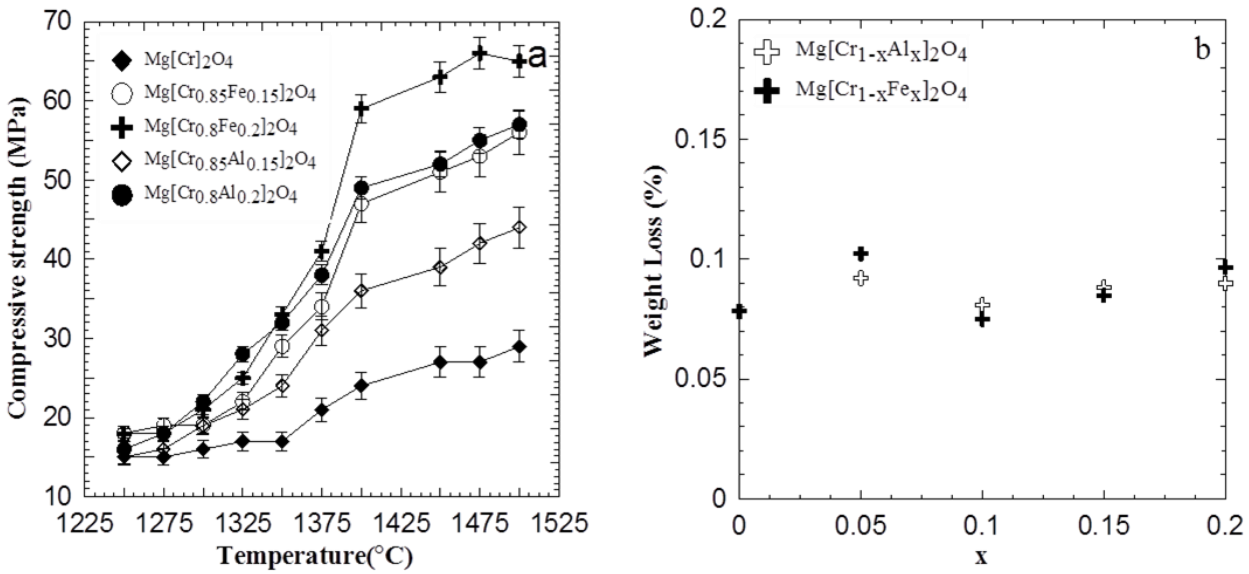

Figure 5-15. a) The variation of compressive strength of samples sintered at various temperatures, b) weight loss of $Mg[Cr_{1-x}Fe_x]_2O_4$ and $Mg[Cr_{1-x}Al_x]_2O_4$ samples sintered at 1475°C

As mentioned above, the Fe^{+2} could also replace Mg^{+2}, as the size difference between Fe^{+3} (0.67 Å) and Mg^{+2} (0.57 Å)[109] is less than 15 %; therefore, an increase in lattice parameter is expected at higher Fe_2O_3 content. However, the mechanisms under scenario 2 were less probable since the sintering was performed in air, where the chance of iron reduction was very low.

As shown in Figure 5-10b the lattice parameter of $MgCr_2O_4$ increased linearly with increasing the Fe_2O_3 content. Based on the above scenarios and the change in the trend of the lattice parameters, the mechanism of the solid solution formation in $Mg[Cr_{1-x}Fe_x]_2O_4$ system could include diffusion of Fe^{+3} into tetrahedral sites of the $MgCr_2O_4$ lattice. The same behavior was also elucidated by Walter et al.[42]; in their study of $Mg[Cr_{1-x}Fe_x]_2O_4$ solid solution series, they reported that the lattice parameter grew linearly with increasing the $MgCr_2O_4$ content. Moreover, they have shown that the normality of $MgCr_2O_4$ decreased by increasing the $MgFe_2O_4$ content. Francesco[71] also showed that the increase in Fe^{+3} reduced the activation energy for inversion of $MgAl_2O_4$ spinel from 274 to 265 kJ/mol. Therefore, based on above discussion and

plots of inversion parameter versus temperature and composition (Figure 5-13), it was concluded that the increase in Fe_2O_3 introduced inversion to $MgCr_2O_4$ and subsequently enhanced the densification.

Al^{+3} has the *OSPE* of [-41.9 kJ/mol] which is 5 times higher than *OSPE* of Fe^{+3} and also is the second highest *OSPE*, implying the higher possibility of substitution of Al^{+3} with Cr^{+3} than of Fe^{+3} with Cr^{+3} in the octahedral sites[38]. The presence of Al^{+3} in the octahedral sites was also observed in the study by Ulf [121], where the color change in $MgAl_2O_4$- $MgCr_2O_4$ solid solution was studied. Moreover, the size difference between Al^{+3} (0.39 Å) and Mg^{+2} (0.57 Å)[109] is more than 30 %, which indicates that the Al^{+3} cannot be substituted for Mg^{+2} in tetrahedral sites. Therefore, Al^{+3} cations occupy other available octahedral sites in $MgCr_2O_4$ unit cell. If this scenario happens, then due to the smaller octahedral bond distances of Al^{+3} (M-O: 1.915 Å) in comparison to that of Cr^{+3} (M-O: 1995 Å)[122], the lattice parameter of $MgCr_2O_4$ should be reduced when Al_2O_3 content increased. Considering the above discussion and the results observed in Figure 5-10b and Figure 5-13, it is concluded that the Al^{+3} is probably located in the octahedral sites and the formed solid solution is a normal spinel.

According to the experimental observations and theoretical analysis, it is concluded that the addition of trivalent oxides enhanced the densification of $MgCr_2O_4$ in air at temperatures below 1500°C. The increased densification is attributed to the increased cationic mobility due to the solid solution formation and to the inversion phenomenon in the $MgCr_2O_4$ crystal structure. The difference between the performance of Fe_2O_3 and Al_2O_3 as sintering additives is explained by the manner in which each trivalent cation changed the $MgCr_2O_4$ unit cell. It is shown that the Fe_2O_3 is more effective than Al_2O_3, as it creates an inverse solid solution. In addition, the weight

loss results showed that the addition of Al_2O_3 and Fe_2O_3 did not change the oxidation kinetics of Cr^{+3} and accordingly did not change its vaporization.

In order to understand the contribution of solid solution formation and the proposed inversion phenomenon on the densification behavior of $MgCr_2O_4$, the effect of SnO_2 as a sintering additive for $MgCr_2O_4$ was also studied. The SnO_2 was selected for two reasons: because it forms Mg_2SnO_4 spinel in reaction with MgO, and because as a tetravalent cation has a different effect on the $MgCr_2O_4$ lattice.

5.3 The effect of tetravalent oxides (SnO_2) on the sintering of $MgCr_2O_4$ spinel

In the previous section, several mechanisms were discussed and an explanation for the change in the sintering behavior of $MgCr_2O_4$ in the presence of Fe_2O_3 and Al_2O_3 was proposed. It was concluded that the addition of Al_2O_3 and Fe_2O_3 enhanced the densification of $MgCr_2O_4$ through solid-solution formation, creation of lattice imperfections, and distortion of the host structure. It was shown that the solid-solution formation during sintering not only resulted in the increased density, but also raised the cold crushing strength of specimens due to the higher atomic mobility at the grain boundaries, which eventually resulted in the bond formation.

In this section, the influence of SnO_2 on the densification of $MgCr_2O_4$ is studied. In comparison to Al_2O_3 and Fe_2O_3, SnO_2 is a tetravalent oxide and its addition to $MgCr_2O_4$ increases the concentration of cation vacancies in the host structure, because there is a charge difference between Sn^{+4} as solute and Cr^{+3} and Mg^{+2} as host cations[122]. According to literature, there is unlimited solid solubility between $MgCr_2O_4$ and Mg_2SnO_4[37]. Therefore, it is expected that the addition of SnO_2 should improve sintering, thus increasing the density of $MgCr_2O_4$. Figure 5-16 shows the effect of SnO_2 on the relative density of $MgCr_2O_4$ sintered in air at 1475°C for 5 hrs. Each data point in this figure represents the average value calculated for 3

samples. As shown, the increase of the SnO_2 content to 10 mol% considerably increased the relative density of $MgCr_2O_4$ from ~51% to ~64%.

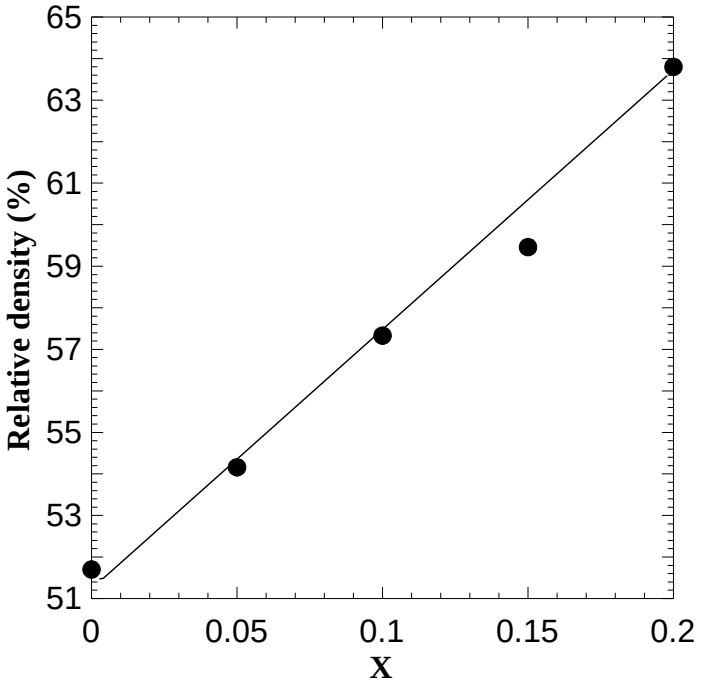

Figure 5-16. The variation of relative density of $Mg[Cr_{1-x}Sn_x]_2O_4$ (x=0, 0.05, 0.1, 0.15, and 0.2) compositions sintered in air at 1475°C for 300 minutes

There is an analogy between this system and the $MgCr_2O_4$-$MgFe_2O_4$ and $MgCr_2O_4$-$MgAl_2O_4$ systems, as there is unlimited solid solubility between the end members; therefore, the same explanations can be used to describe the mechanism by which SnO_2 enhanced the densification of $MgCr_2O_4$.

The *XRD* patterns of SnO_2 containing compositions are shown in Figure 5-17. No new peaks could be identified in *XRD* patterns at higher SnO_2 content. However, the peaks shifted toward the lower angle, indicating that a solid solution has been formed and increased the lattice parameter of $MgCr_2O_4$. This can be explained by the larger effective cationic radius of Sn^{+4} (0.69 Å) than of Cr^{+3} (0.62 Å) and Mg^{+2} (0.57 Å). Mg_2SnO_4 spinel is a normal spinel in which Sn^{+4} occupies octahedral positions and Mg^{+2} tetrahedral sites[37].

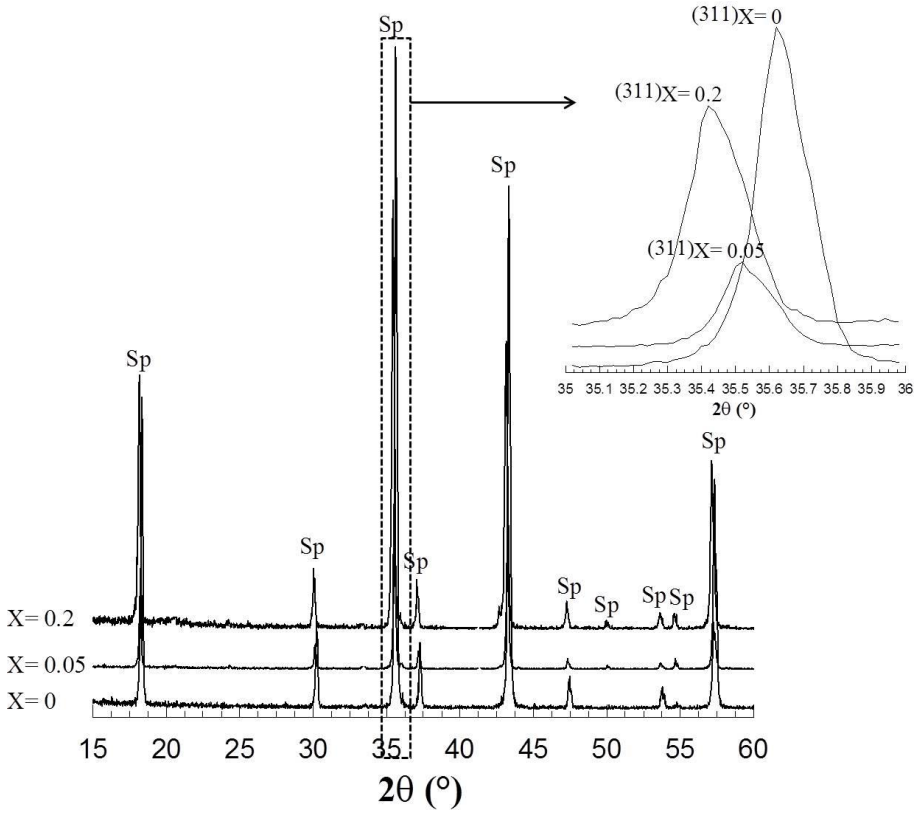

Figure 5-17. *XRD* patterns of $Mg[Cr_{1-x}Sn_x]_2O_4$ (x=0, 0.05, 0.1, 0.15, and 0.2) compositions sintered in air at 1475°C for 300 minutes; Sp: spinel solid solution

The octahedral site preference energy of Sn^{+4} is relatively high; hence it is expected that it sits in the octahedral sites next to Cr^{+3}, or substitutes for Cr^{+3}. The size mismatch causes lattice distortion, which enhances the densification[123]. The addition of SnO_2 results in the formation of cation vacancy in the $MgCr_2O_4$ structure to compensate for the excess charge on Sn^{+4}.

The hypothesized vacancy formation reaction is shown in equation 5-13, which proves that the addition of tin oxide increases the population of vacancies in the spinel structure. It is expected that the increase in the concentration of vacancies enhance both the cation diffusion and densification. Park[124] reported the same results for the sintering of In_2O_3, in which Zn substituted for In and resulted in the formation of oxygen vacancy; subsequently it increased the density of In_2O_3 through increased ionic diffusivity.

$$SnO_2 \xrightarrow{MgCr_2O_4} 3\dot{S}n_{Cr} + V_{Cr}''' + Mg_{Mg} + 2O_O$$ 5-13

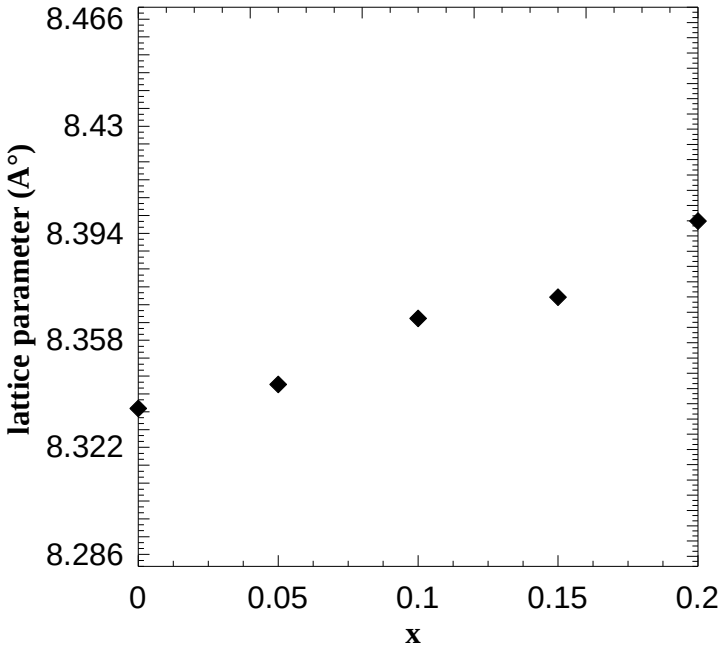

Figure 5-18. The change in lattice parameter of $Mg[Cr_{1-x}Sn_x]_2O_4$ (x=0, 0.05, 0.1, 0.15, and 0.2) compositions sintered in air at 1475°C for 300 minutes

Based on the above, it is concluded that SnO_2 increases the lattice parameter of $MgCr_2O_4$ and enhances the densification of $MgCr_2O_4$ via solid solution formation mechanism. The comparison between the addition of Fe_2O_3, Al_2O_3 and SnO_2 indicates that the formation of solid solution enhances the densification. However, these explanations are not satisfactory to conclude how the inversion phenomenon contributes to the densification of $MgCr_2O_4$. Therefore, the effect of Fe_2O_3 and SnO_2 on the densification of Cr_2O_3 has also been studied.

This experiment was designed since Cr_2O_3 and $MgCr_2O_4$ have similar sintering behaviors and unlimited solid solubility with Fe_2O_3[82,110]. In the presence of the sintering additives, the inversion phenomenon does not occur in Cr_2O_3; however, it should occur in $MgCr_2O_4$ because this phenomenon is defined for spinel structures[37].

5.4 The effect of Fe_2O_3 and SnO_2 on sintering of Cr_2O_3

In this section the effect of tin oxide and iron oxide on the densification of pure Cr_2O_3 has been evaluated. This study is carried out to clarify the contribution of the inversion phenomenon, which is caused by the presence of Fe_2O_3 and Al_2O_3, on the sintering of pure $MgCr_2O_4$. The selection of Cr_2O_3 for the study was due to the fact that on the one hand it has the same sintering behavior and also identical sintering mechanisms with $MgCr_2O_4$[82], and on the other hand the two compounds crystallize in two different crystal structures: $MgCr_2O_4$ has a spinel crystal structure, while Cr_2O_3 has a hexagonal structure[82,125].

In addition, both have a substantial solid solubility with Fe_2O_3 and limited solubility with SnO_2[2]. Therefore, a comparison between the densification of $MgCr_2O_4$-SnO_2 and Cr_2O_3-SnO_2, and $MgCr_2O_4$-Fe_2O_3 and Cr_2O_3-Fe_2O_3 could explain the contribution of the solid solution formation to the densification of $MgCr_2O_4$. In addition, the comparison that has been made between the densification of $MgCr_2O_4$-Fe_2O_3 and Cr_2O_3-Fe_2O_3 could also elucidate the contribution of inversion process to the densification, since inversion phenomenon is only characteristic to the spinel structures. Therefore, if in identical sintering conditions the density of $MgCr_2O_4$-Fe_2O_3 is higher than the density of Cr_2O_3-Fe_2O_3, the excess density is achieved due to the inversion phenomenon induced by Fe_2O_3 in the lattice structure of $MgCr_2O_4$.

Cr_2O_3, Fe_2O_3, and SnO_2 grains with particle size of 1.2µm, similar to particle size of synthesized (1.5µm) $MgCr_2O_4$, were mixed and pressed to make pellets with ~48% green density, identical to that of $Mg[Cr_{1-x}(Fe/Sn)_x]_2O_4$ samples. The pellets were then sintered at 1475°C for 300 minutes, i.e. in the same sintering conditions as for $Mg[Cr_{1-x}(Fe/Sn)_x]_2O_4$.

5.4.1 The effect of SnO_2 on densification of Cr_2O_3

The variation of the relative density of specimens sintered in air at 1475°C for 300 minutes versus the SnO_2 content is shown in Figure 5-19; the relative density of specimens slightly increased from 51.92% (2.70±0.27 g/cm^3) to 58.93% (3.07±0.22 g/cm^3) by increasing the SnO_2 to 0.5 mol%. The further increase in SnO_2 content to 5 mol% decreased the density to a value less than for the pure Cr_2O_3 sample.

The same phenomenon was reported by K.A. Berry[126]: the addition of MgO to alumina raised the density of alumina up to the solid-solubility limit of MgO in Al_2O_3, and then reduced tit below this limit, which was attributed to the solid solution formation as a result of dissolution of the sintering additive in the host structure.

In order to find out if this phenomenon also occurred in the Cr_2O_3-*v*SnO_2 compositions, the *XRD* patterns of the samples with 0.125, 0.25, 0.375, 0.5, 1, and 5 mol% SnO_2 were compared to the pure Cr_2O_3. Figure 5-20 shows the X-ray diffraction patterns of the samples sintered at 1475°C in air for 300 minutes.

A very small shift toward higher angle (by 0.24 degree) is observed in the *XRD* patterns, which is proportional to the SnO_2 content for samples with less than 0.5 mol% SnO_2. This is an indication of the formation of a solid solution between Cr_2O_3 and SnO_2. Since the *XRD* peaks shifted toward high angles, it is concluded that the lattice parameter of the solid solution is smaller than that of Cr_2O_3. Considering the cationic radius of Cr^{+3} (0.62 Å) and Sn^{+4} (0.69 Å)[109], the addition of SnO_2 to Cr_2O_3 resulted in the substitution of Sn^{+4} for Cr^{+3}, accompanied by an increase in the Cr_2O_3 lattice parameter. For compositions with SnO_2 beyond 0.5 mol%, this trend is not valid. An identification peak of SnO_2 is also observed in the diffraction pattern of Cr_2O_3-5mol% SnO_2.

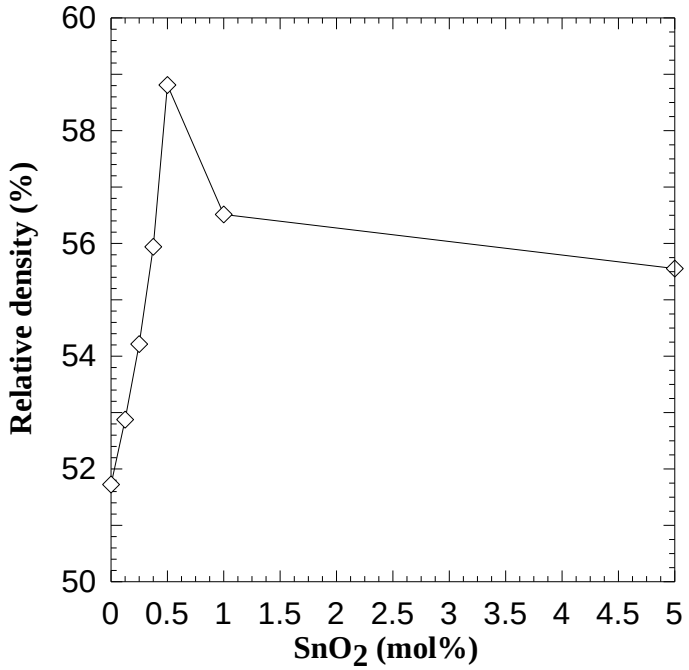

Figure 5-19. The variation in relative density of Cr_2O_3-*v*SnO_2 (*v*=0.125, 0.25, 0.375, 0.5, 1 and 5 mol%) samples sintered in air at 1475°C for 300 minutes

The variation of lattice constant of Cr_2O_3 versus SnO_2 content is presented in Figure 5-21. As shown, the lattice parameter increased to a=4.9653±0.0005 Å and c=13.6948±0.0005 Å, and reached a plateau at 0.5 mol% of SnO_2. The increase in the lattice parameter is attributed to the solid solution formation between Cr_2O_3 and SnO_2. The fact that the lattice parameter is not changing with the increase in SnO_2 content beyond 0.5 mol% is attributed to the precipitation of tin oxide, Figure 5-21. In other words, the solid solubility limit of SnO_2 in Cr_2O_3 is about 0.5 mol% under the sintering conditions. Similar results were reported by D. H. Park et al.[124] who investigated the effect of zinc oxide and defect chemistry on the sintering of In_2O_3.

For compositions with more than 0.5 mol% SnO_2, tin oxide would precipitate on the Cr_2O_3 grains or the grain boundaries. The *SEM* images of the fracture surface of Cr_2O_3-0.5 SnO_2 and Cr_2O_3-5SnO_2 sintered at 1475°C are shown in Figure 5-22.

These images demonstrate that 0.5mol% tin oxide is dissolved in to the Cr_2O_3 lattice; in contrast, for the Cr_2O_3-5SnO_2 compositions, SnO_2 precipitated inside the grains and at the grain boundaries of Cr_2O_3.

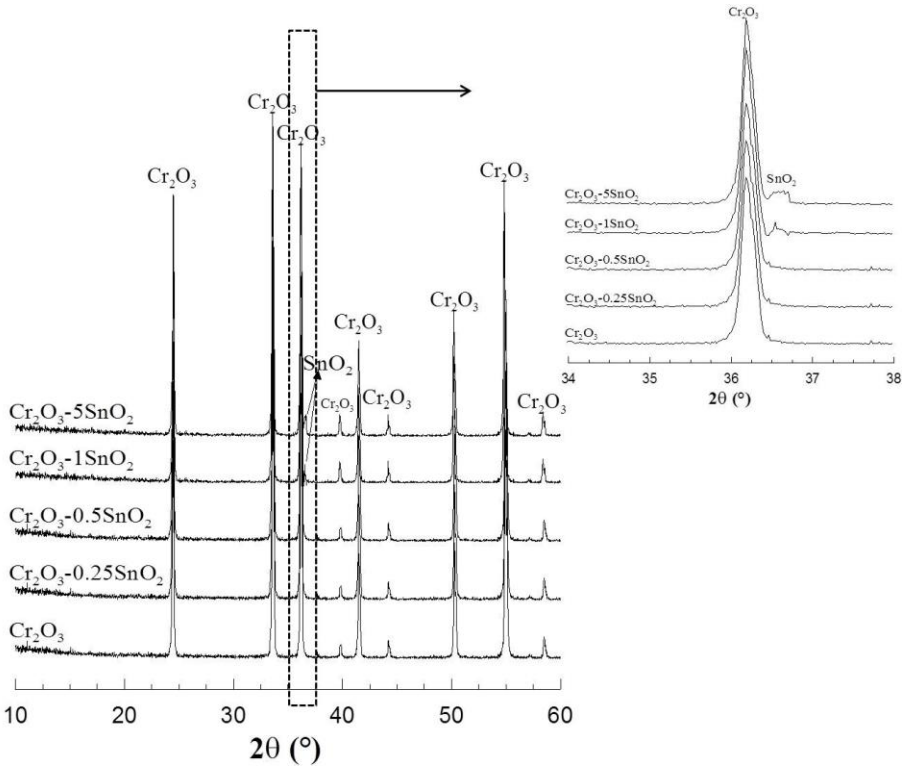

Figure 5-20. *XRD* patterns of Cr_2O_3-*v*SnO_2 (*v*=0.125, 0.25, 0.375, 0.5, 1, and 5 mol%) samples sintered in air at 1475°C for 300 minutes

According to these results, up to 0.5 mol% tin oxide formed a solid solution with Cr_2O_3 and enhanced its densification. SnO_2 possibly formed cation vacancies in chromia and thus enhanced the diffusion and densification. The following reaction is proposed for the cation vacancy formation:

$$SnO_2 \xrightarrow{Cr_2O_3} 3\dot{Sn}_{Cr} + V_{Cr}''' + 2O_O^x \qquad 5\text{-}14$$

Further increase in SnO_2 resulted in the precipitation of SnO_2 on Cr_2O_3 grains and grain boundaries and adversely affected the densification process. The presence of the precipitates

could have decreased the grain boundary energy[127]. Since the maximum density in this set of samples is less than 60±0.1 %, the precipitation could not enhance the densification. For the Cr_2O_3-*v*SnO_2 system, the chromium vapor pressure at temperatures above 1200°C is relatively high (i.e. 0.232 Pa at 1400°C). For the processing conditions where the material's porosity is still high (40-50%) and the fraction of grain/grain contacts is limited, surface diffusion and evaporation/condensation mechanisms could dominate the mass transport mechanism, and thus control the sintering process. For this reason, for compositions with more than 0.5 mol% SnO_2, the densification decreases.

The comparison between these results and the densification behavior of $MgCr_2O_4$ in the presence of SnO_2 sheds light on the effect of solid solution formation on the densification of Cr_2O_3 and $MgCr_2O_4$.

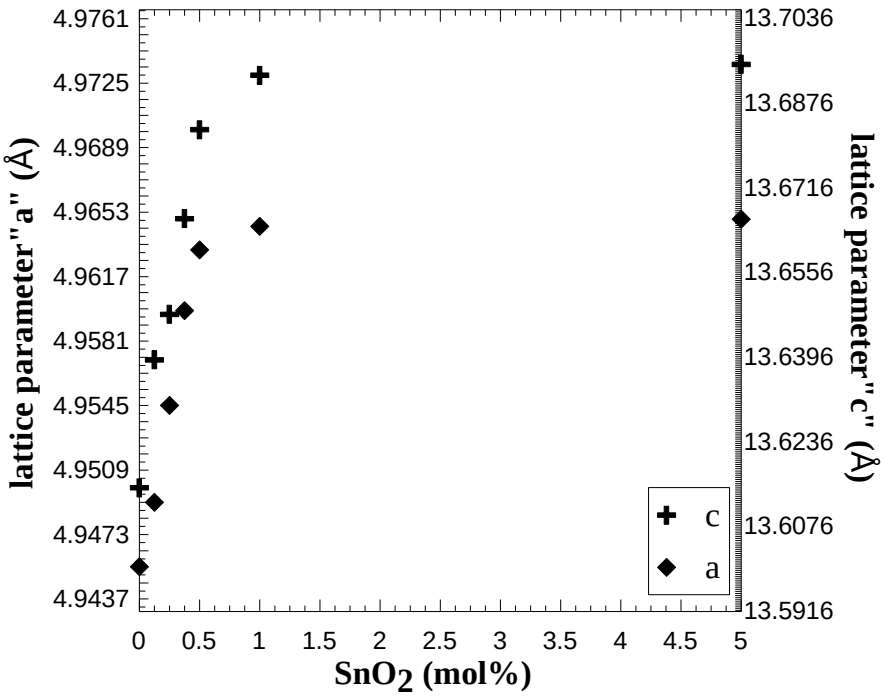

Figure 5-21. The influence of SnO_2 content on the lattice parameter of Cr_2O_3 sintered at 1475°C for 300 minutes in air.

The increase in SnO_2 content continuously increased the density of $MgCr_2O_4$ as a result of the unlimited solid solubility between $MgCr_2O_4$ and Mg_2SnO_4. In contrast, density increased to a maximum with the increase in tin oxide content up to 0.5 mol%, and decreased with further SnO_2 additions. This behavior is attributed to the effect of the solid solution formation on the sintering of ceramics, since the solid solubility of SnO_2 in Cr_2O_3 is shown to be 0.5 mol%.

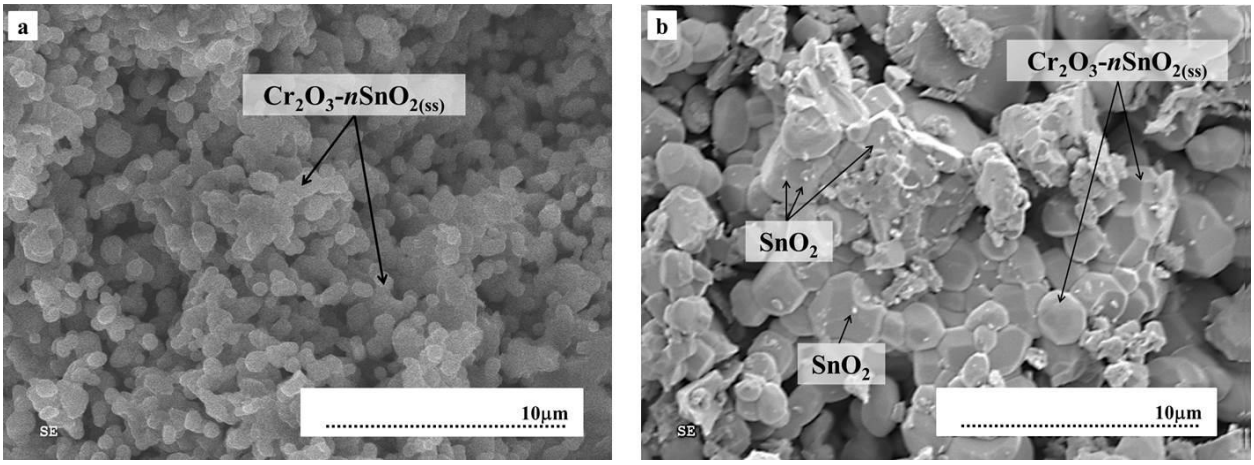

Figure 5-22. Microstructure of the fracture surface of sintered Cr_2O_3-*n*SnO_2 (*n*= 0.5 and 5 mol%) samples sintered in air at 1475°C for 300 minutes

5.4.2 The effect of Fe_2O_3 on the densification of Cr_2O_3

Figure 5-23 shows the variation of relative density of Cr_2O_3-*v*Fe_2O_3, (*v*: 1, 2.5, 5, 7.5 and 10 mol%) compositions sintered at 1475°C in air for 300 minutes. The reported relative density is the average density of three samples. The errors are calculated based on $\sigma/\sqrt{3}$ and are about 0.5%. Considering the experimental errors, the relative density gradually increased with the increase in Fe_2O_3 content, indicating that the Fe_2O_3 enhances the sintering of Cr_2O_3.

A phase diagram of Cr_2O_3-Fe_2O_3 was constructed using the Factsage software to find out the reasons for this behavior. Based on the phase diagram, shown in Figure 5-24, there is unlimited solid solubility between these oxides.

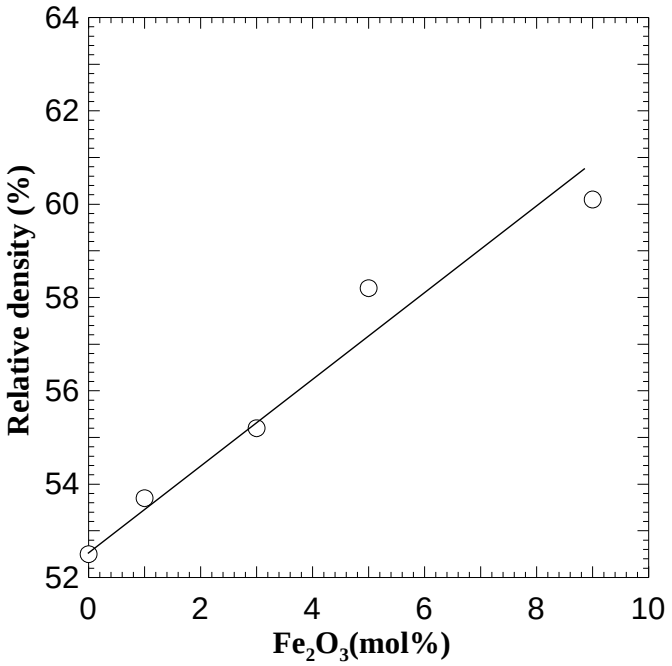

Figure 5-23. The variation of relative density of Cr_2O_3-*v*Fe_2O_3 composition with Fe_2O_3 content sintered in air at 1475°C; the error bars are smaller than symbols

Formation of solid solution can improve the densification in two ways. First, the formation of solid solution creates lattice distortion due to the size mismatch between solute and host atoms/ ions; this affects their diffusivity and densification. Second, it can create lattice imperfections such as ion vacancies or interstitials of both ion types, if there is a charge difference between solute and the host ion in the ceramic material. In the case of Cr_2O_3 and Fe_2O_3, since there is no charge difference between Cr and Fe, no vacancy would form in Cr_2O_3 as a result of Fe_2O_3 addition. However, due to the size difference between Fe^{+3} (0.67 Å) and Cr^{+3} (0.62 Å) a substantial lattice distortion is induced in Cr_2O_3, which could possibly enhance

densification. Therefore, the increase in the solid solution content as a result of Fe_2O_3 addition is attributed to this sintering behavior.

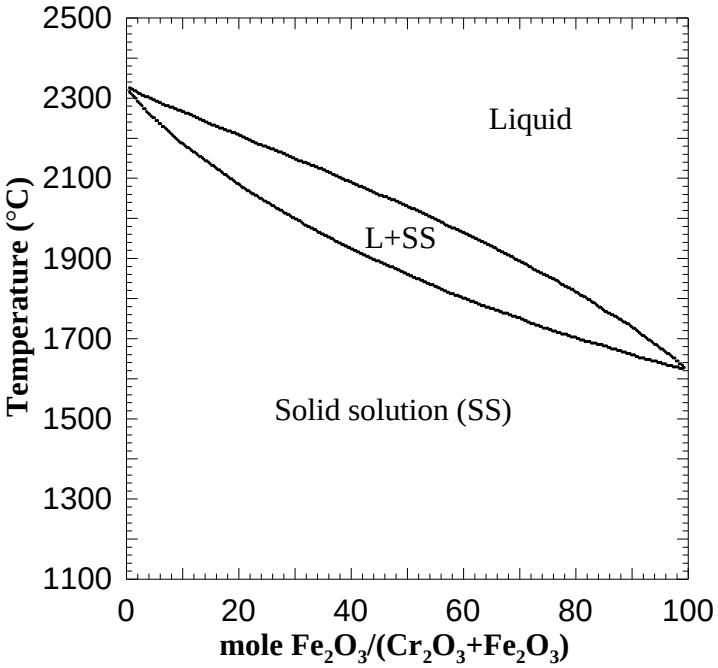

Figure 5-24. Cr_2O_3-Fe_2O_3 phase diagram; reprinted from Factsage results

As explained earlier, the main purpose of this experiment was to explore the contribution of the inversion phenomenon to the sintering of $MgCr_2O_4$. In this regard, the effect of solid solution formation on the sintering of $MgCr_2O_4$ was explained by comparing the results of the sintering of $MgCr_2O_4$-SnO_2 and Cr_2O_3-SnO_2. In order to differentiate between the contribution of solid solution formation and the inversion during sintering of $MgCr_2O_4$, a comparison between the results of the densification of $MgCr_2O_4$-Fe_2O_3 and Cr_2O_3- Fe_2O_3 has been made.

In both systems there is unlimited solid solubility between the end-members. They also form different crystal structures. $MgCr_2O_4$ crystallizes in the spinel form and Cr_2O_3 in the hexagonal form. In addition, $MgCr_2O_4$ and Cr_2O_3 have similar sintering behaviors; therefore, any

differences between their densification behaviors in the presence of Fe_2O_3 can be attributed to the inversion phenomenon. Figure 5-25 shows the densification of Cr_2O_3 and $MgCr_2O_4$ versus Fe_2O_3 content; the density of both $MgCr_2O_4$ and Cr_2O_3 has shown to be proportional to the Fe_2O_3 content. Although the density of pure $MgCr_2O_4$ is similar to the density of Cr_2O_3, the rate of increase in density of $MgCr_2O_4$ with Fe_2O_3 is considerably higher than that of Cr_2O_3. In other words, the density of $MgCr_2O_4$ is more than that of Cr_2O_3 for the samples with same Fe_2O_3 content. According to the above discussion, the difference between the densities is attributed to the inversion phenomenon, which only occurred in spinel structure.

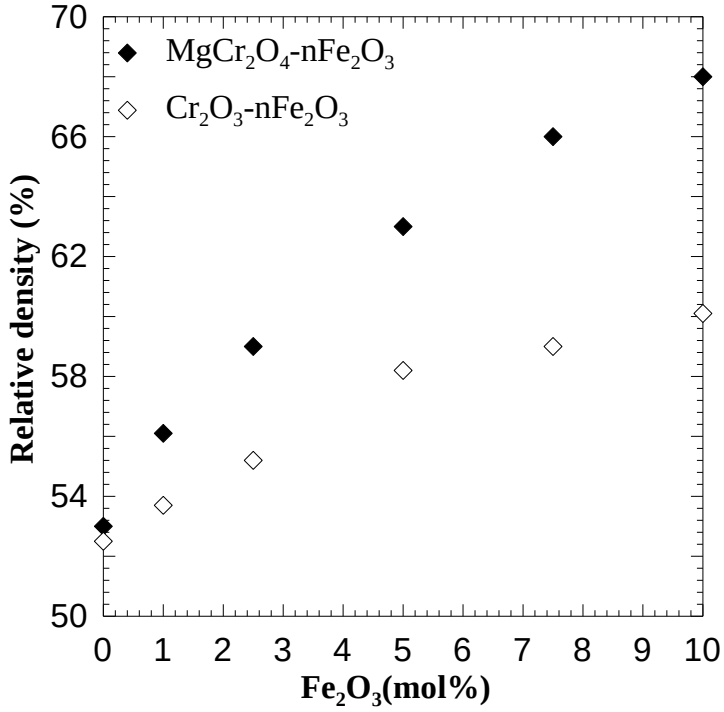

Figure 5-25. The densification of Cr_2O_3 and $MgCr_2O_4$ versus Fe_2O_3 content. The samples were sintered at 1475°C in air for 300 minutes

It is concluded that the inversion process is considerably important in the sintering of $MgCr_2O_4$ with a spinel structure. In Section 5.2 it was demonstrated that the inversion process

could result in either the reduction or the increase in the volume of tetrahedral and octahedral sites in the spinel lattice, depending on the size of the interchanging cations. In the case of Fe_2O_3, as Fe^{+3}(0.67 Å) is larger than Mg^{+2} (0.57 Å), it induces stress on the cations in octahedral sites and thus perhaps increases the driving force for movement of the cations from neighboring octahedral sites to other sites. In contrast, the addition of Fe_2O_3 to Cr_2O_3 could only enhance the densification, as it only slightly induces distortion to the Cr_2O_3 lattice due to the size mismatch. Therefore, it is hypothesized that the inversion phenomenon enhanced the sintering of the $MgCr_2O_4$.

Chapter 6. The effect of spinel forming oxides on the sintering of magnesia-chromite composites

6.1 Introduction

In the previous section the effect of various sintering additives on the crystal structure and the sintering of $MgCr_2O_4$ have been studied. It was shown that the effectiveness of sintering additives increases with the increase in solid solubility and the degree of inversion induced by the additive. Based on the results of this study, Fe_2O_3 is selected as the most effective and SnO_2 as the least effective sintering additives. The main reason for the different performance of SnO_2, Al_2O_3 and Fe_2O_3 is explained by the induced degree of inversion.

SnO_2 forms a normal spinel solid solution, $Mg[Cr_{1-x},Sn_x]_2O_4$ with $MgCr_2O_4$ regardless of temperature and SnO_2 content. Al_2O_3 and Fe_2O_3 both form partially inverted spinel solid solutions, $(Mg_{1-\xi},Al_\xi)[Cr_{2-2NA},Mg_\xi,Al_{2NA-\xi}]_2O_4$ and $(Mg_{1-\xi},Fe_\xi)[Cr_{2-2NA},Mg_\xi,Fe_{2NA-\xi}]_2O_4$ respectively, but Fe^{+3} introduced more inversion to the $MgCr_2O_4$ structure and resulted in more atomic mobility and eventually more densification under similar sintering conditions.

The main purpose of this study was to sinter magnesia-chromite composites at temperatures below 1500°C for refractory applications. Therefore, the reduction in the sintering temperature, the phase assemblage and the microstructure of the sintered composite should be all considered in the composite design. $MgCr_2O_4$ can withstand the contact with bottom blown oxygen convertors (BBOC)[*] slag at 1100-1200°C, but MgO, $MgAl_2O_4$ and especially $MgFe_2O_4$ dissolve very fast in the slag in the same conditions. In magnesia-chromite refractory composites

[*] The average composition of the BBOC slag is: Ag: 37%, As: 0.2%, Sb: 3.3%, Pb: 7.4%, Bi: 47%, and Cu: 0.4%. It should be mentioned that these elements are in oxide form due to the working conditions of BBOC.

MgO, $MgAl_2O_4$ and $MgFe_2O_4$ form a solid solution with the host structure, $MgCr_2O_4$, and therefore are expected to have less reactivity with the slag than the pure compositions. The higher the content in the solid solution, the more the formed solid solution is prone to dissolve in the slag.

Based on the obtained knowledge of the influence of the selected sintering additives and of the crystal structure on the densification of $MgCr_2O_4$, as well as on the sintering behavior of MgO and chromite from literature, 12 magnesia-chromite composites, coded *MK*1 to *MK*12, were designed (Table 5-2). The primary goal of designing the 12 composites was to understand the effects of Fe_2O_3 and Al_2O_3 on their sintering behavior, and to optimize the Fe_2O_3, Al_2O_3 and Cr_2O_3 content in the compositions. As shown in Table 6-1, *MK*1-*MK*4, *MK*5-*MK*9 and *MK*10-*MK*12 were designed to evaluate the effect of Cr_2O_3, Al_2O_3, and Fe_2O_3 content on the sintering of magnesia-chromite composites respectively. The range of the Cr_2O_3, Fe_2O_3, and Al_2O_3 content was set based on the composition of industrially available fused chromite grains, and with the intention of keeping the value of Fe_2O_3 below 10 wt% in the composition. Based on the previous studies, the presence of more than 10wt% Fe_2O_3 in the refractory composites negatively affects their performance.

In order to study the effect of each oxide on the densification of magnesia-chromite refractory composites, a comparison has been made between the relative densities of all magnesia-chromite refractory compositions which were sintered at 1550°C for 300 minutes. Based on these results, 4 composites were selected for further non-isothermal sintering studies. The best composition was nominated based on the densification results and used for the sintering kinetics studies.

Table 6-1. The composition of designed magnesia-chromite refractory composites

	MgO (mole%)	Al_2O_3 (mole%)	Fe_2O_3 (mole%)	Cr_2O_3 (mole%)
MK1	85.49	6.9	2.71	4.9
MK2	84.49	6.9	2.71	5.9
MK3	83.49	6.9	2.71	6.9
MK4	82.49	6.9	2.71	7.9
MK5	81.49	6.9	2.71	8.9
MK6	85.49	4.9	2.71	6.9
MK7	84.49	5.9	2.71	6.9
MK8	82.49	7.9	2.71	6.9
MK9	81.49	8.9	2.71	6.9
***MK*10**	81.49	6.9	3.71	6.9
***MK*11**	82.49	6.9	1.71	6.9
***MK*12**	84.49	6.9	0.71	6.9

The typical morphology of the synthesized magnesia-chromite refractory composites is shown in Figure 6-1. For compositions with high content of Fe_2O_3 or Al_2O_3 the particles are in the form of hexagons and cubes with rounded edges. In contrast, samples with high Cr_2O_3 have sharp corners and are slightly smaller. The particle and grain size of selected magnesia-chromite refractory composites are measured by *SEM* and *XRD* respectively, and the results are listed in Table 6-2.

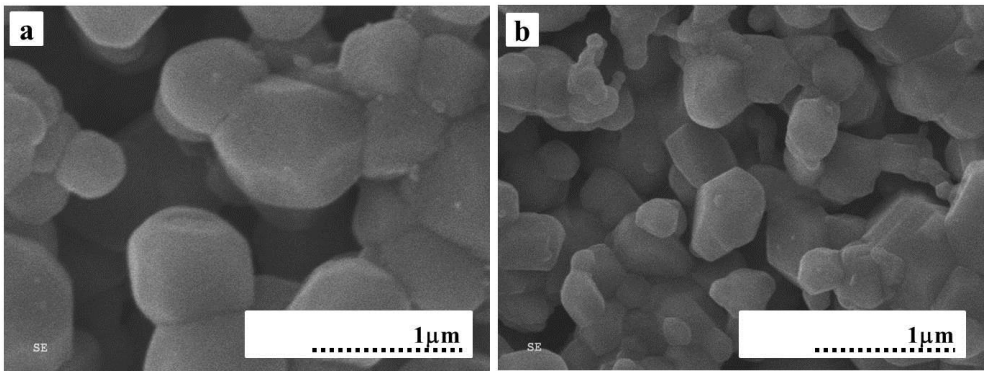

Figure 6-1. The typical microstructure of synthesized magnesia-chromite composites; a) the lowest Cr/Al+Fe ratio (*MK*1), and b) the highest Cr/Al+Fe ratio (*MK*6)

As expected, the differences between the particle sizes of different composites are in the range of 15-20 % of the smallest particle. For this reason the effect of initial particle size on the densification of magnesia-chromite refractory composites was not incorporated in the interpretation of the results.

Table 6-2. Particle size of selected magnesia-chromite composites after calcination at 850°C

	Particle size (μm)
MK1	1.12
MK3	1.27
MK6	1.34
MK12	1.19

6.1.1 The effect of Fe_2O_3 on the densification and grain growth of magnesia-chromite refractory composites

Figure 6-2 illustrates the density variation versus the Fe_2O_3 content of the composites. The increase in Fe_2O_3 increases the density of magnesia-chromite refractory composites sharply from 83% to 95% of theoretical density. The same behavior was observed during sintering of pure $MgCr_2O_4$ and was attributed to the solid solution formation and the inversion process of the formed spinel solid solution. The microstructure of the magnesia-chromite refractory composites consists of two phases which are soluble in each other; therefore, the same analogy can be considered for this behavior.

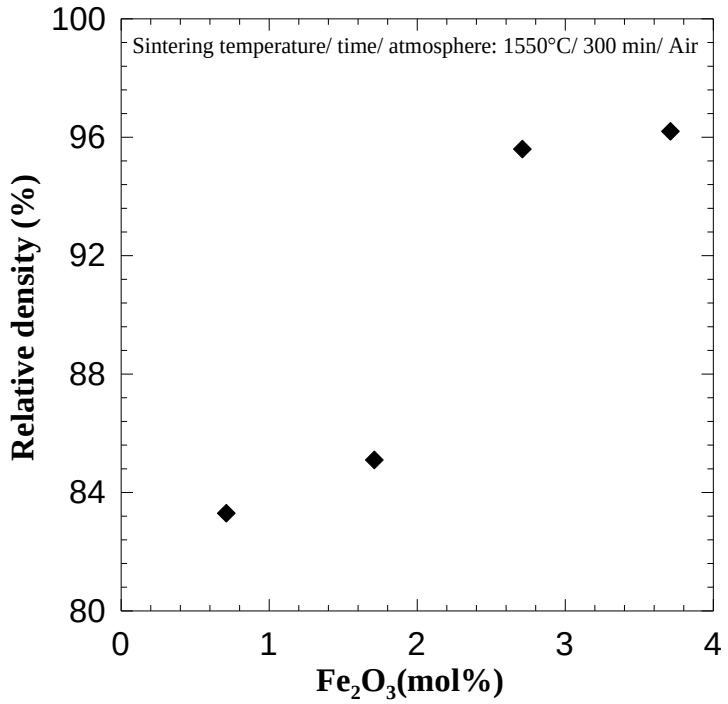

Figure 6-2. The variation of relative density of magnesia-chromite refractory composites versus Fe_2O_3 content; composites sintered at 1550°C for 300 minutes

Figure 6-3 shows the *XRD* patterns of the *MK*3 composite air quenched from the sintering temperature of 1550°C. The formation of spinel (*Sp*) solid solution can be confirmed by the shift toward high diffraction angles recorded for the [101] peak of MgO. The BSE microstructure of polished and thermally etched *MK*3 composites is shown in Figure 6-4. It is seen that the microstructure is composed of two phases; the darker phase is MgO with 3% Fe_2O_3, 0.2% Al_2O_3 and 3.6% Cr_2O_3 as solutes, and the brighter phase is a spinel solid solution.

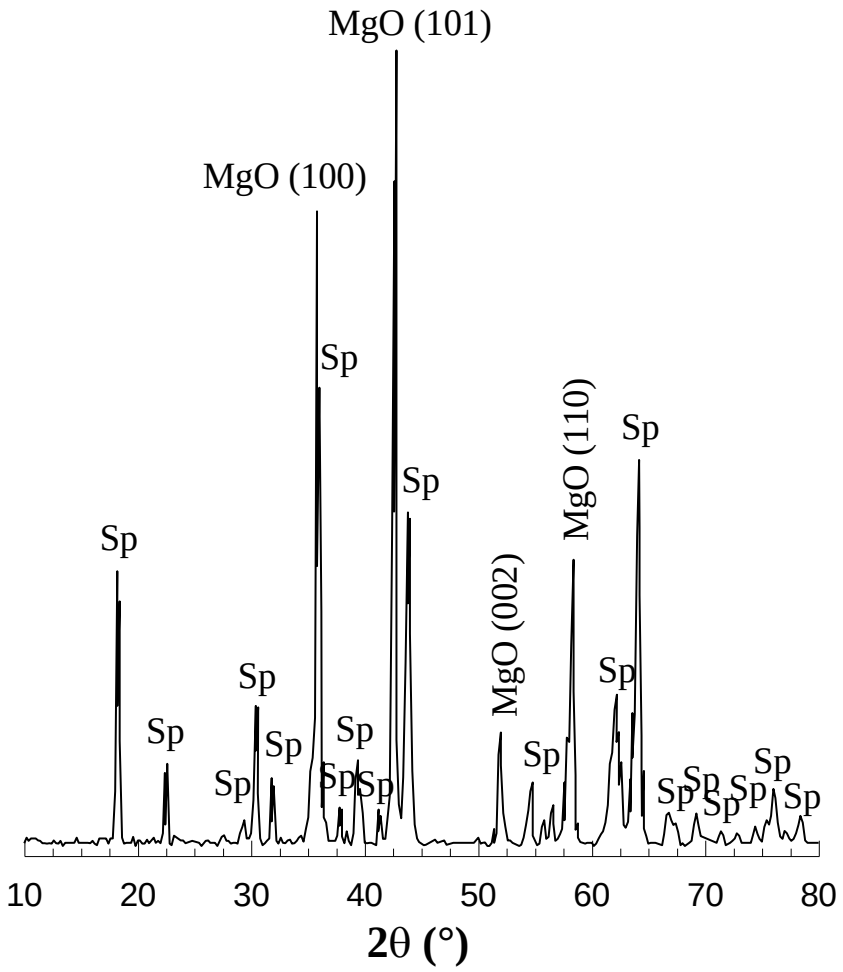

Figure 6-3. The *XRD* of *MK*3 composite sintered at 1550°C for 5 hours;

***Sp*: $(Mg_{1-x-y},Fe_y,Al_x)[Cr_{2-x-y},Al_x,Fe_y,Mg_{x+y}]O_4$; $\xi = x+y$**

A closer examination of the chromite grains, Figure 6-4, shows the presence of a brighter rim around the spinel grains; the Fe_2O_3 content is higher in the spinel grains and at the MgO/spinel interfaces (rim). Al_2O_3 is concentrated in the spinel grains and its concentration is ~0.22% in the center of the selected MgO grains. Similar observations were reported by Stubican and Menezes[128]. They presented that there was a difference between the diffusion of Fe, Cr, and Al from chromite grains to magnesia grains.

The large amount of iron, limited amount of chromium and almost no aluminum was reported to have diffused from chromite into magnesia at 1400°C[128]. This phenomenon can also

be predicted from the respective phase diagrams. Figure 6-5 shows a part of the phase diagrams of $MgO\text{-}MgAl_2O_4$, $MgO\text{-}MgFe_2O_4$, and $MgO\text{-}MgCr_2O_4$[2].

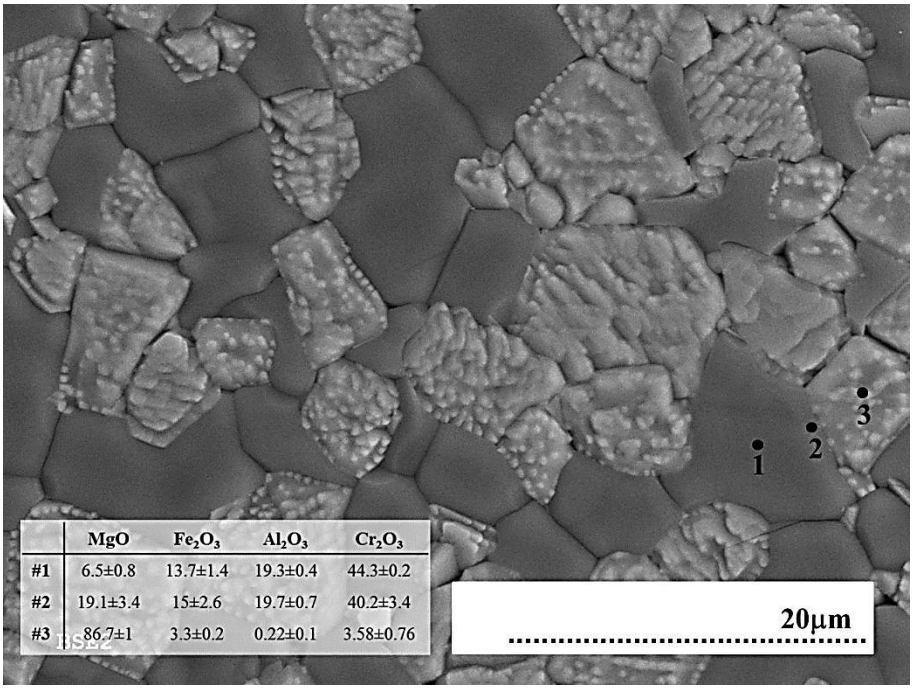

	MgO	Fe_2O_3	Al_2O_3	Cr_2O_3
#1	6.5±0.8	13.7±1.4	19.3±0.4	44.3±0.2
#2	19.1±3.4	15±2.6	19.7±0.7	40.2±3.4
#3	86.7±1	3.3±0.2	0.22±0.1	3.58±0.76

Figure 6-4. BSE image of *MK*3 sintered at 1550°C for 300 minutes; inset shows the *EDS* analysis of the selected points; the confidence intervals were obtained based on the $\sigma/\sqrt{3}$ equation for flat distribution, as each point has been analyzed 3 times

It is observed that at high temperatures Al_2O_3, Cr_2O_3 and Fe_2O_3 are partially soluble in MgO and their solubility increases with temperature, while the solubility decreases in the order $Fe_2O_3 >> Cr_2O_3 > Al_2O_3$ at temperatures above 1000°C. Therefore, the shift in the MgO peak is attributed to the formation of MgO solid solutions at the sintering temperature. At 1550°C, some of Fe_2O_3 and Cr_2O_3, which are in the form of spinel, are dissolved into MgO and form a MgO solid solution. The diffusion of Fe and Cr into MgO results in the formation of V''_{Mg} vacancy in MgO through the following reaction, in which *M*e is Fe or Cr, and increases the diffusion rate of cation in the MgO lattice, and subsequently the densification:

$$Me_2O_3 \xrightarrow{MgO} 2\dot{M}e_{Mg} + V''_{Mg} + 3O_O^x$$ 6-1

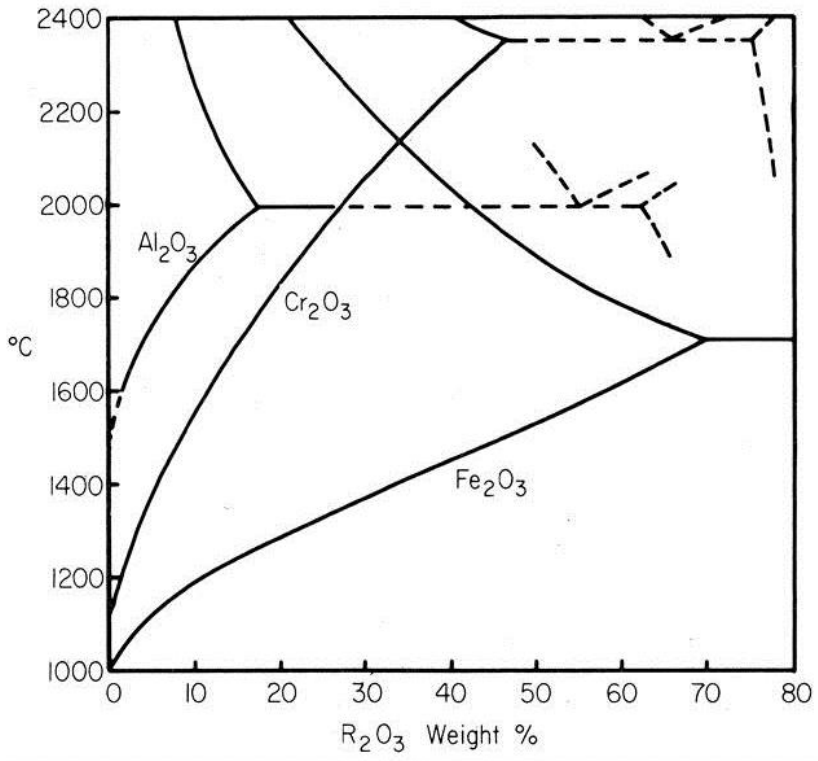

Figure 6-5. Solid solubilities of sesquioxides in periclase at high temperatures[2]

Figure 6-6 illustrates the variation of the relative density of *MK*3 and *MK*12 composites during non-isothermal sintering from 900 to 1600°C at an approximate heating rate of 20 deg/min). For both composites the density increases with temperature, but at temperatures above 1250°C the density of *MK*3 is significantly higher than the density of *MK*12. In addition, the increase in density for *MK*3 can be fitted to the "S" curve, but not for *MK*12 (i.e. it appears that the density increase saturation at 98-99% could occur at temperatures significantly higher than 1600°C).

The "S" curve pattern of density with sintering temperature indicates that the *MK*3 composite experienced all three steps of the sintering process[4]. At temperatures below 1150°C,

density barely changed with an increase in the sintering temperature resembling the initial stage of sintering. In the intermediate stage, the density sharply rose to 90% of theoretical density with a 250°C increase in the sintering temperature (from 1200 to 1450°C) and in the final stage it reached 98% of the theoretical density above 1500°C. In contrast, for *MK*12 the initial stage of sintering extended to about 1300°C, and the density increased to 84% of theoretical density at 1600°C. This indicates that two different mechanisms control the densification of *MK*3 and *MK*12.

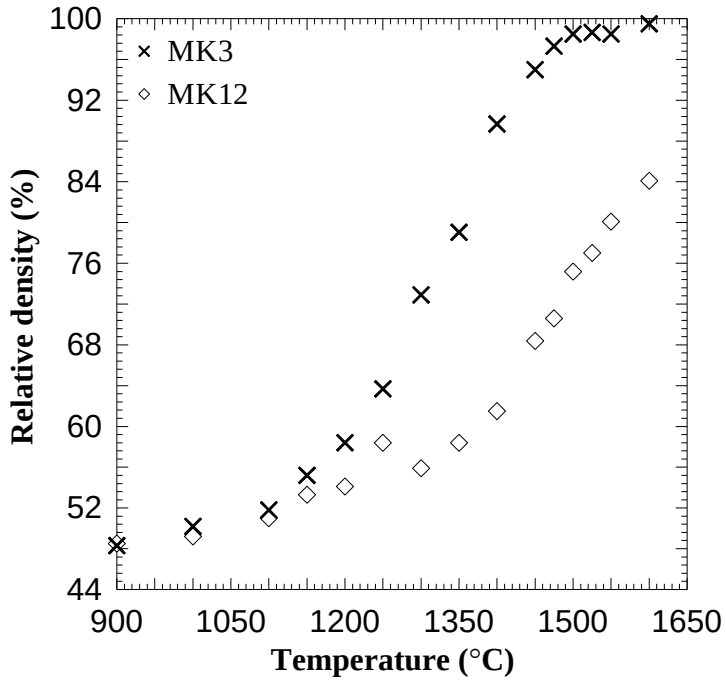

Figure 6-6. The non-isothermal densification of *MK*3 and *MK*12 composite sintered in air at different temperatures for 300 minutes

In the interpretation of the densification and grain growth results for these composites, it should be considered that there is about 40 wt% spinel in the composition of the magnesia-chromite refractory composites; according to Karpinos et al.[129] this affects the kinetics of magnesia-chromite refractory composites densification. They showed that the kinetics of sintering of two-phase composites depends on both the volume fraction and the morphology of

the second phase. For instance, they presented that for copper-ZrC composites the higher the ZrC content and ZrC particles aspect ratio, the lower the final density of the composite[129]. Boltona et al.[130,131], and Fan et al.[131] also showed that densification and the grain growth were affected by the presence of the second phase in the microstructure. They stated that the sintering behavior of the second phase must be taken into account when studying of kinetics of densification and grain growth of a composite.

In this regard, the effect of the composition on the densification of the second phase, which is a solid solution of $MgCr_2O_4$-$MgAl_2O_4$-$MgFe_2O_4$, must be considered when analyzing the results of the densification of the magnesia-chromite refractory composites. Earlier in this work in Chapter 5, it was described that the solid solution formation increases the cation mobility via different mechanisms, including vacancy formation, stress induction, etc., and this increases the densification. In this case, since Fe_2O_3 has high solubility in MgO, the higher the Fe_2O_3 content in magnesia-chromite refractory composites, the more solid solution is formed in the composite, which results in higher densification. In Section 5.2 we have shown that the Fe_2O_3 not only enhances the densification of pure $MgCr_2O_4$ via solid solution formation, but it also contributes to densification due to the induced inversion in the host "$MgCr_2O_4$" structure.

We showed that regardless of the sintering temperature, an inverse spinel solid solution $(Mg_{1-\xi}, Fe_{\xi})$ $[Cr_{1-x}, Mg_{\xi}, Fe_{\xi-x}]_2O_4$ forms . Since the inversion is associated with the short range of cation mobility, we proposed that this reduces the activation energy of the sintering of $MgCr_2O_4$. The same analogy can be applied for magnesia-chromite refractory composites. The only difference is that in the magnesia-chromite refractory composites, both Al_2O_3 and MgO are present in the composition. As a result, the contribution of Al_2O_3 in the inversion of the spinel should be taken into account.

A comparison between the compositions of *MK*3 and *MK*12 shows that they both have the same Cr_2O_3 and Al_2O_3 content, and the difference between them is limited to the Fe_2O_3 content. Based on the above explanations, the higher content of Fe_2O_3 in the composition of *MK*3 resulted in a better densification of *MK*3 than of *MK*12. As shown in Figure 5-13, the presence of about 2 mol% excess Fe_2O_3 in *MK*3 significantly increases the inversion parameter in the spinel. Considering the kinetics of sintering of the two-phase magnesia-chromite refractory composites and the enhancement of densification of MgO and spinel by Fe_2O_3, it can be concluded that the composites with higher Fe_2O_3 content densify better than the others.

The variation of the grain size of *MK*3 and *MK*12 with the sintering temperature is presented in Figure 6-7. The grain size increased with temperature for both composites; however, the final grain size of *MK*3 is larger than in *MK*12. In fact, considering the ±0.7 μm confidence interval for the average grain sizes for the two compositions, it appears that the materials are similar at low temperatures and the differences are visible only at 1600°C. Considering the errors in grain size measurements, Figure 6-7 demonstrates that increasing Fe_2O_3 from 0.71 (*MK*12) to 2.71 mol% (*MK*3) resulted in about 10% increase (d_{ave}: 5.5 to 6 μm) in the average grain size of both spinel and magnesia; however, an opposite trend, reduction in grain size by adding solute, is expected. According to the classic theory of the grain growth[4], the presence of a second phase, here the spinel, should have also suppressed the grain growth of MgO. This anomaly can be explained from two perspectives.

Let's consider the grain growth via the interface migration under the chemical non-equilibrium status. At high temperatures, multiphase polycrystalline solids become chemically unstable, and as a result equilibration reactions occur to reach the new equilibrium condition. These reactions usually occur by diffusion, effecting boundary movement from one grain to

another, and causing grain growth in the first grain at the price of consuming the second grain; this results in the formation of a new solid solution behind the migrating boundary[1,4]. In *MK*3 composites, as shown in Figure 6-14, the grain boundaries are curved, indicating the non-equilibrium conditions at the grain interfaces. The chemical analysis of the grains, displayed in Figure 6-4, shows a difference in the chemical potential of Fe at the spinel/MgO interfaces, which acts as a driving force for the grain growth. As a result, the increase in Fe_2O_3 content increases the driving forces for grain growth and increases the grain size.

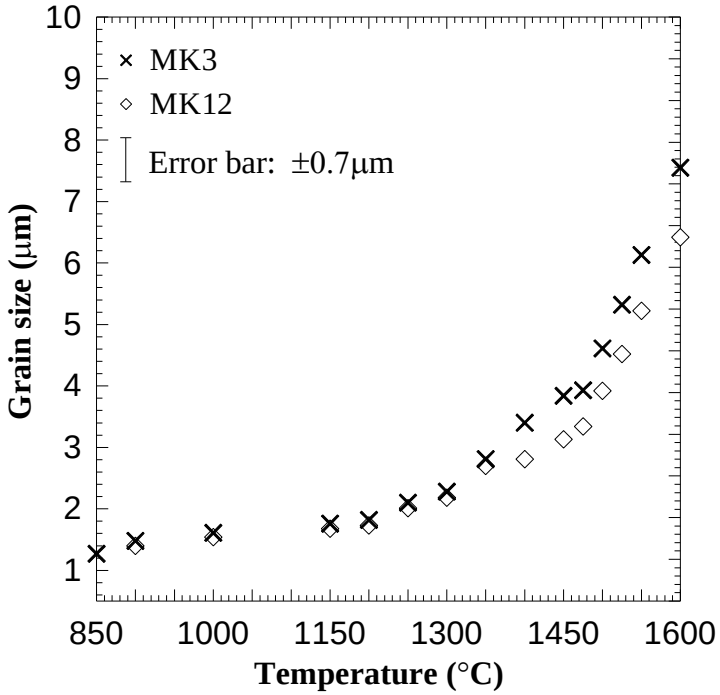

Figure 6-7. Grain size of *MK*3 and *MK*12 composites sintered in air at different temperatures for 300 minutes

The second perspective proposes that in two-phase composites the activation energy for grains coarsening is related to the reduction of the grain boundary energy between the same-phase grains, and also to the reduction of the interphase boundary energy between unlike grains[131]. This occurs via grain growth through grain boundary migration and Ostwald ripening

processes. The Ostwald ripening is a long range diffusion process, while the grain boundary migration requires a short distance diffusion of atoms between two sides of the grain boundary. Therefore, Oswald ripening is the rate controlling mechanism of grain growth in two-phase composites. As a result, the solid solubility of the two phases in each other plays a significant role in the grain growth of the composite. It is therefore proposed that the slightly larger grain size in *MK*3 composites could be caused by the higher Fe_2O_3 content in comparison to the *MK*12 composites.

As shown in Figure 6-5, the high amount of Fe_2O_3 in the spinel results in a high degree of solid solubility, and hence more active Oswald mechanism, and larger grain sizes of both MgO and spinel. Due to the errors in grain size measurement and limited data, at the present stage of this research it is not possible to reach definite conclusions from the above results.

6.1.2 The effect of Cr_2O_3 on densification and grain growth of *MK* composites

The variation of relative density of magnesia-chromite refractory composites with the Cr_2O_3 content is shown in Figure 6-8. It should be mentioned that in this series the compositions of Fe_2O_3 and Al_2O_3 are constant, and the changes in Cr_2O_3 content are balanced with MgO. The effect of Cr_2O_3 on the densification of magnesia-chromite composites and on the microstructure features of the spinel and MgO have been evaluated and used as a base for the interpretation of the results.

Two different trend-lines are fitted to the results in Figure 6-8. Based on the first trendline, density decreases with the increase in Cr_2O_3 content. According to the second trendline, dash line, the trend of change in density with Cr_2O_3 content is also diminishing, but there is a sharp increase in the density of the magnesia-chromite refractory composite with 6.9 mol%. The density dropped from 96±0.3% to ~92±0.3% with 1 mol% increase in Cr_2O_3 content, and then

rose sharply to 96±0.3% and dropped to ~84% of theoretical density with the continuous increase of Cr_2O_3 to 8.9 mol%.

This behavior can be explained by the different oxidation rates of chromia in the presence of other composite constituents. In an investigation by Warshaw and Keith[132], it has been shown that temperature, partial pressure of oxygen, Cr_2O_3 content, and the composition of the composites containing Cr_2O_3 solid solutions influence the vaporization intensity of Cr_2O_3.

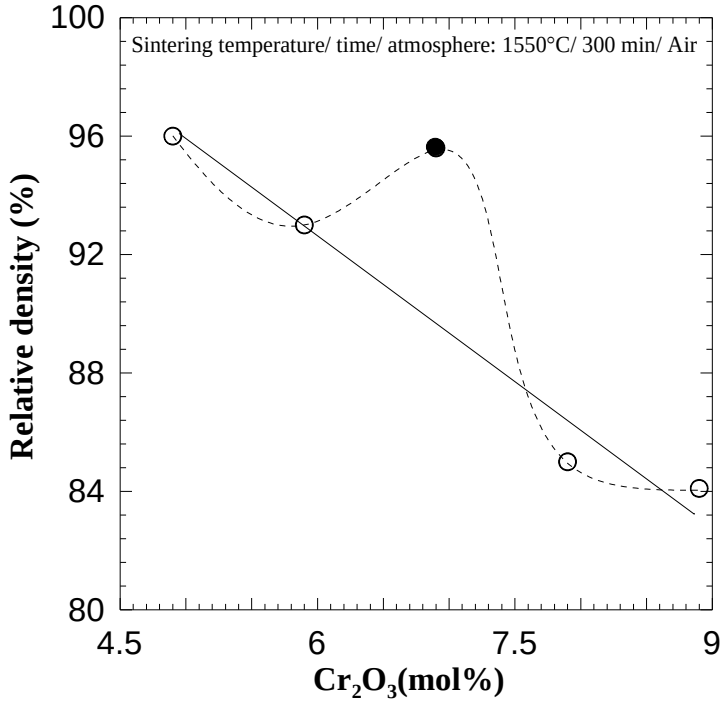

Figure 6-8. Variation of density of magnesia-chromite refractory composites as a function of Cr_2O_3 content; the error bars are smaller than the symbols sizes

In the same study, it was reported that at a given condition, the presence of Al_2O_3 and MgO increases the evaporation of chromium. In contrast, the addition of the SiO_2 reduced chromium evaporation. They explained this observation based on MgO increasing the ratio of Cr^{+3} to Cr^{+2} in a composition. Cr^{+3} is unstable at both high temperatures and oxygen partial pressures, oxidizes to Cr^{+4} and leaves the composition; therefore, the increase in MgO causes the enhanced

vaporization of Cr_2O_3[132]. Sata and Lee[133] reached the same conclusion when studied the vacuum vaporization of $MgCr_2O_4$. They showed that at a given condition the vaporization of $MgCr_2O_4$ is higher than that of MgO and Cr_2O_3.

Based on the above discussion, the reduced density due to the increase in Cr_2O_3 content is attributed to the higher vaporization of chromium, which is detrimental for density. However, at 6.9 mol% Cr_2O_3, it seems that the reduction of chromium vaporization due to the reduced MgO in the composition was large enough to enhance the densification and to result in the final density of 96%.

In order to evaluate the influence of Cr_2O_3 on the sintering behavior of magnesia-chromite refractory composites, a comparison has been made between the densification and the grain growth behavior of *MK*1 and *MK*3. Figure 6-9 illustrates the S curve densification plot for *MK*1 and *MK*3 composites, which indicates that in both materials sintering occurred in three stages. The only difference between the densification of *MK*1 and *MK*3 is the maximum achieved density, which is higher for *MK*3 (99±0.1 %) in comparison to *MK*1 (95±0.4 %). In fact at temperatures above 1350°C, the density of *MK*3 has dominated *MK*1. This is explained by the fact that *MK*1 has more MgO than *MK*3.

As mentioned, MgO increases chromium evaporation significantly at any given condition. The sintering of Cr containing ceramics is very sensitive to the partial pressure of oxygen[82]. This sensitivity is due to the intensified chromium evaporation at high oxygen partial pressures. It is concluded that the higher density of *MK*3 in comparison to *MK*1 is due to the enhanced chromium evaporation in *MK*1.

Figure 6-10 shows the variation of grain growth versus sintering temperature for the *MK*3 and *MK*6 composites. The increase in the sintering temperature increased the grain size for both

composites, and also the grain size of *MK*3 is larger than that of *MK*1 at temperatures above 1500°C. As explained earlier, the vaporization of chromium from *MK*6 composite is perhaps higher than from *MK*3, and for this reason a larger grain size was expected for *MK*1. Other influential parameters on the grain growth of composites were first identified and used to explain this behavior. In the case of Fe_2O_3, the classic theory of grain growth[4] is not applicable due to the variety of solutes in the composition. For this reason, it is considered that the grain growth is controlled by the Ostwald mechanism in both *MK*1 and *MK*3 composites[131].

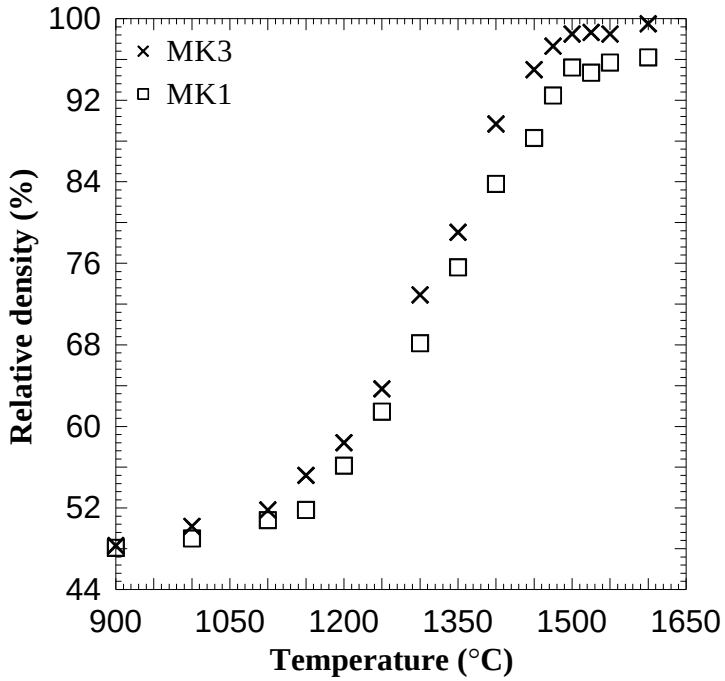

Figure 6-9. The non-isothermal densification of *MK*3 and *MK*1 composite sintered in air at different temperatures for 300 minutes; error bars are smaller than symbols

The smaller grain size of the *MK*3 composites is due to the higher Cr_2O_3 content in its composition. In fact, according to the phase diagram[2], Cr_2O_3 is less diffusive in MgO grains; therefore, in any given condition the grain growth for *MK*3 is always lower than for *MK*1. In other words, the spinel in *MK*3 is rich in Cr_2O_3 and its solubility in MgO is less than in *MK*1. As a result, the grain growth via the Ostwald mechanism is suppressed in *MK*3.

In contrast, *MK*1 contains 4.9 mol% Cr_2O_3; hence, it has higher Fe/Cr+Al ratio. For this reason, the spinel solid solution in the microstructure of *MK*1 is more soluble in MgO than the spinel in *MK*3. In addition, the MgO content of *MK*3 is less than that of *MK*1. As explained earlier this would reduce the chromium vaporization rate in *MK*3 in comparison to *MK*1. This reason also explains the smaller grain size of *MK*3 in comparison to *MK*1 composite.

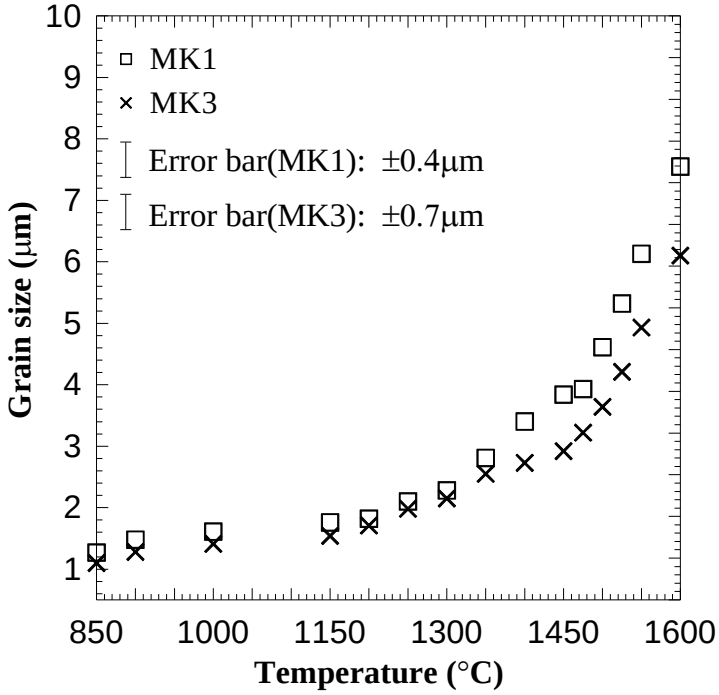

Figure 6-10. Average grain size of *MK*3 and *MK*1 composites sintered in air at different temperatures for 300 minutes

6.1.3 The effect of Al_2O_3 on the densification and grain growth of *MK* composites

The density variation with the Al_2O_3 content in the magnesia-chromite composites is plotted in Figure 6-11. The density of magnesia-chromite composites rose sharply from 81% to 96% of theoretical density with the increase in Al_2O_3 content and reached a plateau at ~6.9 mol% Al_2O_3. In order to explain this curve two subjects should be considered.

First, like in the previous section 6.1.1 discussing the effect of Al_2O_3 on the densification of both magnesia-chromite microstructure features, the effects of spinel and MgO must be evaluated. Second, in these compositions Al_2O_3 has been replaced with MgO; therefore, any changes in the densification behavior were attributed only to Al_2O_3 content. In the first part of the curve, where Al_2O_3 increases to 6.9 mol%, the increase in density can be explained by the formation of excess solid solution in compositions with the higher Al_2O_3 content.

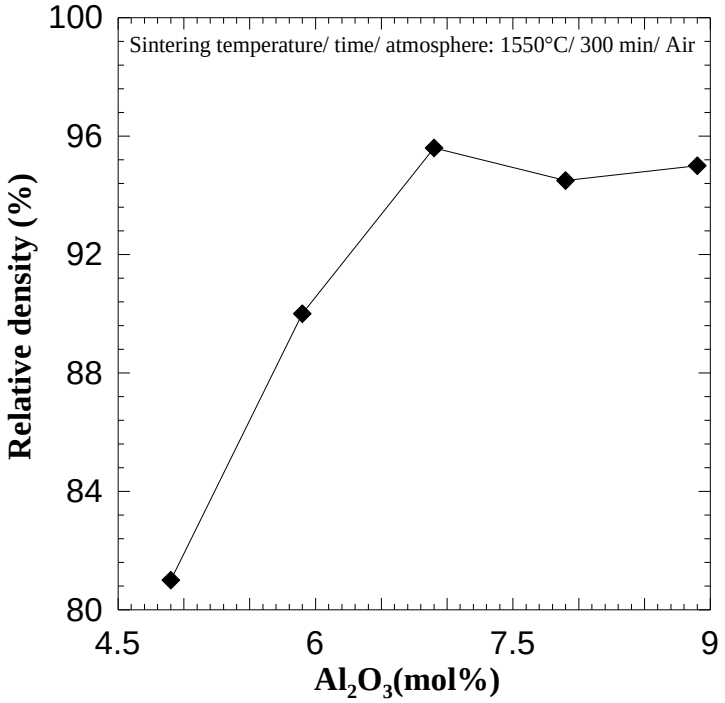

Figure 6-11. Variation of density of magnesia-chromite refractory composites as a function of Al_2O_3 content; error bars are smaller than symbols

As shown in section 5.2, Al_2O_3 enhances the densification of pure $MgCr_2O_4$, as it forms an inverse spinel solid solution with it[47]. The same analogy can be considered here. For the second part of the curve, where the density reached a plateau, two reasons could be considered. First adding more Al_2O_3 to the composite reduces the Cr/Al+Fe ratio, and secondly it also reduces the Fe/Cr+Al ratio.

The low Cr content promotes densification through the mechanism explained in the previous section, but as discussed earlier, reduction in the Fe content deteriorates the density. In fact, Fe is the only cation in this series of composites that significantly enhances the densification of both MgO and spinel in magnesia-chromite refractory composites; therefore, the addition of Al_2O_3 contributes in two opposite ways to the densification of the magnesia-chromite refractory composites. On the one hand it enhanced the density, as it reduces the total Cr content. On the other hand, it reduces the densification, as it reduces the total Fe content and enhances the vaporization of Cr from the system. In the concentration range used in this study, $4.9 \leq Al_2O_3 \leq 8.9$, for composites with Al_2O_3 concentration above 6.9 mol%, these two effects must have balanced off each other, and for this reason the density-concentration curve reached a plateau. In order to analyze the effect of Al_2O_3 on the densification and grain size of magnesia-chromite refractory composites, the densification curves of *MK*6 and *MK*3 were compared. In Figure 6-12, both composites show a trend of increasing density with temperature.

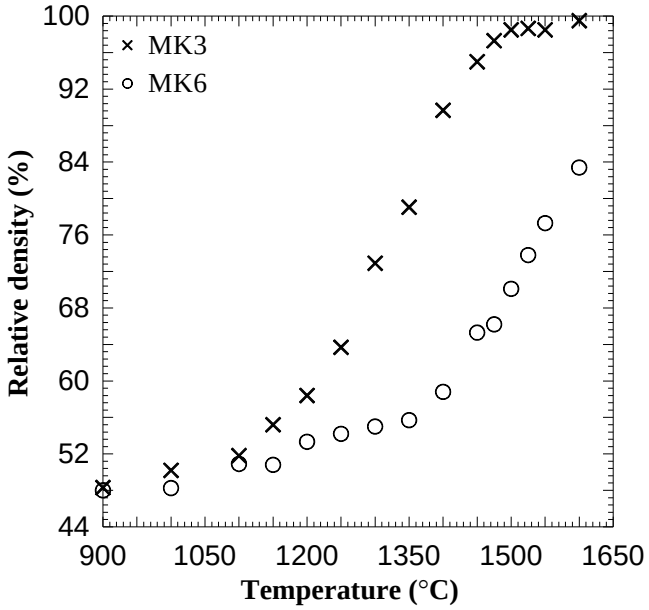

Figure 6-12. The non-isothermal densification of *MK*3 and *MK*6 composites sintered in air at different temperatures for 300 minutes; error bars are smaller than symbols

For *MK*3 the density increases slowly with the sintering temperature until 1150°C, then it rises sharply from ~55% to 96% with a ~250°C increase in sintering temperature, and reaches a plateau of 96-99% for sintering temperatures above 1450°C. In contrast, density of *MK*6 increases linearly with a relatively small slope up to ~1350 C, then with a sharper slope up to ~1600°C, when density reaches ~86 %.

The change in the grain size of *MK*3 and *MK*6 composites at different temperatures is shown in Figure 6-13. There is the same pattern for both composites; however, the grain size of *MK*6 is slightly larger than that of *MK*3. This is explained by the higher ratio of Cr/Fe+Al in *MK*6 in comparison to *MK*3.

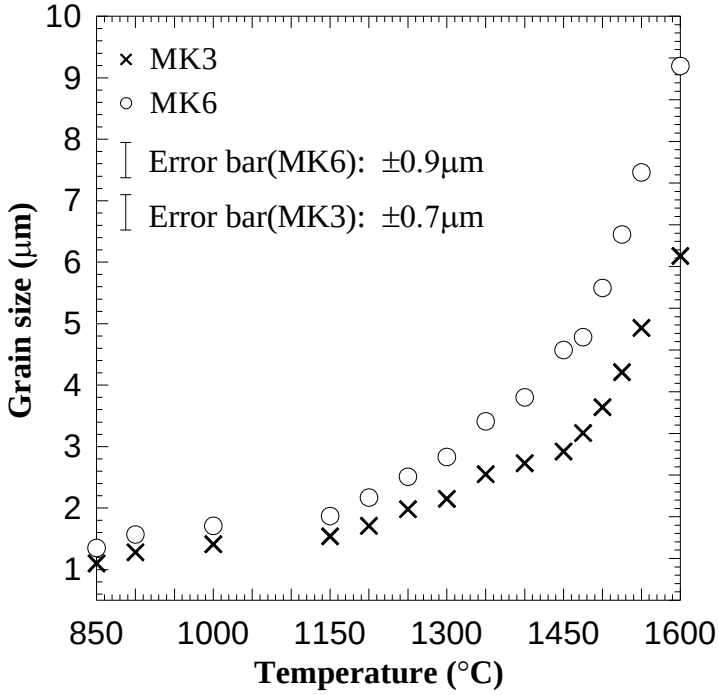

Figure 6-13. Average grain size of *MK*3 and *MK*6 composites sintered in air at different temperatures for 300 minutes

As any change in alumina content in these samples has been balanced with MgO, the low alumina content in *MK*6 means that there is more magnesia in this composition in comparison to

*MK*3. The higher MgO content increases the vaporization of chromium from the composite, as it increases the Cr^{+3}/Cr^{+2} ratio[132]. The larger grain size of *MK*6 is attributed to the evaporation/condensation mass transport mechanism, which is possibly more active in *MK*6 than in *MK*3.

6.1.4 The effect of Fe_2O_3, Cr_2O_3, and Al_2O_3 on the microstructures of sintered magnesia-chromite refractory composites

In the previous section the influence of chromite constituents on the sintering of synthetic chromite were investigated. It was shown that each of the three considered oxides can change the densification and the grain growth behavior in a certain way. This makes the studying of the sintering mechanism of magnesia chromite composite challenging. In this section we will study the effect of each oxide on the final microstructure of the magnesia chromite composite with respect to the morphology of the grains. Moreover, the influence of the oxide on the dihedral angle, as well as the grain boundary energy of the magnesia chromite composite are reported, in order to verify the results of densification of magnesia chromite composite provided in the previous section.

The microstructures of *MK*1 and *MK*3 composites quenched from 1550°C after 300 minutes sintering are shown in Figure 6-14. In the *MK*3 composite, which is enriched in Fe_2O_3, the spinel grains are mostly equiaxial. In contrast, the spinel grains in the microstructure of *MK*12 with high alumina and chromia are generally angular. This difference in the morphology of these spinels can be explained with respect to the strain energies due to the lattice mismatch between MgO and spinel solid solution[94].

The phase composition of the spinel in *MK*3 and *MK*12 is calculated theoretically, assuming that all trivalent oxides react with an equal mole percent of magnesia to form spinel.

The results are reported in Table 6-3. *MK*12 contains only 6 wt% $MgFe_2O_4$. Contrary to *MK*12, *MK*3 consists of 19 wt% $MgFe_2O_4$. Since the interface between MgO and $MgFe_2O_4$ is reported to be coherent, then the formed spinels in *MK*3 are more rounded[134].

The interface between $MgAl_2O_4$ and $MgCr_2O_4$ is not coherent and makes the spinel more irregular and angular[134]. Goto and Lee[134] reported that in the microstructure of magnesia chromite refractories the chromite precipitates with different morphologies on the magnesia grains. They attributed this phenomenon to the contribution of the strain energy to the microstructure of chromite refractories.

Table 6-3. The theoretical composition of spinel solid solution in magnesia-chromite refractory composites

	$MgFe_2O_4$ (wt%)	**$MgAl_2O_4$ (wt%)**	**$MgCr_2O_4$ (wt%)**
MK3	19	40	52
***MK*12**	9	36	45

The dihedral angle of the 12 designed composites has been calculated from the *SEM* images. The dihedral angle was selected as the angle with the maximum frequency of repetition. Since the designed composites consist of two phases, three different dihedral angles have been defined: MgO/MgO ($\varphi_{M/M}$), spinel/spinel ($\varphi_{S/S}$), and spinel/MgO ($\varphi_{S/M}$). In this study, the dihedral angle between spinel and MgO was considered for the analysis of the effect of dihedral angle on the densification of the composites.

The reason was that the $\varphi_{M/M}$ and $\varphi_{S/S}$ varied very little with the composition. The average calculated $\varphi_{M/M}$ and $\varphi_{S/S}$ values were almost the same, ~114 and 109° respectively. Theoretically, the value of $\varphi_{M/M}$ and $\varphi_{S/S}$ for a single crystal MgO and spinel should have been 120°[4]; however, these composites consist of two polycrystalline phases, with different orientations of the grains,

as well as variation of composition along the grain boundaries. As a result, the calculated values are acceptable. Figure 6-16 shows the frequency of repetition of dihedral angles for the *MK*3 composite. According to the above definition, the dihedral angle for this composition is 96°.

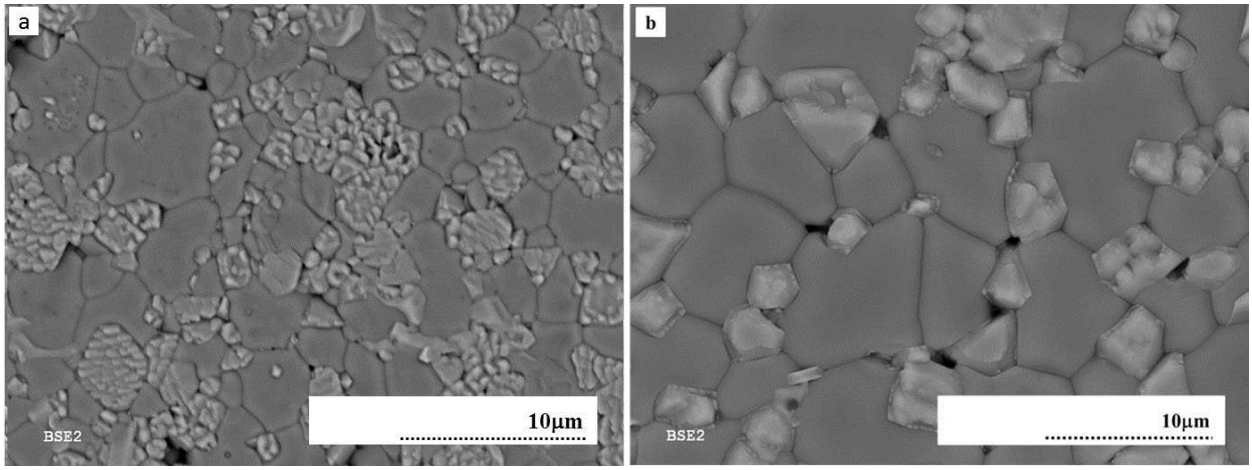

Figure 6-14. BSE images of a) *MK*3 and b) *MK*12 composites sintered at 1550°C for 300 minutes

The change in the dihedral angle ($\varphi_{S/M}$) versus the R_2O_3 content is shown in Figure 6-16. The increase in the Al_2O_3 and Fe_2O_3 decreases the dihedral angle. In contrast, the value of $\varphi_{S/M}$ is proportional to the Cr_2O_3 content. The same trend has been reported by White et al. [2] measuring the effect of the same oxides on the dihedral angle in MgO-15 wt% monticellite. The main difference between the results of the present study and the one reported by White is the measure of dihedral angle. The values reported by White are considerably lower than those calculated in the present study.

For instance, ($\varphi_{M/M}$) was reported to increase from 25 to 45° for MgO-15 wt% monticellite with a 10mol% increase in the Cr_2O_3 content. Also, ($\varphi_{M/M}$) was reported to decrease from 25 to 20° with a 10mol% increase in the Fe_2O_3 content.

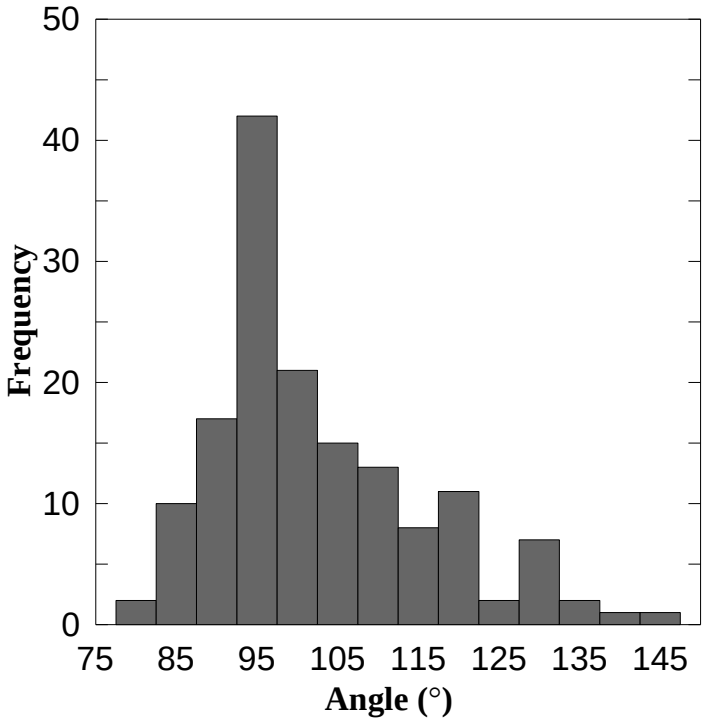

Figure 6-15. The calculation of dihedral angle for the *MK*3 composite

This difference can be explained by considering the fact that White measured the dihedral angle between magnesia grains in a matrix of melted monticellite. The interfacial energy ($\gamma_{solid/solid}$) is usually 1 to 2 orders of magnitude lower than ($\gamma_{solid/liquid}$)[4], thus the dihedral angle decreases according to the equation 6-2. In contrast, in the present study the dihedral angle was measured in the solid state. The grain boundary energy of the oxides and spinels has similar values, 1-2 J.m^{-2}; therefore, the dihedral angle is relatively high. The increase and decrease in the dihedral angle can be translated to increase and decrease in the interfacial energy between the MgO/spinel grains according to the following equation:

$$cos(\varphi_{S/M}/2) = \frac{\gamma_{M/M}}{\gamma_{S/M}} \qquad 6\text{-}2$$

where $\gamma_{M/M}$ and $\gamma_{S/M}$ are the grain boundary energy of MgO/MgO and the interfacial energy between MgO and spinel grains respectively. The grain boundary energy of the *MK*3 composite

was calculated using the above equation; the grain boundary energy of pure MgO ($\gamma_{M/M}$ = 1.411 $J.m^{-2}$) was obtained from literature[135]. Using the average dihedral angle between MgO and spinel $\varphi_{S/M}$ = 95 in the equation 6-2, the resulted interfacial energy was about 1.04 $J.m^{-2}$ for *MK*3 with 2.71 mol% Fe_2O_3 sintered at 1550°C. The $\gamma_{S/M}$ decreased to 0.965 $J.m^{-2}$ with the increase in the Fe_2O_3 content of the composite to 4.9 mol%.

This reduction in the interfacial energy can be correlated to the higher solubility of Fe_2O_3 in both magnesia and spinel solid solution, which enhanced the densification and reduced the strain energy between spinel and MgO. It also resulted in the formation of a rounded second phase between the MgO grains in the microstructure of high iron oxide content magnesia-chromite refractory composites. The uncertainty of these measurements is estimated at ±5°.

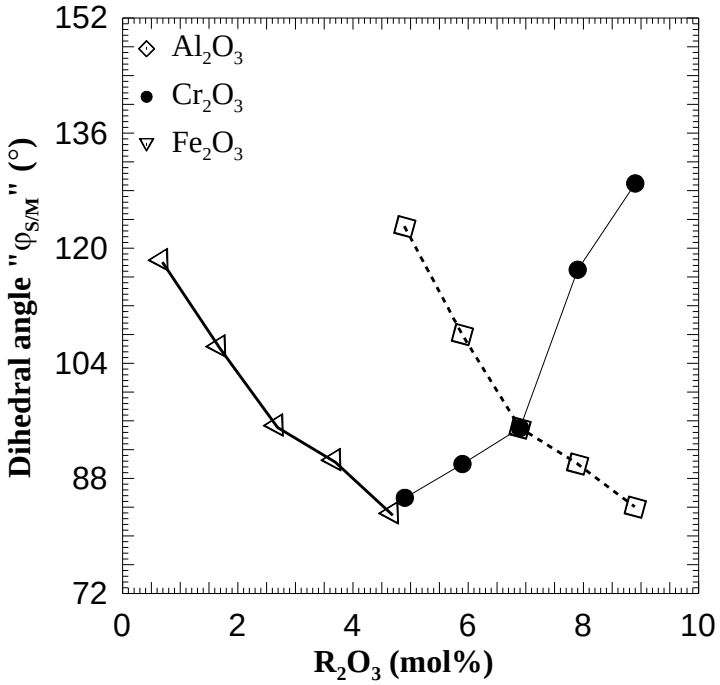

Figure 6-16. The variation of the average dihedral angle of magnesia-chromite refractory composites versus oxide content; the composites were sintered at 1550°C for 300 minutes

The change in the relative density of the magnesia-chromite refractory composites with the dihedral angle is shown in Figure 6-17: the relative density is higher for the composition with the smaller dihedral angle. Similar results have been reported by Alper[2], who reviewed a study by White et al. and showed that Fe_2O_3, Al_2O_3, and TiO_2 improved the densification of the basic refractories by decreasing the dihedral angle between the magnesia grains.

Gosh et al.[13] also reported that the addition of ZrO_2 to the magnesia chromite refractories increased the densification due to the decrease in the dihedral angle. To the best of our knowledge, there is however no published information about the effect of Fe_2O_3, Al_2O_3, and Cr_2O_3 on the dihedral angle of magnesia or chromite spinel. In this section the effect of trivalent oxides on the densification, grain growth behavior, and microstructure of magnesia-chromite composites were investigated. For this purpose, 12 compositions were prepared and compared with each other, with respect to the density and grain growth.

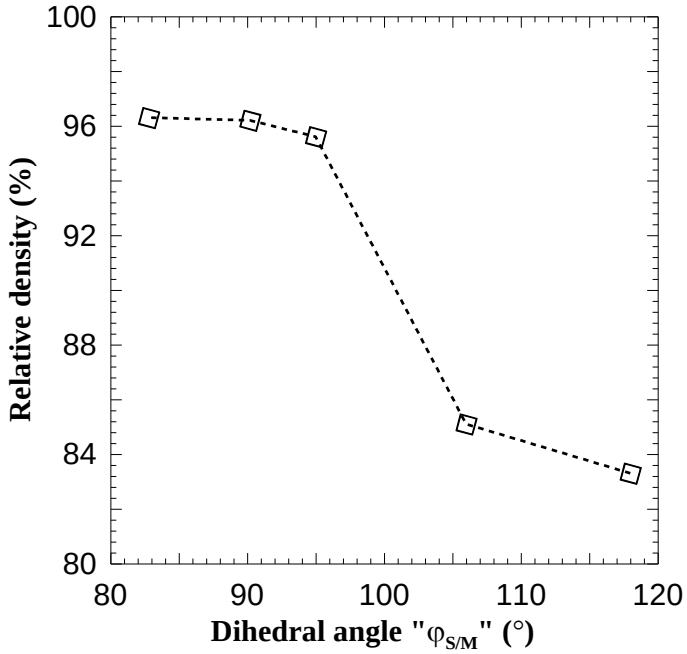

Figure 6-17. The variation of the density versus the dihedral angle for magnesia-chromite refractory composites

Based on the results, the *MK*3 composition was selected for studying the kinetics of sintering. For the sake of simplicity, the *MK*3 is called *MK* composite hereafter. In addition, nano sized *MK* called, *NMK*, was also prepared via Pechini's method (section 2.2.1.1) and was used to evaluate the effect of particle size on the densification behavior of the magnesia-chromite refractory composites.

6.2 The densification behavior of *MK* composite

Figure 6-18 shows the variation of the relative density and the grain size of the *MK* composite for sintering temperatures between 850ºC and 1600ºC. The plot of the relative density versus sintering temperature exhibits a sigmoidal shape. The density increased only 4% up to 1150°C, but increased significantly, up to 92%, at sintering temperatures between 1150 and 1450°C. The densification rate was lower for sintering temperatures above 1450°C, and the maximum density of the composite was 98% of the theoretical density at 1600°C.

The variation of grain size with the sintering temperature showed a parabolic shape. While the density was significantly increasing between 1150° and 1450°C, no considerable increase in the grain size was observed in this range of temperatures. In contrast, at temperatures above 1475°C the grain size increased dramatically, i.e. by ~140%, whereas the density increased only by ~5%. The average grain size of the *MK* composite was ~7 μm, and the standard deviation of the measured grain size was ±0.9 μm, for the fully dense (ρ~98%) composite. According to the classic theory of sintering, this curve shows the three stage of sintering[4]: the first stage, where no significant densification occurred (<4%), the intermediate stage, where the density increased dramatically from ~52% to 92%, and the final stage, where the density increased slightly from 92 to 98 % and the grain size increased significantly from ~3 to ~7μm.

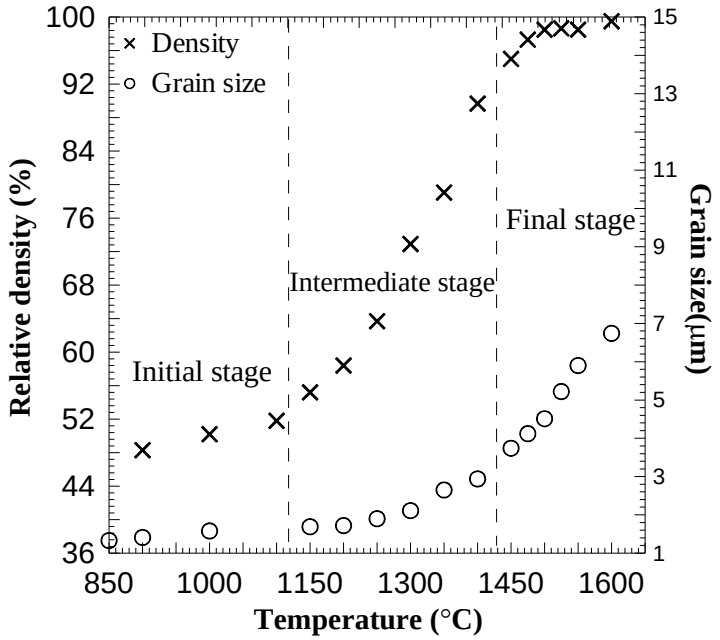

Figure 6-18. The non-isothermal densification and grain size of *MK* composite sintered in air at different temperatures for 300 minutes

The reduced densification rate in the 3rd stage can be linked to the grain growth[16] and the presence of insoluble gas entrapped in the closed pores[5]. This behavior can be attributed to the distribution of open pores in the 2nd stage of sintering and to their contribution on the grain growth inhibition. During the intermediate stage, pores are usually located at the triple junctions and would pin the grain boundaries, consequently suppressing the grain growth.

However, as the temperature increases, the pores would become thermodynamically unstable[136] and form closed ones at the beginning of the final stage. As a result, the grain size increases sharply, as there is no resistance to the grain boundary migration. This phenomenon has been addressed by several researchers. Mazaheri et al.[137] investigated the two-step sintering of nano ZnO and showed that in a certain sintering condition it was possible to densify nano ZnO to the full density with about 200% smaller grain size in comparison with the same composition

sintered in a conventional sintering profile. Li et al.[138] reported the same phenomenon by comparing the conventional sintering procedure to the two-step sintering procedure.

Another reason for the limited grain growth at the intermediate stage of the sintering of *MK* composite could be the presence of the second phase in the microstructure. In the *MK* composite, ~30 vol% of the microstructure consists of the spinel phase. The presence of spinel affects the grain growth rate during the 2nd stage of sintering, when the grain boundary migration is controlled by volume and by the grain boundary diffusion mechanisms. However, it should be mentioned that due to the solid solubility between magnesia "matrix" and spinel "inclusion", the grain boundary pinning has probably occurred due to the size factor.

According to the Zener drag effect theory[1, 4] the exerted drag force on the grain boundaries is proportional to the grain boundary surface area that is occupied by the 2nd second phase. In this regard, the fewer and the smaller the 2nd phase particles are at the grain boundaries, the more drag forces they create, and become more effective in the hindrance of the grain growth. In addition, it is known that any phenomenon which increases the movement of the 2nd phase would increase the grain growth[5]. The *MK* composite powder has been synthesized through the chemical route to ensure the uniformity of the mixing at molecular level[44,139,140]. In addition, the grain sizes of spinel (d_{SP}:1.28 μm) and magnesia (d_{Mg}:1.34 μm) are relatively identical.

Therefore, the slight increase in the grain size of the *MK* composite is attributed to the increased mobility of MgO grain boundaries at high temperature, due to the solid solubility between MgO and spinel. Moreover, the increase in temperature also increased the spinel grain size and reduced its effect on the grain boundary movement. At temperatures above 1450°C, the pores were collapsing and the inclusions were large enough to not be able to inhibit the grain growth, allowing for a ~140% grain size increase. The influence of inclusions on the density of

ceramics has been studied for several systems. Haroun[141] theoretically and experimentally proved the inclusions would suppress the grain growth during the densification of ceramics. He also showed that the grain growth inhibition depends on the size and the movability of the inclusion. Lange et al.[142] studied the Al_2O_3-ZrO_2 system and reported that although ZrO_2 hindered the grain growth of Al_2O_3, it became more effective when its concentration was ~5 vol%.

The typical microstructure of the *MK* composite at the different stages of sintering is shown in Figure 6-19a-d. The microstructure of the specimen sintered at 1150°C (Figure 6-19a) contains a large amount of pores, which reflects the low density of the composite (ρ=54%). Increasing the sintering temperature to 1350°C (Figure 6-19b) resulted in the reduction of the pore content and the formation of a relatively dense structure with ~80% density. The sintering at 1475°C (Figure 6-19c) provided a near fully dense microstructure ~96%, with larger grains of 6.4 to 7.3 μm; however, a further increase in the sintering temperature (T=1600°C, Figure 6-19d) only increased the grain size from ~4 μm to ~7 μm, at 98 % relative density.

Figure 6-19 also shows that the spinel phase is composed of smaller equiaxial sub-grains. This microstructure can be explained by the fact that the composites used in this study were made via a chemical method, which is homogeneous at the molecular level. In Section 5.2 it was shown that spinels such as $MgAl_2O_4$, $MgCr_2O_4$, and $MgFe_2O_4$ would form in such homogenous mixtures at relatively low temperatures (T<1000°C). It was also shown that the formation mechanism involves the oxidation of nitrates to oxides, followed by the spinel-forming reaction between the oxides. Therefore, the microstructure of the *MK* composite at the calcination temperatures and also at low sintering temperatures (T<1350°C) is composed of MgO and

spinels or spinel solid solutions. Figure 6-19a,b illustrate this microstructure, consisting of small cubic and equiaxial grains with rounded edges, randomly distributed in the microstructure.

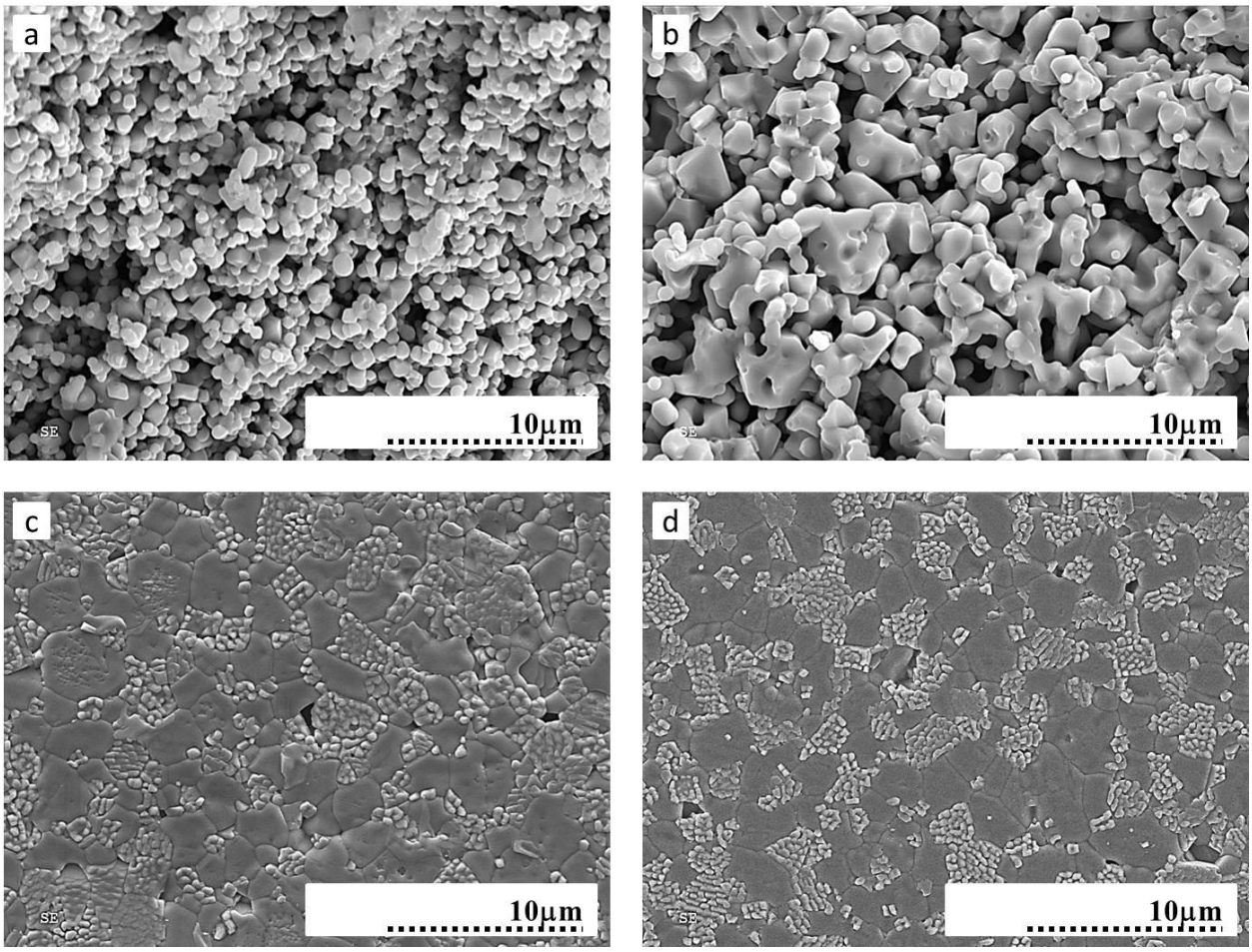

Figure 6-19. The microstructure of *MK* composite at a)1150°C, b)1350°C, c)1475°C, and d)1600°C

As determined by *EDX*, the cubes are rich in magnesia and the equiaxial grains are rich in spinel forming oxides. At high sintering temperatures (T >1400°C) there is unlimited solid solubility between spinel structures ($MgCr_2O_4$- $MgFe_2O_4$- $MgAl_2O_4$); as a result, they form a solid solution with a composition close to $(Mg_{1-x-y},Fe_y,Al_x)[Cr_{2-x-y},Al_x,Fe_y,Mg_{x+y}]O_4$.

In contrast, there is a limited solid solubility between the spinel solid solution $(Mg_{1-x-y},Fe_y,Al_x)[Cr_{2-x-y},Al_x,Fe_y,Mg_{x+y}]O_4$ and magnesia. Therefore, at the sintering temperature,

when the concentration of spinels gets beyond the solid solubility limit in magnesia, the spinel solid solution exsolves from magnesia grains and changes the microstructure of the *MK* composite to the one shown in Figure 6-19c and d. A very similar microstructure was also observed in the sintered microstructure of $BaTiO_3$-$SrTiO_3$ solid solutions[143].

Figure 6-20 also shows the *SEM* image of the *MK* composite sintered at 1600°C in the regions where the exaggerated grain growth has occurred. The exaggerated grain growth can be attributed to the inhomogeneous distribution of the pores and to the second phase in the *MK* microstructure. This was caused by the reduced pore volume at high temperatures, and also by the high solid solubility of MgO and spinel, which resulted in the ongoing local composition change. As a result, the grains at the dense locations grew faster than in the rest of the *MK* microstructure. The same phenomenon has been reported by Lange et al.[142] in the studying of the effect of ZrO_2 on the densification of Al_2O_3. Roy[14, 85] also reported the effect of the solute on the densification and the grain growth of Cr_2O_3.

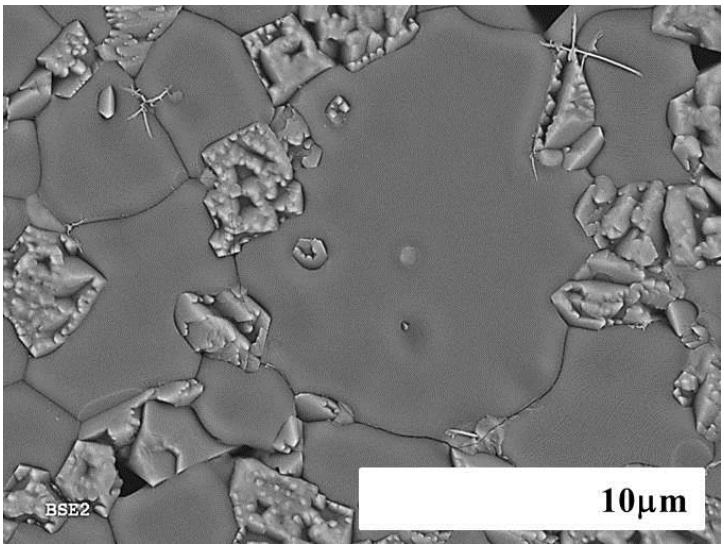

Figure 6-20. The *SEM* image of *MK* composite at 1600°C showing the exaggerated grain growth

The isothermal experiments were performed at 1200°C-1600°C with 50°C intervals. The evolution of the relative density over the sintering schedule at different holding temperatures is shown in Figure 6-21. This set of experiments has been executed to understand the densification behavior of the *MK* composite at the different stages of sintering.

As expected based on the theory of densification[4], the density did not change at temperatures below 1150°C, in the initial stage of sintering. The densification rate was increasing in the temperature range of 1200-1450°C. At temperatures above 1450°C the densification rate was increasing at holding times below 70 minutes, but it was almost zero beyond that time limit. In other words, at temperatures above 1475°C no change in the density was recorded after 70 minutes, indicating that this was the optimum sintering time for the *MK* composite.

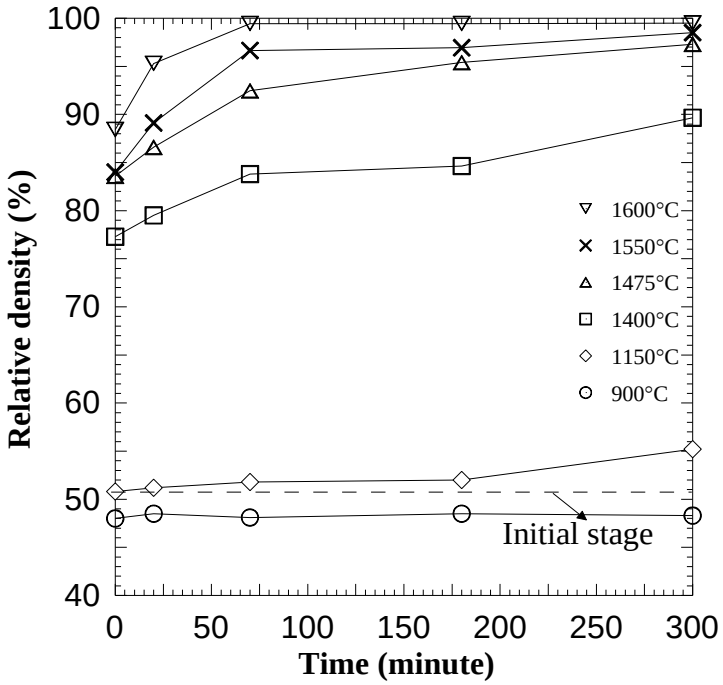

Figure 6-21. Isothermal densification of *MK* composite sintered in air at different temperatures

Figure 6-22 illustrates the variation of the grain size with the relative density of the *MK* composite. The grain size did not change considerably until the density reached the critical value of ~60% of the theoretical density, which indicates the initial stage of sintering. Above this critical density, the grain size increased slightly until the density reaches ~90%, and it rose dramatically to the maximum average grain size value. The 90% is the critical density above which the grain growth accelerates, indicating the transition from the intermediate to the final stage of sintering. Correlating the densification and the grain size results with the microstructures of the sintered composite supports the division of the sintering process of *MK* composite into the three stages.

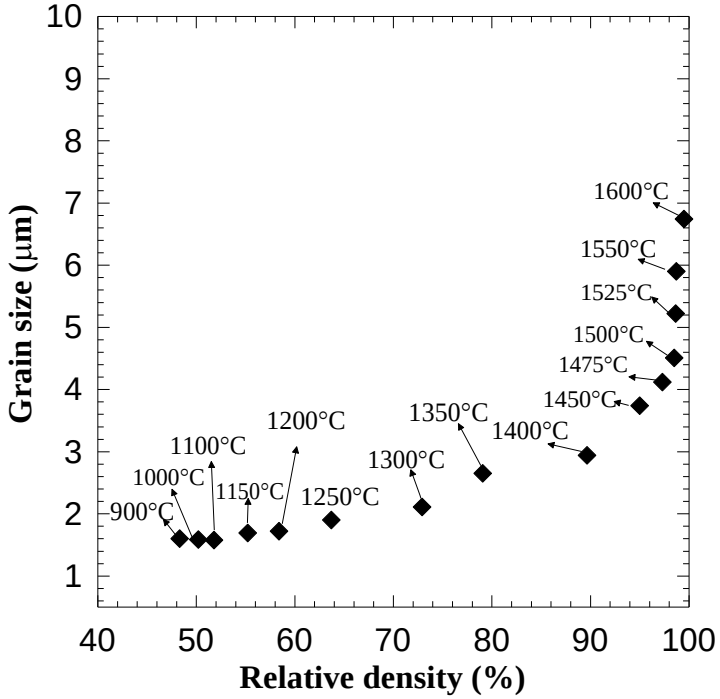

Figure 6-22. The isothermal grain size versus relative density of *MK* composite sintered in air at different temperatures for 300 minutes

In the initial stage, the neck formation, with no densification and no grain growth occurred; this stage was followed by the intermediate stage, when the grain growth happened above the

critical relative density due to the collapse of some pores, in spite of the presence of the 2nd phase and a continuous network of pores.

The main characteristic of the final stage of sintering was the rapid grain growth. During the final stage, the densification did not change considerably, although the grain size did change; however, only closed pores and the secondary phase remained in the final sintered microstructure.

As mentioned in the literature, one parameter which could affect the densification behavior is the initial particle size of the ceramic powder. According to Herring's scaling law[144], the particle size is proportional to the reciprocal sintering rate; the smaller particles sinter faster than the larger ones.

Reducing the particle size increases the surface area of the system and substantially increases the driving force for the sintering process, which could result in a considerable reduction in the sintering[145-148]. In spite of this achievement, reducing the particle size also increases the chance of agglomeration, contamination and grain coarsening, which negatively affects the physical and the mechanical properties of a certain ceramic[149-151].

Since one of the main objective of this study was to reduce the sintering temperature of the magnesia-chromite composites in air from 1750°C to below l500°C, nano particles of the *MK* composite were prepared via Pechini's method, as described in the experimental section 4.1.2. The sintering studies were performed on the pellets made of the nano *MK* composite particles (called *NMK*), and the results were compared to those obtained by the micron sized *MK* composite.

Figure 6-23 shows the densification and the grain growth change of the *NMK* composite at sintering temperatures in the 900-1600°C range; the plot of the density exhibited a sigmoidal

behavior, implying the occurrence of the three stages of sintering. The density increased slowly from ~35% to 44% at 1000°C, dramatically increased from 44 to ~92% at 1300°C, and reached a plateau at almost 1350°C. The three stages of sintering are inserted in Figure 6-23.

The grain size followed a parabolic profile, rising sharply from ~700 nm at 1300°C to ~2000 nm at 1475°C. The microstructures of specimens, marked as A, B, C, and D on Figure 6-23, are shown in Figure 6-24. As expected, the pore volume decreased from ~30% at 1100°C to zero at 1350°C. However, the grain size increased dramatically to 100 times the grain size of the primary "synthesized grains", and to 10 times the grain size of the specimen sintered at 1150°C+-.

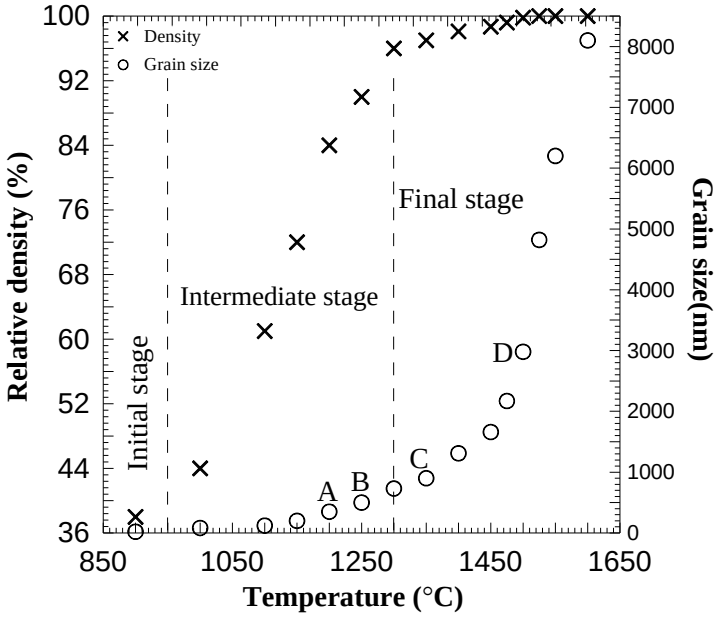

Figure 6-23. The non-isothermal densification and grain size of *NMK* composite sintered in air for 300 minutes

Three mechanisms could be attributed to the high grain growth in the microstructure of *NMK* composite. It is well known that the reduction in the particle size increases the surface area of a system, and the surface related phenomenon will be affected by the increased surface area.

In the case of the *NMK* composite, the high surface area has probably increased the evaporation of Cr_2O_3 from the system at the sintering temperature, and enhanced the non-densifying evaporation/condensation mass transport mechanisms, resulting in the grain growth. The evaporation of Cr_2O_3 is known to be detrimental for the densification of Cr_2O_3 containing ceramics[11,88]. We have also showed that the spinel forming additives such as Al_2O_3 and Fe_2O_3 would not affect the evaporation rate of Cr_2O_3 in the designed magnesia-chromite composite. Considering the above explanations plus the fact that the sintering was carried out in air, the very high surface area of the nano sized *NMK* composite could be attributed to the high grain growth rates, especially at temperatures above 1350°C. This statement is verified by the fact that the oxidation and evaporation of Cr_2O_3 exponentially increased with the temperature, as reported by Graham[84].

The second reason of the high grain growth rate is also related to the small size of the powder in *NMK*. The grain growth might have occurred through the Ostwald mechanism, like for the *MK* composite. The smaller particle size of the *NMK* grains created the short diffusion paths and resulted in the high dissolution of small grains and the growth of large grains. According to the Fick's second law, the penetration depth (x_d) is relative to the square root of the product of the diffusion coefficient (D_d) and time (t), ($x_d=2\sqrt{D_d}.t)^1$. In the *NMK* composite the penetration depth is very short, 20 nm; therefore, the time required for the diffusion of cations from one grain to another is short, and the grain growth rate is high. The extensive grain growth of nano ceramics has been studied by several investigators[99, 146, 149, 152-156].

They all showed that grain growth occurred as a result of the grain boundary mobility and the full densification occurred when the grain boundary mobility was suppressed. The grain boundaries are also known as sinks for vacancies; therefore, the separation of the grain boundary

from pores is detrimental to the densification[146,156]. Several techniques have been used to sinter the nano ceramics with limited or no grain growth, but the review of these techniques is not in the scope of this study.

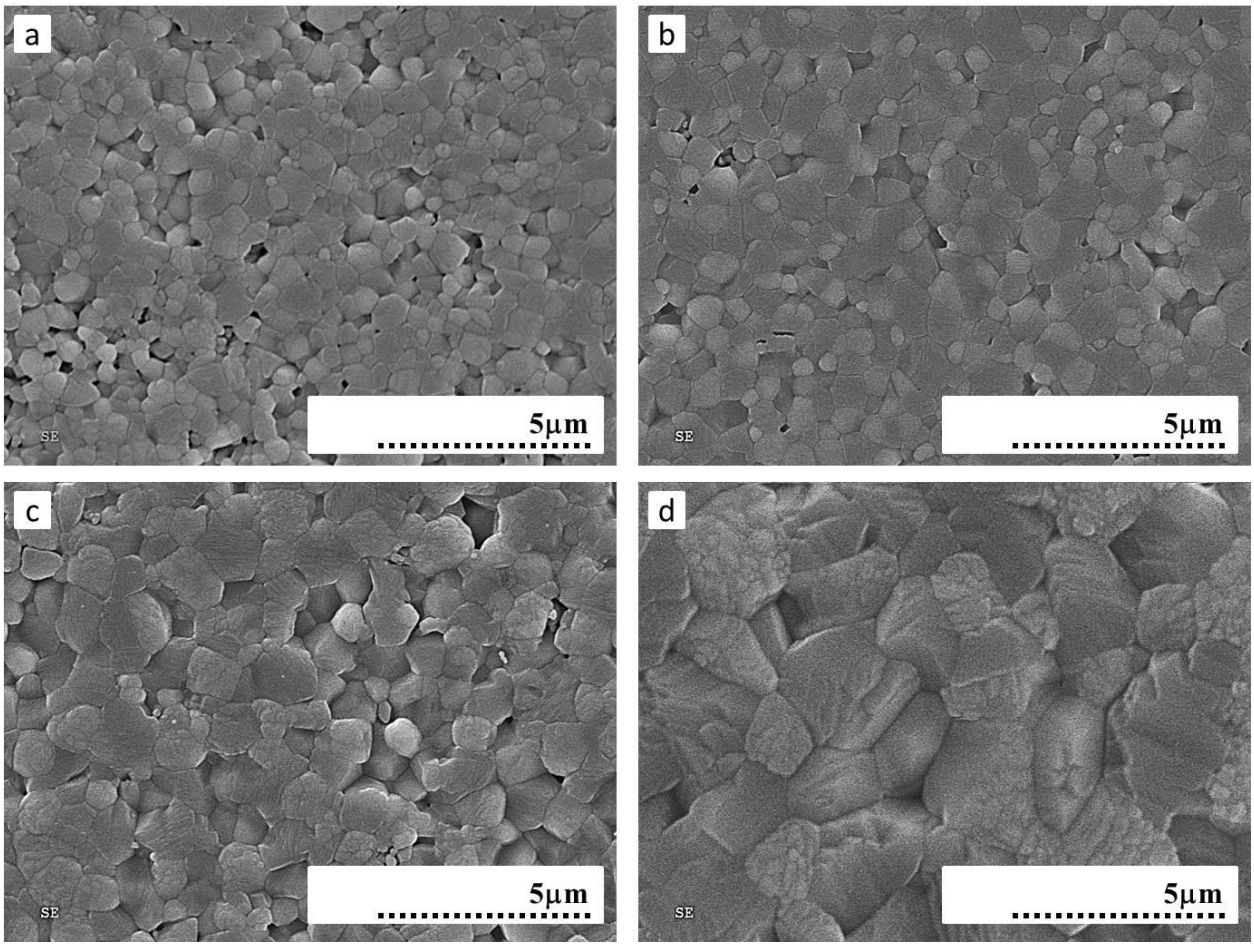

Figure 6-24. The microstructure of *NMK* composite at a)1150°C, b)1250°C, c)1350°C, and d)1475°C

The isothermal densification behavior of the *NMK* composite is shown in Figure 6-25. It is similar to the one presented for the *MK* composite in Figure 6-21. At high sintering temperatures, above 1350°C, the variation of density with the sintering time reaches a plateau relatively fast, i.e. after about 20 minutes.

In the mid sintering temperature range from 1100°C to 1300°C, the density increases continuously. There are some similarities between the isothermal densification behavior of *NMK* and *MK* at the low sintering temperatures, where the density was below 60%; however, the density increased linearly with time for *NMK*, while it did not change significantly in the *MK* composite. This different behavior can be explained by the different sintering kinetics for the nano and micro sized *MK* grains.

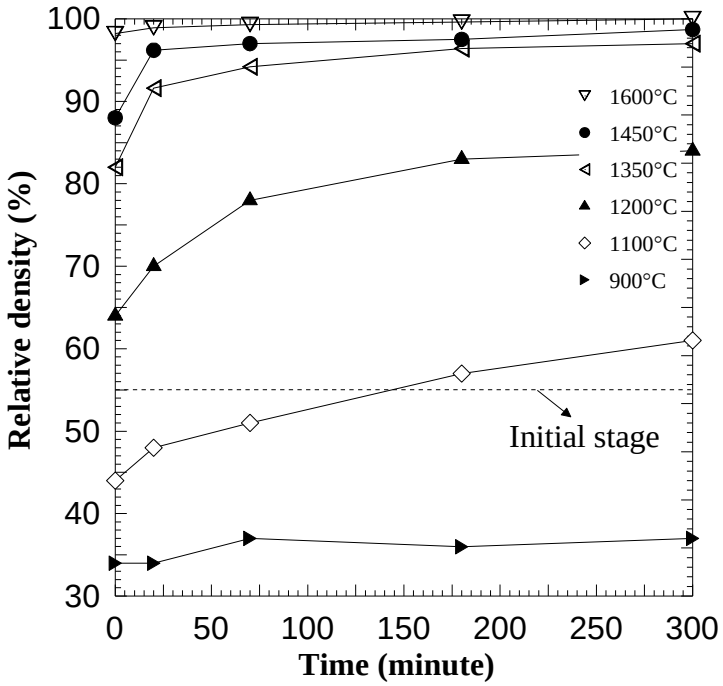

Figure 6-25. The isothermal densification of *NMK* composite sintered in air at different temperatures

A comparison has been made between the densification behavior of *MK* and *NMK* composite in Figure 6-26. It is observed that the onset sintering temperature of the nano sized particles is ~200°C below the onset sintering temperature of micron sized *MK* grains. In the intermediate stage, the sintering process of *NMK* composite also continued faster than that of the *MK* composite; however, they both reached their full density.

This is attributed to the fact that at higher sintering temperatures, the difference between the densities of specimens with low green densities decreases, and results in the convergence of densification curves of both set of samples to the same value. Despite the fact that the green density of specimens made of *NMK* grains was lower, they reached the full density even faster than the *MK* grains. As mentioned in the beginning of this chapter, the same phenomenon has been observed by Neves[100].

The driving force of sintering is the reduction of the interfacial energy[4]. This is caused by the reduction in the interfacial energy and in the surface area, through the decrease in the densification and grain growth respectively. By reducing the particle size to the nano range, the surface energy of the system and the sintering driving forces are higher than for the micro size grains.

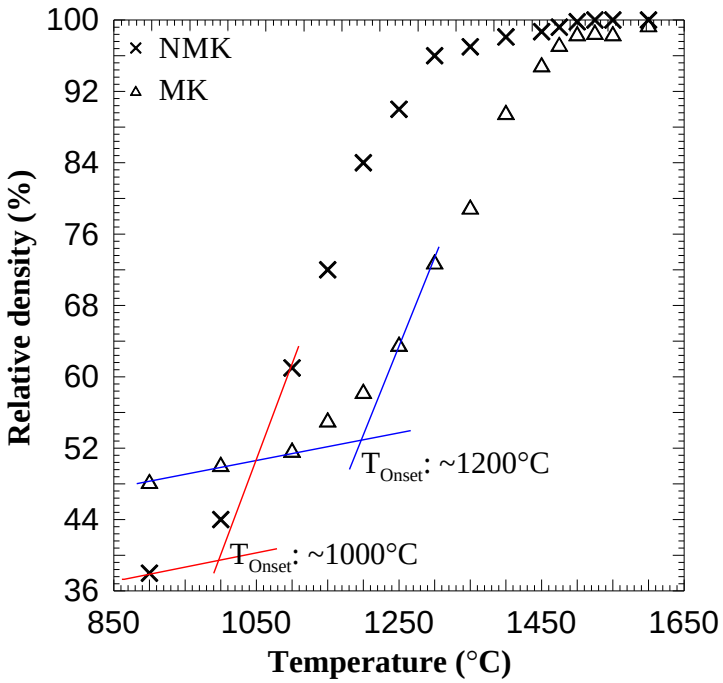

Figure 6-26. The comparison between non-isothermal densification behavior of *MK* and *NMK* composite sintered in air for 300 minutes

Moreover, due to the higher ratio of grain boundary in the nano composite in comparison to micron sized composites, higher grain boundary diffusion was expected between the nano grains. Both the densification and the grain growth occur by the diffusion process; therefore, a higher densification in the first two stages of sintering was expected for the *NMK* than for the *MK* composite. For the same reasons, a higher grain growth was also expected for *NMK* than for the *MK* composite during the final stages of sintering, where the grain growth mechanisms were active. The same phenomenon has been reported by Neves[100], who compared the densification behavior of nano and micron size zinc oxide. He showed the densification rate and the grain growth rates of nano sized zinc oxide powder were both higher than the ones reported for the micron sized powder. Pietrzak et al.[157] also reported that using nano alumina instead of micro alumina enhanced the densification of alumina – Cr composites. They also attributed the results to the high surface area of the specimens prepared using nano alumina.

The results described above show that both *MK* and *NMK* composite experienced the three stages during the sintering schedule. However, despite the similarities in the sintering behavior of *MK* and *NMK* composites, the results show that reducing the particle size from ~1.2 μm to 20 nm substantially enhanced the densification. The main drawback of reducing the particle size (neglecting the increased processing costs) was the increased grain growth. The grain size increased ~4 times from ~1.5 μm to 7 μm by sintering the *MK* composite at 1600°C; in contrast, the grain grew~400 times for the *NMK* composite, during the same sintering schedule.

It should be noted that in spite of the higher rate of the grain growth of the *NMK* composite, the final grain sizes were identical for both composites. It was also shown that there was a difference between the initial stage of sintering of *MK* and *NMK*. No significant density change was observed during the sintering of the *MK* composite, while the density increased

linearly during this stage for the *NMK*. In order to determine the mechanisms involved in the sintering and the reason for the difference in the sintering of *MK* and *NMK* composites, their sintering kinetics were compared.

6.3 Kinetics of sintering of *MK* and *NMK* composites

The main objective of this section is to determine the sintering mechanisms through studying the kinetics of sintering of the *MK* and *NMK* composites. The sintering practices in this study were performed isothermally, however owing to the high number of experiment runs, we were able to demonstrate the results in a non-isothermal pattern as well. For this reason, the classic sintering model for the two spheres developed by Kingery and Berg[5] was applied to the densification results to analyze and to estimate the sintering mechanism. According to this model, the kinetics of the initial stage sintering can be expressed by the following equation:

$$\frac{\Delta\rho}{\rho} = 3\left[\frac{H}{G^m}t\right]^n \qquad 6\text{-}3$$

where $\Delta\rho/\rho$ is the relative densification, H is a function of temperature and geometry, G is the grain size, t is the sintering time, m is a Herring scaling law exponent, and n is a parameter which depends on the sintering mechanism (Table 6-4). The variation of $\ln(\Delta\rho/\rho)$ with ln(t) was plotted for different sintering temperatures resembling the initial stage of sintering. According to the following equation 5-12, the slope of this curve is the sintering exponent n, by which the sintering mechanism can be estimated. Table 6-4 illustrates the correlation between the sintering mechanisms and the n values.

$$ln\left[\frac{\Delta\rho}{\rho}\right] = nln(t) + constant \qquad 6\text{-}4$$

Figure 6-27 shows the variation of ln($\Delta\rho/\rho$) versus ln(t) for the *MK* composites sintered isothermally at 1000°C, 1100°C, and 1150°C. The sintering temperatures were selected based on the densification results presented in Figure 6-18. It was shown that the sintering procedure for the *MK* composites can be divided into 3 sintering stages, i. e. the initial stage "950-1150°C", the intermediate stage "1200-1450°C", and the final stage "1475-1600°C".

Table 6-4. Exponent values reported for different sintering mechanisms[4, 5]

Mechanism	*n*	*m*
Surface diffusion	0.286	4
Grain boundary diffusion	0.334	4
Lattice diffusion from surface	0.5	3
Lattice diffusion from grain boundary	0.4	3
Vapor transport	0.667	2
Viscous flow	1	1

As shown in Figure 6-27, the sintering exponent for the densification data is slightly above 0.4, indicating that the lattice diffusion is responsible for the densification during the initial stage for the *MK* composite. In order to determine the activation energy of the densification during the initial stage of sintering, the Semilogarithmic law[25] was utilized:

$$\rho = \rho_0 + KLn(\frac{t}{t_0}) \qquad 6\text{-}5$$

where ρ_0 is an initial density at time (t_0), ρ is a density at time (t) and K is a temperature dependent parameter, calculated from the following equation in which Q is an activation energy of densification, T is an absolute temperature and R is a gas constant:

$$K = K_0 exp(-\frac{Q}{RT}) \qquad 6\text{-}6$$

Based on the above equations, the relative density versus the natural logarithm of time was plotted for the selected temperatures. The slope of the curves in Figure 6-28 (the K values) were used for the activation energy measurement. Figure 6-29 shows the variation of ln(K) versus

(1/*T*). According to the equation 6-6, the slope of the curve is the activation energy of sintering in the initial stage. Based on the plot, the activation energy of sintering for the *MK* composite is about 317 kJ/mol[*].

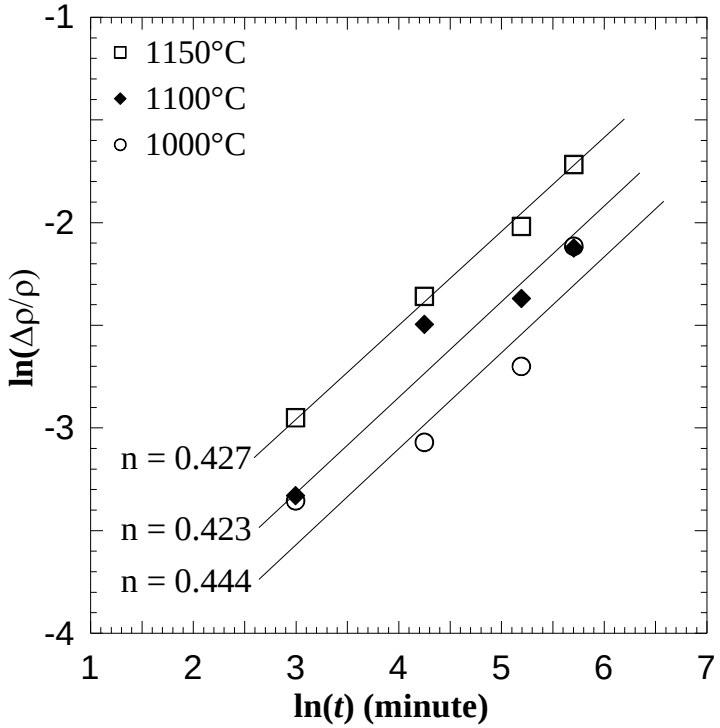

Figure 6-27. Sintering kinetics of the initial stage of sintering of *MK* composite; the 95% confidence intervals for n values are ± 0.02 (2σ)

In order to correlate this value with a sintering mechanism, the role of MgO on the densification has also been considered, since the microstructure of the *MK* composite consists of both MgO and spinel. A comparison between the activation energy of the diffusion of oxygen in MgO (261 kJ/mol)[158] and the oxygen diffusion in the $MgAl_2O_4$ spinel (415 kJ/mol)[159] shows that

[*] Due to the lack of information about the initial stage sintering of $MgCr_2O_4$ and chromite in the literature; the similarities between the sintering of Cr_2O_3 and $MgCr_2O_4$ and also similarities between the structure of $MgAl_2O_4$ and $MgCr_2O_4$ all the kinetic data in this study was compared to the spinel and Cr_2O_3.

although MgO plays an important role in the densification of magnesia-chromite refractory composites, it is not a rate controlling species in the microstructure.

Furthermore, this value is very close to the activation energy of $MgCr_2O_4$ formation (323 kJ/mol)[104], indicating the activation energy required for the cation movement in the closed packed array of oxygen in spinel structure. In addition, since Cr^{+3} is the rate controlling species, this value indicates the activation energy of Cr^{+3} mobility in the $MgCr_2O_4$ structure.

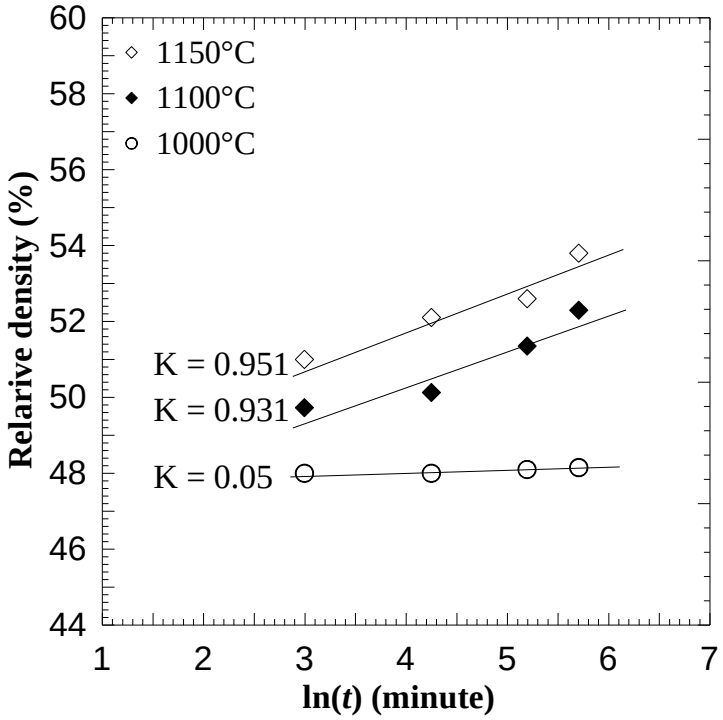

Figure 6-28. Variation of relative density versus the sintering time during the initial stage of sintering

Considering the above values, one can conclude that the volume diffusion of Cr^{+3} in the spinel phases is a rate controlling mechanism in the initial stage sintering of *MK* composite. This conclusion can be compared to the on drawn by Hagel et al.[88], who reported that the oxygen diffusion was the rate controlling mechanism during the densification at this stage. Since the

oxygen ion is significantly larger than the chromium ion (r_{O2}: 1.32 Å vs. r_{Cr}^{+3}: 0.62 Å)[109], its activation energy of diffusion (425 kJ/mol)[88] is significantly higher than that of Cr^{+3} (255 kJ/mol), thus the former conclusion by Hagel is acceptable.

Considering the above discussion and the fact that the activation energy of diffusion from the grain boundaries is smaller than from the lattice, it is hypothesized that the initial stage sintering of the *MK* composite is governed by the oxygen diffusion from the grain boundaries. Hagel[88] also mentioned that the same mechanism was observed during the sintering of pure Cr_2O_3.

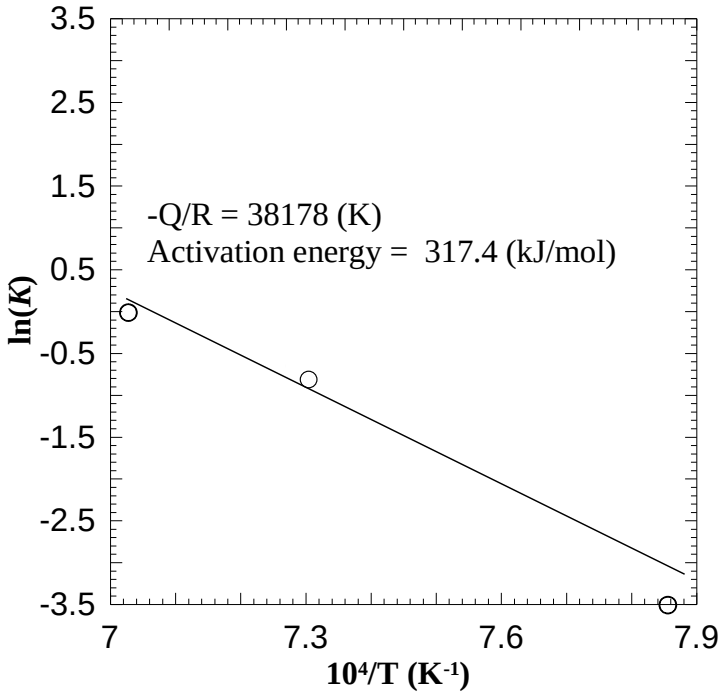

Figure 6-29. Calculation of activation energy of initial stage of sintering of *MK* composite using equations 6-5 and 6-6

Figure 6-30 illustrates the variation of $\ln(\Delta\rho/\rho)$ versus ln(t) for the nano *MK* composite (*NMK*). The sintering exponent n = 0.35 is lower than the value obtained for the *MK* composite, indicating that contrary to the *MK* composite, where the volume diffusion was governing the

densification, the grain boundary diffusion is governing the densification of the *NMK* composite. Such a change in the densification mechanism can only be correlated to the dramatic increase in the grain boundary area in the nano *MK* powders in comparison to the micron *MK* powders.

The nano-*MK* (*NMK*) powders have a large fraction of atoms in the grain boundary, which provides a high concentration of short diffusion paths. Therefore, enhanced diffusivity compared to the micron *MK* powders was expected. As a result of the increased sinterability of the *NMK* composites, the sintering temperature of these powders was lower than for the *MK* composites.

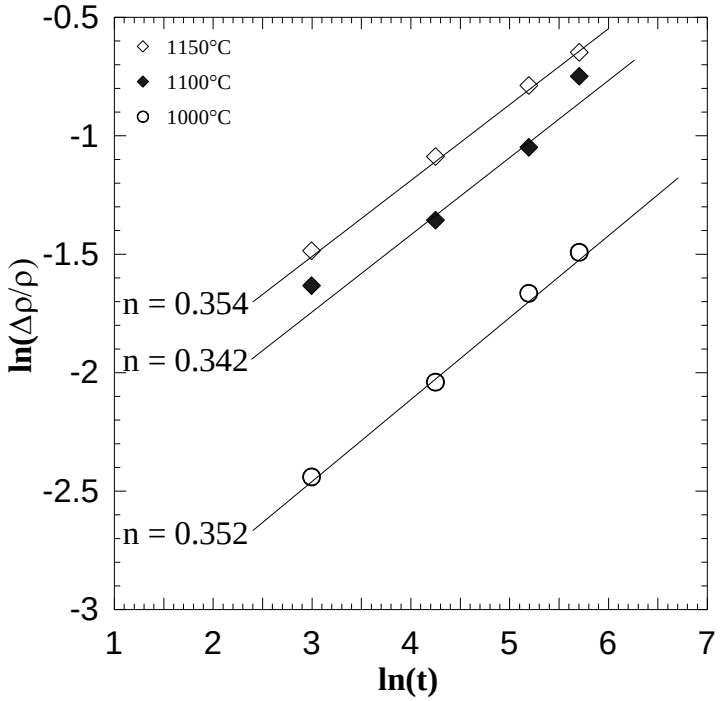

Figure 6-30. Kinetics study on the initial stage sintering of *NMK* composite according to the two sphere model (Kingery et al.[5, 16])

The effect of particle size on the densification of WC-Co composites wasinvestigated by Porat et al.[160]. They showed that the reduction in particle size to the nano range not only enhanced the densification, but also changed the sintering mechanism of WC-Co from liquid phase sintering to solid state mechanism. He et al.[161] showed the same phenomenon studying the

sintering of nano and micron size Al_2O_3. Neves et al.[100] studied the initial stage sintering of ZnO and showed that the activation energy of nano ZnO (202 kJ/mol) was significantly below the values reported for the micron size ZnO (270–320 kJ/mol).

In order to calculate the activation energy of sintering during the initial stage for the *NMK* composite, the same approach was used to analyze the data ; however, the data did not fit the Kingery two-sphere model[24]. This model could also not be used for the analysis of densification results for the intermediate and final stage of sintering.

Several investigations addressed the densification models for analyzing the densification data during the final stage of sintering. Coble[30]developed a model assuming a tetrakaidecahedra distribution of pore channels along the edges. According to this geometrical model, the densification rate is a function of grain boundary and lattice diffusion, which are expressed in equations 2-3 and 2-4. It is impossible to solve the equations since the relationship between G and ρ is still unknown. Several explanations and models were developed based on the Kingery and Coble's models; however, none of them were solvable mathematically[162, 162, 163].

Lately, a new model has been proposed by Su and Johnson[23] - Master Sintering Curve (*MSC*). The *MSC* predicts the sintering behavior and the activation energy of sintering of a given powder with specific particle size and green density, regardless of the sintering profile. The MSC model have been successfully used to sintering systems such as YSZ[164], $MgAl_2O_4$[165], TiO_2[166].

In this model, the grain growth was assumed to be only a function of density. The model was constructed based on the combined stage sintering model by Hansen[167], in which the immediate densification rate of a given compact was related to the volume, grain boundary diffusion coefficients, microstructure parameters and surface tensions, as follow:

$$-\frac{d\rho}{3\rho dt}=\frac{\gamma\Omega}{kT}\left(\frac{\Gamma_V D_V}{G^3}+\frac{\Gamma_b \delta D_b}{G^4}\right) \quad 6\text{-}7$$

where γ is a surface energy, Ω is an atomic volume, δ is a grain boundary width, Γ_b and D_b are microstructure scaling factor for the grain boundary and the grain boundary diffusion coefficient respectively, Γ_v and D_v are microstructure scaling factor for the lattice and the lattice diffusion coefficient respectively. Based on MSC theory, the sintering rate, microstructure and temperature parameters can be separated into two equations, as follows: ϕ(ρ) demonstrates all the microstructure evolution during sintering (6-8), and Θ(ρ) shows the sintering parameters depending on the thermal history (6-9):

$$\emptyset(\rho)=\frac{k}{\gamma\Omega D_0}\int_{\rho_0}^{\rho}\frac{(G(\rho))^n}{3\rho\Gamma(\rho)}d\rho \quad 6\text{-}8$$

$$\theta(t,T(t))=\int_0^t\frac{1}{T}exp(\frac{Q}{RT})dt \quad 6\text{-}9$$

where ϕ(ρ) incorporates G(ρ), scaling parameters Γ(ρ) ,and Q is an activation energy of sintering. Since the latter equations are equal, the *MSC* that demonstrates the relation between density and ϕ(ρ) can be constructed from the experimental results by knowing or estimating the activation energy of sintering and plotting the curve of density versus the Θ(ρ) function.

In order to estimate the apparent activation energy of sintering *MK* and *NMK* composites, the *MSC* theory was applied to analyze the densification data. *MK* and *NMK* compacts were isothermally sintered at temperatures ranging from 1150°C to 1500°C and quenched to room temperature after different sintering durations. The density was then measured and used to construct the master sintering curve, as shown in Figure 6-31 for the *MK* composite.

Since no information about the activation energy of $MgCr_2O_4$ or MgO-chromite ceramics was available, the value was estimated based on the activation energy values reported for

sintering of MgO, $MgAl_2O_4$ and $MgCr_2O_4$[102,103]. In this regard, a few Q values ranging from 250 kJ/mol to 650 kJ/mol were used in a primary estimation. As mentioned earlier, the heating profile does not affect the *MSC*, which only depends on the powder type, grain size and green density of compacts. Therefore, if the right activation energy is estimated, all sintering data should converge to a single curve.

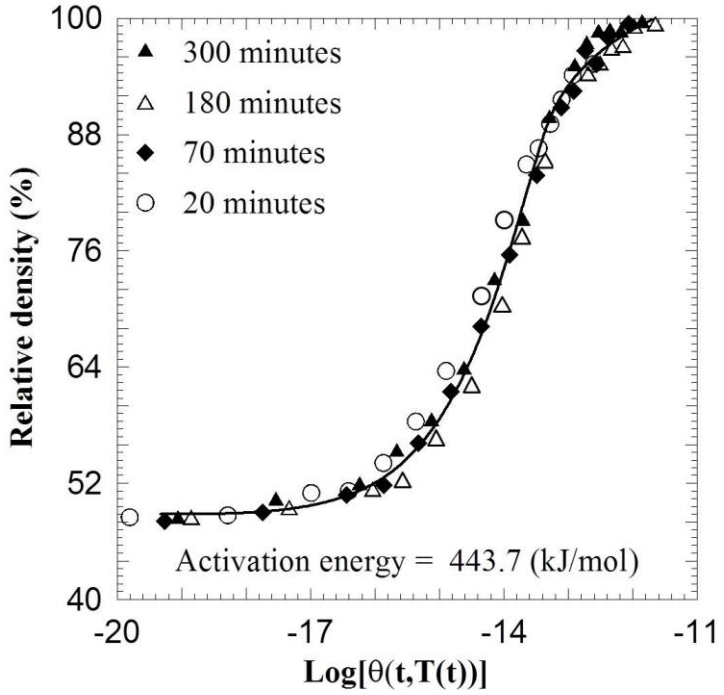

Figure 6-31. *MSC* of isothermally sintered *MK* composite

A polynomial curve (fitted to all data points and the sum of the residual squares of the points with respect to the fitted curve) was used to quantify the measure of the convergence. Figure 6-32 shows the variation of the mean residual squares for the estimated activation energies. The minimum mean residual square occurs at about 444 kJ/mol, indicating that the apparent activation energy of sintering for the *MK* composite is 444 kJ/mol. Several studies have been performed on pressureless sintering of spinel[79,81]. Bratton[77,81] investigated the initial and the

intermediate stages sintering of a $MgAl_2O_4$ powder, and showed that the rate controlling mechanism was the lattice diffusion of oxygen in the $MgAl_2O_4$ lattice.

Ting et.al.[79] also determined the sintering mechanisms for magnesia and alumina rich spinels, and showed that the oxygen lattice diffusion was responsible for the densification of $MgAl_2O_4$ spinel. Several activation energies for the diffusion of oxygen in spinel have been reported. Reddy[159] reported that the oxygen self-diffusion coefficient in spinel is about 440 kJ/mol, which is higher than the value reported for the self-diffusion of Al^{+3} (250 kJ/mol)[168] and Mg^{+2} (360 kJ/mol)[168] in spinel. Nassira et al.[165] reported the activation energy of grain boundary diffusion of oxygen in $MgAl_2O_4$ spinel at ~265 kJ/mol, which was smaller than the activation energy of lattice diffusion. Comparing the measured activation energy for the *MK* composite to the values reported for $MgAl_2O_4$, it is hypothesized that the lattice diffusion of oxygen is the rate determining species during the sintering of $MgCr_2O_4$.

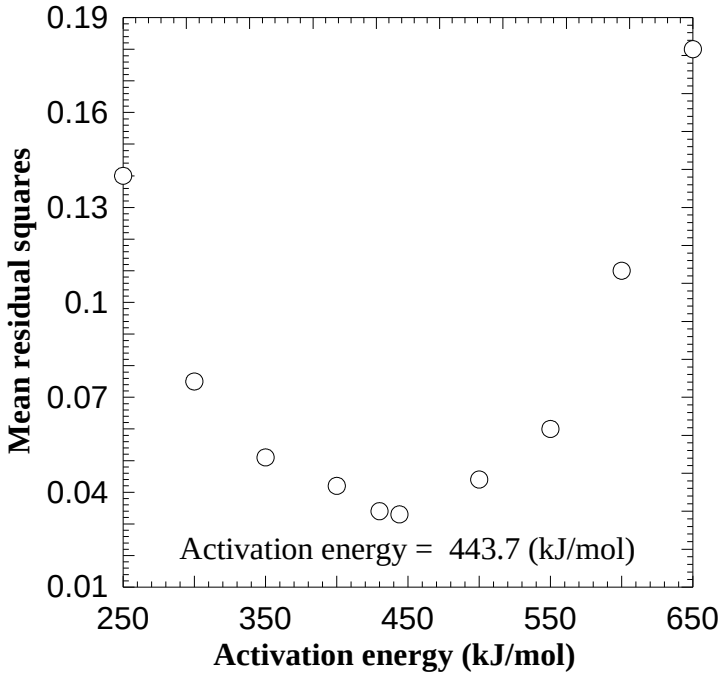

Figure 6-32. The variation of mean residual squares for estimated activation energies; the minimum was obtained at ~444 kJ/mol

Figure 6-33 and Figure 6-34 show the *MSC* curve and the variation of the mean residual squares for the estimated activation energies for *NMK* composite. All curves converged when the activation energy of 302 kJ/mol was used for the data analysis. This value is considerably lower than the reported value for the *MK* composite, indicating that different mechanisms are responsible for its densification. It was already explained that reducing the particle size to the range of nano size increases the volume of grain boundaries in comparison to the micro size powder. As a result, the grain boundary would react as a short circuit for diffusion and results in the faster densification. As shown in Figure 6-26, the onset sintering temperature of *NMK* composite was about 200°C lower than that of *MK* composite, which verifies the above explanation.

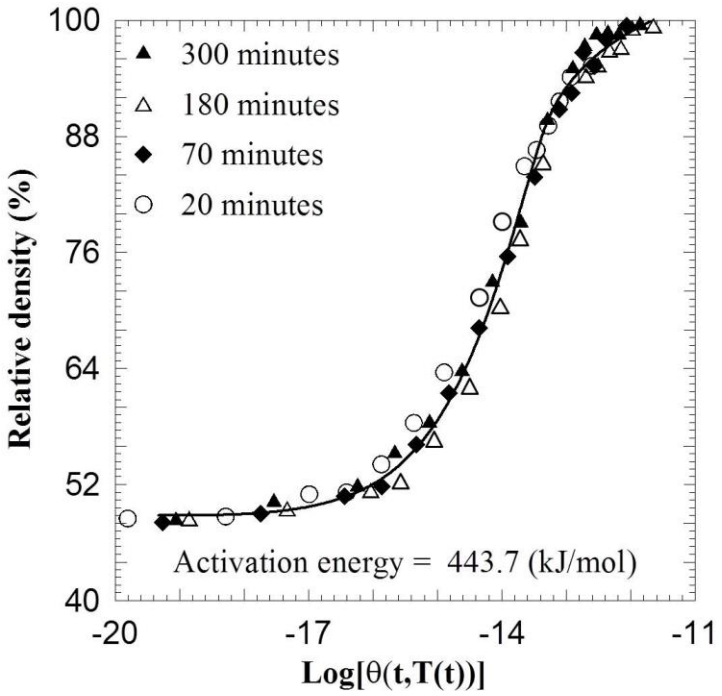

Figure 6-33. MSC of isothermally sintered *NMK* composite

In addition, the activation energy obtained for the *NMK* composite (303 kJ/mol) was close to the value reported for the self-diffusion of cations in the spinel structure and also for the self-

diffusion of cations in the parent oxide. The activation energy of diffusion of Mg and Cr in MgO and Cr_2O_3 is 261 and 255 kJ/mol[11,17,88] respectively. Comparing the values to the activation energy of the *NMK* composite and considering the fact that oxygen diffusion in an oxide structure is lower than cations diffusion, it is expected that the oxygen diffusion is still the slowest species during the sintering of *NMK* composite.

Grain boundary is a sink for the lattice imperfections, which are short paths for diffusion; therefore, a lower activation energy for the densification of ions is expected at grain boundaries[4,5]. As a result, the lower activation energy for the sintering of the *NMK* composite in comparison to the *MK* composite is attributed to the oxygen diffusion through the grain boundaries of the *NMK* composite.

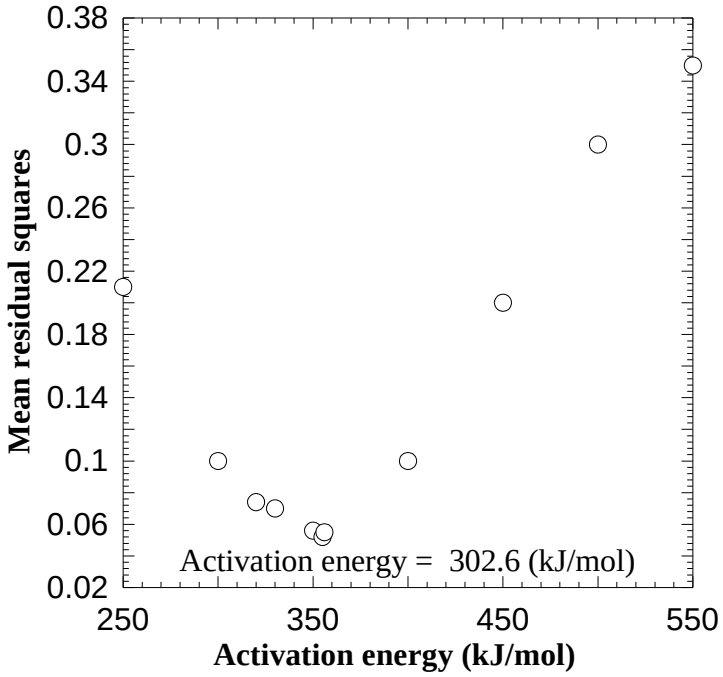

Figure 6-34. The variation of mean residual squares for estimated activation energies; the minimum was obtained at ~303 kJ/mol

Chapter 7. Conclusions and future work

7.1 The influence of spinel forming oxides (Fe_2O_3 and Al_2O_3) on sintering of $MgCr_2O_4$

The kinetics of $MgCr_2O_4$ formation in the presence of Al and Fe was studied using the simultaneous thermal analysis (*DSC/TGA*) method. Based on the obtained results, the activation energy of spinel formation and the Avrami constant were calculated. It was shown that the addition of Al_2O_3 reduces the activation energy of $MgCr_2O_4$ spinel formation from 329±7 kJ/mol to 206±3 kJ/mol. In contrast, Fe_2O_3 was less effective in reducing the formation activation energy of $MgCr_2O_4$ spinel, lowering it to 298±11 kJ/mol. These activation energies correlate well with the results of previous studies.

Based on the comparison between the measured activation energies of spinel formation and the activation energies of the diffusion of cations in their parent oxides, it is concluded that the diffusion of Cr^{+3} is the rate controlling mechanism during spinel formation in all compositions. However, the early formation of $MgAl_2O_4$ retards the spinel formation and increases the quantity of the unreacted oxides at the calcination temperature (850°C). It is proposed that faster $MgAl_2O_4$ spinel formation could be attributed to the smaller cation radii of Al^{+3} (0.54 Å), in comparison to that of Fe^{+3} (0.67 Å) and Cr^{+3} (0.62 Å).

The sintering behavior of $Mg[Cr_{1-x}Me_x]_2O_4$ (Me: Al, Fe, and Sn; $0 \leq x \leq 0.2$) compositions was investigated by comparing the relative density for the different sintering temperatures of 1200°C to 1500°C, for 300 min soak. The results showed that Al_2O_3, Fe_2O_3, and SnO_2 enhanced the densification of $MgCr_2O_4$. The increase in the density in presence of Al_2O_3 and Fe_2O_3 was attributed to the solid solution formation in the presence of the sintering additives. Due to the

size mismatch between the cations and also to their inherent location preference in a spinel structure, it is proposed that the solid solution formation of $MgCr_2O_4$ lattice might have been distorted, and consequently changed the diffusion coefficient of the cations in favor of densification.

Extensive *XRD* analyses were performed on the specimens that were quenched from the sintering temperatures. For the first time, the cation distribution in a spinel structure (expressed through the "inversion parameter") was calculated from the *XRD* data for the $Mg[Cr_{1-x}Me_x]_2O_4$ system. The results showed that for $Mg[Cr_{0.8}Fe_{0.2}]_2O_4$ the inversion parameter increased from 0.16 at 750°C to 0.24 at 1475°C. For $Mg[Cr_{0.8}Al_{0.2}]_2O_4$ the inversion parameter was 0.11 and 0.17 at 750°C and 1475°C respectively. This indicates that in both cases the inversion increased with the sintering temperature.

The correlation between the inversion parameter and the densification results revealed that the increase in the inversion parameter enhanced the densification. The addition of Al_2O_3 and Fe_2O_3 increased the inversion parameter and densification rate; however, the inversion parameter of $Mg[Cr_{0.8}Al_{0.2}]_2O_4$ was less than that of $Mg[Cr_{0.8}Fe_{0.2}]_2O_4$. It is hypothesized that the high degree of inversion resulted in enhancement of the sintering driving force as a result of cation interchange between the octahedral and the tetrahedral sites.

To understand the contribution of solid solution formation and proposed inversion phenomenon on the densification behavior of $MgCr_2O_4$, the effects of SnO_2 as a sintering additive were also studied. The SnO_2 was selected for this purpose because it forms Mg_2SnO_4, which is a normal spinel in a wide temperature range. The results showed the addition of 0.2 mol% SnO_2 increased the lattice parameter of $MgCr_2O_4$ from 8.3351±0.002 Å to 8.4015±0.002 Å, and increased the density of $MgCr_2O_4$ from 51% to 59% via the solid solution formation

mechanism. The comparison between the densification results of $MgCr_2O_4$ in the presence of SnO_2 and Fe_2O_3 reveals that the inversion phenomenon could be responsible for the better performance of Fe_2O_3 in comparison to SnO_2 in increasing the density, since on one hand for both compositions same green density were recorded, and on the other hand they both have unlimited solid solubility with $MgCr_2O_4$.

In order to quantify the effects of solid solution formation and of the inversion phenomenon on the densification of $MgCr_2O_4$, the effect of Fe_2O_3 and SnO_2 on the densification of Cr_2O_3 was also studied, and the results were compared to the densification data obtained from sintering of $MgCr_2O_4$ in the presence of SnO_2 and Fe_2O_3.

There is unlimited solid solubility in $MgCr_2O_4$-Mg_2SnO_4, $MgCr_2O_4$-$MgFe_2O_4$, and Cr_2O_3-Fe_2O_3 systems. In contrast, it was shown that the maximum solid solubility of SnO_2 in Cr_2O_3 is ~0.5 mol% at 1475°C in air. Therefore, for the Cr_2O_3-$v$$SnO_2$ compositions, an increase in SnO_2 up to 0.5 mol% raised the final density from 51 to 59%. However, the increase in SnO_2 content beyond the solid solubility limit of SnO_2 in Cr_2O_3 decreased the density. In contrast, for $MgCr_2O_4$-Mg_2SnO_4 compositions, the increase in SnO_2 continuously increased the density up to 64%, since there is no solid solubility limit in the $MgCr_2O_4$-Mg_2SnO_4 system. This shows that the formation of the solid solution is responsible for the enhanced densification of $MgCr_2O_4$ and Cr_2O_3.

A comparison between the density of $MgCr_2O_4$-$N_A$$MgFe_2O_4$ and Cr_2O_3-$v$$Fe_2O_3$ compositions, quenched from 1475°C after 300 minutes sintering, showed that the addition of Fe_2O_3 increased the density of both $MgCr_2O_4$ and Cr_2O_3. However, the extent of densification for the $MgCr_2O_4$-$N_A$$MgFe_2O_4$ compositions was higher than for Cr_2O_3-$v$$Fe_2O_3$. For instance, 10 mol% Fe_2O_3 concentrations resulted in 68% density of $MgCr_2O_4$, and 56% density of Cr_2O_3.

This difference in the densification of $MgCr_2O_4$-$N_A MgFe_2O_4$ and Cr_2O_3-vFe_2O_3 is attributed to the inversion phenomenon, which is responsible for the better densification.

7.2 The effects of spinel forming oxides on the sintering of magnesia-chromite composites

The effects of Cr_2O_3, Al_2O_3 and Fe_2O_3 on the densification of magnesia-chromite refractory composites (MgO-$Mg[Cr_{1-x}Me_x]_2O_4$; Me: Al, Fe) were investigated. The densification behavior of twelve compositions (*MK*1-*MK*12) at different sintering temperatures was compared. Also, the effect of sintering additives on the dihedral angels was studied. The results showed that for the compositions with the high chromium content ($Cr_2O_3 \geq 6.9$ mol%) the relative density would not increase above 80% even at 1600°C for 300 minutes. In contrast, the compositions with 2.7 mol% Fe_2O_3 and 4.9 mol% Al_2O_3 densify to 96% at 1475°C after 300 minutes. In addition, Fe_2O_3 was also shown to be more effective than Al_2O_3 in increasing the densification of the magnesia-chromite composites.

The dihedral angles of the composites with different concentrations of the sintering additives were measured and correlated to the densification results. It was shown that the increase in Cr_2O_3 content from 4.9 to 8.9 mol% increased the average dihedral angle from 80 to 128 degrees. The increase in Al_2O_3 (4.9-8.9 mol%) decreased the dihedral angle from 124 to 75 degrees. The increase in Fe_2O_3 content from 0.9 to 4.9 mol% also decreased the dihedral angle from 120 to 75 degrees. It is concluded that the enhanced densification at the higher concentration of Fe_2O_3 can be attributed to the smaller dihedral angle; however, there is an optimum composition at which the maximum density of 96% could be achieved at 1475°C. The optimum composite contained 6.9 mol% Al_2O_3, 6.9 mol% Cr_2O_3, 2.7 mol% Fe_2O_3 and MgO. The sintering behavior of this optimized composition [MgO-6.9Al_2O_3-2.7Fe_2O_3-6.9Cr_2O_3] (called

MK), was further investigated by sintering samples isothermally for different durations and temperatures. The results show the optimum sintering temperature of 1475˚C for 70 minutes.

In order to study the effect of the particle size on the densification behavior of *MK* composites, the nano particles of the optimized magnesia-chromite refractory composite with the particle size of 20 nm was synthesized via Pechini's method and called *NMK*. The *NMK* composite powders were further processed in the same way as the *MK* composites. The results showed that the decreasing of the particle size of magnesia chromite composites from 1.2 μm to 20 nm reduced the onset sintering temperature by about 200°C. The onset sintering temperature for the *MK* composite was ~1200°C and for the *NMK* composite was ~1000°C. When sintered at 1475°C for 300 minutes, the density for *NMK* was ~99%, while for *MK* it was 95%. For *NMK* the 95% density was achieved at ~1300°C, while the same density was achieved for *MK* at 1475°C. In addition, the minimum time that was required to reach to 95% density at 1475°C for *MK* and *NMK* was ~70 and ~20 minutes respectively. This indicated that the densification rate of *NMK* is higher than of *MK*. In other words, reducing the particle size of the optimized magnesia-chromite composite to the range of 20 nm increased the densification rate ~3.5 times. The drawback of using nano particles was however the extensive grain growth. During the sintering at 1600°C the average grain size of *NMK* composites increased dramatically from ~40 nm to ~8000 nm, while for the same sintering condition, the grain size of the *MK* composite increased from 1.2 μm to 7 μm.

For the first time, the sintering kinetics parameters were measured in this work for magnesia-chromite composites, based on the master sintering curve theory. The results showed that the activation energy of sintering of the composites with micron-size grains was 443.7 kJ/mol, whereas the activation energy of the nano-sized composite is reported to be 302.6

kJ/mol. A comparison between these data and the activation energy of diffusion of ions in spinel revealed that in both cases the diffusion of oxygen was the rate controlling mechanism of sintering for the *MK* and *NMK* composites. However, the lower activation energy of nano-sized composite was attributed to the diffusion of oxygen through grain boundaries, in contrast to the higher activation energy in micron sized composite, which was attributed to the lattice diffusion of oxygen.

In this study we showed that the solid solution formation could enhance the densification of $MgCr_2O_4$. It was found that the effect of sintering additives on the densification is controlled by the solid solubility of the additives in the host spinel structure, by the rate of solid solution formation and how it affects the cation distribution, and by the unit cell dimensions of the host structure. We introduced a hypothesis based on which the inversion phenomenon contributes to the densification of magnesia-chromite spinel.

Further work should be done in addition to these observations to develop a quantitative relationship between the inversion parameter and the densification. Such analysis for other spinel structures could develop a model which might facilitate better selection of sintering additives for spinel structures. This could be important for sintering of electronic ceramics with spinel structure, where the concentration and type of additives change their performance significantly. It is recommended to use normal spinels with low sintering temperature ($T<1100°C$) as host structures, because high sintering temperatures may induce inversion in the host structure.

In order to calculate the inversion parameter several assumptions were made to simplify the calculation of the *XRD* intensity. In addition, the procedure that was introduced by Porta[3] and used by us was based on assumptions which might affect the results. According to this method, the intensity was measured for each peak separately. To solve the intensity equations, the

estimated value for the inversion parameter was changed with 0.01 intervals, which is not very accurate for inversion parameter measurements. In fact, in the previous studies the inversion parameter was reported with three significant figures. Had we been able to perform the Rietveld analysis, the desired accuracy might have been achieved, since with this technique, all the peaks would be analyzed in the same time. Therefore, it is recommend that the cation distribution in the spinel structures is calculated based on more accurate analysis techniques such as the Rietveld analysis.

We have successfully applied the master sintering curve theory to analyze the densification results of magnesia-chromite refractories with the optimum composition (*MK*) and to calculate the sintering activation energy. We have determined that the dominant sintering mechanism in the *MK* composite was the diffusion of oxygen through either lattice or grain boundary. However, the isothermal sintering data may introduce an additional source of error in the calculation of the sintering activation energy. Therefore, it is recommended that the results of these experiments are verified with dilatometric studies by recording the dimensions of one specimen over the course of sintering. This would reduce the errors introduced in the isothermal studies due to the variation of the initial conditions for each specimen.

The master sintering curve theory assumes that the initial conditions of specimens i.e. green density, porosity, particle size, particle shape and chemical composition, are similar. In our isothermal studies, the chemical compositions of the particles, the particle size and particle shape were similar for all specimens, as they were prepared from one batch of synthesized composite. However, the green density of specimens varied in the 0.5-1.0 % range, which might induce some error in the activation energy calculations.

In this regard, the application of dilatometry to calculate the activation energies of the studied compositions is recommended.

In this study we showed that it is possible to sinter a magnesium-chromite refractory composite to nearly full density (~98%) in air at temperatures as low as 1475°C, which is about 300°C below the current sintering temperatures. The key component in reducing the sintering temperature was the addition of Fe_2O_3, as it formed an inverse solid solution with $MgCr_2O_4$. In addition, we found that reducing the particle size of the magnesia-chromite composite with the optimum composition to ~20 nm reduced the sintering temperature to 1350°C, which is 425°C below the sintering temperature that is currently used for these composites. Based on these results it is recommended that the performance of a mag-chrome brick with *MK* composite as the binding system is investigated in-field, and compared with the performance of industrially available mag-chrome bricks. In another study, which is not reported here, we sintered a mag-chrome brick, with the *MK* binding system, at 1475°C for 5 hours.

We showed that the physical properties of our brick, including strength, density and porosity, were comparable to the industrially available refractories. For this reasons, a similar in-field performance is expected for our brick. Since our brick is sintered at 1475°C and the industrially available brick is sintered at 1700°C, the comparable performance of the two bricks opens the opportunities to prepare mag-chrome bricks with lower sintering temperatures.

References

1. MN. Rahaman, Ceramic Processing and Sintering, Marcel Dekker, United state of America, 1995.

2. M. A. Alper, High temperature oxides. New York and London, Academic press, 1970.

3. P. Porta, F. Stone, R. Turner, The distribution of nickel ions among octahedral and tetrahedral sites in $NiAl_2O_4$-$MgAl_2O_4$ solid solutions, J. Solid State Chem., 1974,11, 135-147.

4. S. Kang. Sintering Processes in Sintering, Oxford, Butterworth-Heinemann, 2005, 3-8.

5. German RM. Sintering Theory and Practice, John Wiley& sons Inc., United States of America, 1996.

6. M. A. Alper, Refractory Materials: A series of monographs, Ref. Mater., New York and London, Academic Press, 1970.

7. M. A. Alper, R. N. McNally, R. C. Doman, F. G. Keihn, Phase equilibria in system MgO-$MgCr_2O_4$, J. Am. Ceram. Soc., 1964, 47, 30-33.

8. A. C. Schacht, Refractories Handbook, Marcel Dekker, 2004.

9. M. A. Braulio, L. R. Bittencourt, V. Pandolfelli, Magnesia grain size effect on in situ spinel refractory castables, J. Eur. Ceram. Soc., 2008, 28, 2845-2852.

10. K. Rozenburg, I. E. Reimanis, H. Kleebe, R. L. Cook, Chemical interaction between LiF and $MgAl_2O_4$ spinel during sintering, J. Am. Ceram. Soc. 2007, 90, 2038-2042.

11. P. D. Ownby, G. E. Jungquist, Final sintering of Cr_2O_3, J. Am. Ceram. Soc., 1972, 55, 433-436.

12. A. Yamaguchi, T. Okamura, Sintering and compounds in the $MgCr_2O_4$-TiO_x system, Ceram. Int. 1989,15,147-153.

13. A. Ghosh, M. K. Haldar, S. K. Das, Effect of MgO and ZrO_2 additions on the properties of magnesite-chrome composite refractory, Ceram Int., 2007, 33, 821-825.

14. J. P. Singh, Effect of ZrO_2 inclusions on fracture properties of $MgCr_2O_4$, J. Mater. Sci., 1987, 22, 2685-2690.

15. T. Fang, J. Tsay, Effect of pH on the chemistry of the barium titanium citrate gel and its thermal decomposition behavior, J. Am. Ceram. Soc., 2001, 84, 2475-2478.

16. S. L. Kang, Y. Jung, Sintering kinetics at final stage sintering: Model calculation and map construction, Acta Mater., 2004, 52, 4573-4578.

17. D. Chen, E. H. Jordan, M. Gell, Pressureless sintering of translucent MgO ceramics, Scr. Mater, 2008, 59, 757-759.

18. J. M. Brenan, C. F. Finnigan, W. F. McDonough, V. Homolova, Experimental constraints on the partitioning of Ru, Rh, Ir, Pt and Pd between chromite and silicate melt: The importance of ferric iron, Chem. Geol., 2012, 16-32, 302–303.

19. K. Rida, A. Benabbas, F. Bouremmad, M. A. Pena, A. Martinez-Arias, Influence of the synthesis method on structural properties and catalytic activity for oxidation of CO and C_3H_6 of pirochromite $MgCr_2O_4$, Applied Catal. A. Gen., 2010, 375,101-106.

20. A. Nakatsuka, H. Ueno, N. Nakayama, T. Mizota, H. Maekawa, Single crystal X-ray diffraction study of cation distribution in $MgAl_2O_4$-$MgFe_2O_4$ spinel solid solution, Phys. and Chem. of Miner. 2004, 31, 278-287.

21. D. S. McClure, The distribution of transition metal cations in spinels, J. Phys. and Chem. Solid., 1957, 3, 311-317.

22. W. D. Callister, Fundamentals of materials science and engineering, 5th ed., United States of America, John Wiley and Sons, Inc., 2001.

23. H. Su, D. L. Johnson, Master sintering curve: A practical approach to sintering, J. Am. Ceram. Soc., 1996, 79, 3211-3217.

24. W. D. Kinger, M. Berg, Study of the initial stages of sintering solids by viscous flow, evaporation-condensation, and self-diffusion, J. Appl. Phys. 1955, 26, 1205-1212.

25. R. Cobel, Initial sintering of alumina and hematite, J. Am. Ceram. Soc., 1958, 41, 55-62.

26. D. L. Johnson, I. B. Culter, Diffusion sintering: initial stage sintering models and their application to shrinkage of powder compacts, J. Am. Ceram. Soc., 1963, 46, 541-545.

27. F. Tietz, F. J. Dias, D. Simwonis, D. Stöver, Evaluation of commercial nickel oxide powders for components in solid oxide fuel cells, J. Eur. Ceram. Soc., 2000, 20, 1023-1034.

28. W. S. Young, I. B. Culter, Initial sintering with constant rates of heating, J. Am. Ceram. Soc., 1970, 53, 659-663.

29. W. E. Kingston, Congres, The physics of powder metallurgy, New York etc.: McGraw Hill, 1951.

30. R. L. Coble, Sintering crystalline solids. II. experimental test of diffusion models in powder compacts, J. Appl. Phys., 1961, 32, 793-799.

31. A. K. Karkar, Sintering kinetics based on geometric models, J. Am. Ceram. Soc., 1968, 51, 236-236.

32. P. J. Jorgensen, Modification of sintering kinetics by solute segregation in Al_2O_3, J. Am. Ceram. Soc., 1965, 48, 207-210.

33. D. L. Johnson, A general model for the intermediate stage of sintering, J. Am. Ceram. Soc., 1970, 53, 574-577.

34. J. Zhao, M. P. Harmer, Sintering kinetics for a model final-stage microstructure: A study of Al_2O_3, Philos. Mag. Lett., 1991, 63, 7-14.

35. X. Wang, Z. Fang, H. Y. Sohn, Grain growth during the early stage of sintering of nanosized WC-Co powder, Inter. J. Ref. Metal. Hard Mater., 2008, 26, 232-241.

36. R. J. Tilley, Defects in Solids, John Wiley& sons Inc., United States of America, 2008.

37. E. J. Verwey, E. L. Heilmann, Physical properties and cation arrangement of oxides with spinel structures I. cation arrangement in spinels, J. Chem. Phys., 1947, 15, 174-180.

38. A. Miller, Distribution of cations in spinels, J. Appl. Phys., 1959, 30, S24-S25.

39. H. S. C. O'Neil, A. Navrotsky, Cation distributions and thermodynamic properties of binary spinel solid solutions, J. Am. Miner., 1984, 69, 733-753.

40. G. B. Andreozzi, F. Princivalle, Kinetics of cation ordering in synthetic $MgAl_2O_4$ spinel, J. Am. Miner., 2002, 87, 838-844.

41. H. Furuhashi, M. Inagaki, S. Naka, Determination of cation distribution in spinels by X-ray diffraction method, J. Inor. Nucl. Chem., 1973, 35, 3009-3014.

42. W. C. Allen, The series $MgCr_2O_4$-$MgFe_2O_4$. J. Am. Ceram. Soc., 1968, 51, 485-490.

43. G. C. Ulmer, Oxidation-reduction reactions and equilibrium phase relation at 1300°C at oxygen pressures from 0.21 E^{-14} atm for the spinel solid solution series $FeCr_2O_4$-$MgCr_2O_4$ and $FeCr_2O_4$-$MgAl_2O_4$. Penn. State. Univ. University park, 1964.

44. L. V. Morozova, V. P. Popov, Synthesis and investigation of magnesium chromium spinel, Glass Phys. Chem., 2010, 36, 86-91.

45. H. Moriwake, I. Tanaka, F. Oba, Y. Koyama, H. Adachi, Formation energy of Cr/Al vacancies in spinel $MgCr_2O_4$ and $MgAl_2O_4$ by first-principles calculations, Phys. Rev. B. , 2002, 65, 153103.

46. K. Hoshino, N. L. Peterson, Cation self-diffusion in Cr_2O_3, J. Am. Ceram. Soc., 1983, 66, c202-c203.

47. M. K. Rasmussen, A. S. Foster, B. Hinnemann, Stable cation inversion at the $MgAl_2O_4$ (100) surface, Phys. Rev. Lett., 2011,107, 036102.

48. S. T. Murphy, C. A. Gilbert, R. Smith, T. E. Mitchell, R. W. Grimes, Non-stoichiometry in $MgAl_2O_4$ spinel, Philos. Mag., 2010, 90, 1297-1305.

49. H. S. C. O'Neill, H. Annersten, D. Virgo, The temperature dependence of the cation distribution in magnesioferrite $MgFe_2O_4$ from powder *XRD* structural refinements and moessbauer spectroscopy, J. Am Miner., 1992, 77, 725-740.

50. D. Levy., V. Diella, M. Dapiaggi, A. Sani, M. Gemmi, A. Pavese, Equation of state structural behaviour and phase diagram of synthetic $MgFe_2O_4$, as a function of pressure and temperature. Phys. and Chem. Miner., 2004, 31, 122-129.

51. R. A. Candeia, M. A. F. Souza, M. I. B. Bernardi, $MgFe_2O_4$ pigment obtained at low temperature, Mater., Res., Bull., 2006, 41,183-190.

52. A. E. Paladino, Phase equilibria in the ferrite region of the system FeO-MgO-Fe_2O_3, J. Am. Ceram. Soc., 1960, 43, 183-191.

53. D. H. Speidel, Phase equilibria in the system MgO-FeO-Fe_2O_3, The 1300°C isothermal section and extrapolations to other temperatures. J. Am. Ceram. Soc., 1967, 50, 243-248.

54. Z. V. Marinkovic Stanojevic, N. Romcevic, B. Stojanovic, Spectroscopic study of spinel $ZnCr_2O_4$ obtained from mechanically activated ZnO-Cr_2O_3 mixtures, J. Eur. Ceram. Soc. , 2007, 27, 903-907.

55. J. Auvray, C. Gault, M. Huger, Evolution of elastic properties and microstructural changes versus temperature in bonding phases of alumina and alumina–magnesia refractory castables, J. Eur. Ceram. Soc., 2007, 27, 3489-3496.

56. A. Azhari, F. Golestani-Fard, H. Sarpoolaky, Effect of nano iron oxide as an additive on phase and microstructural evolution of mag-chrome refractory matrix, J. Euro. Ceram. Soc., 2009, 29, 2679-2684.

57. G. Drazic, M. Trontel, Preparation and properties of ceramic sensor elements based on $MgCr_2O_4$, Sens. Actuators, 1989, 18, 407-414.

58. H. Zargar, MR. Bayati, HR. Rezaie, Influence of nano boehmite on solid state reaction of alumina and magnesia. J. Alloy. Comp. 2010, 507, 443-447.

59. E. B. Watson, J. D. Price, Kinetics of the reaction MgO + Al_2O_3 → $MgAl_2O_4$ and Al-Mg interdiffusion in spinel at 1200 to 2000°C and 1.0 to 4.0 GPa, Geochim Cosmochim Acta. 2002, 66, 2123-2138.

60. A. Saberi, F. Golestani-Fard, M. Willert-Porada, Z. Negahdari, C. Liebscher, B. Gossler, A novel approach to synthesis of nanosize $MgAl_2O_4$ spinel powder through sol-gel citrate technique and subsequent heat treatment, Ceram. Int., 2009, 35, 933-937.

61. N. Yoshida, Y. Takano, M. Yoshinaka, K. Hirota, O. Yamaguchi, Formation, powder characterization and sintering of $MgCr_2O_4$ by the hydrazine method, J. Am. Ceram. Soc., 1998, 81, 2213-2215.

62. F. Tavangarian, R. Emadi, Synthesis and characterization of pure nanocrystalline magnesium aluminate spinel powder, J. Alloys. Compds., 2010, 489, 600-604.

63. C. Greskovich, V. S. Stubican, Interdiffusion studies in the system MgO-Cr_2O_3, J. Phys. Chem. Solids, 1969, 30, 909-917.

64. E. B. Rigby, I. B. Culter, Interdiffusion studies of the system Fe_xO-MgO, J. Am. Ceram. Soc., 1965, 48, 95-99.

65. E. Y. Sako, M. A. L. Braulio, E. Zinngrebe, S. R. van der Laan, VC. Pandolfelli, Fundamentals and applications on in situ spinel formation mechanisms in Al_2O_3–MgO refractory castables, Ceram Int. 2012, 38, 2243-2251.

66. H. Yu, D. Yeon, A. Van der, K. Thornton, Substitutional diffusion and kirkendall effect in binary crystalline solids containing discrete vacancy sources and sinks, Acta Mater., 2007, 55, 6690-6704.

67. H. S. C. O'Neill, A. Navrotsky, Simple spinels: crystallographic parameters, cation radii, lattice energies, and cation distribution, J. Am. Mineral, 1983, 68, 181-194.

68. A. Della Giusta, G. Ottonello, Energy and long-range disorder in simple spinels. Phys. Chem. Miner., 1993, 20, 228-241.

69. Y.M. Abbas, S. A. Mansour, M. H. Ibrahim, S. E. Ali, Microstructure characterization and cation distribution of nanocrystalline cobalt ferrite, J. Magn. Magn. Mater., 2011, 323, 2748-2756.

70. L. Kumar, P. Kumar, A. Narayan, M. Kar, Rietveld analysis of *XRD* patterns of different sizes of nanocrystalline cobalt ferrite, Int. Nano Lett., 2013,3,8.

71. F. Princivalle, F. Martignago, F. Nestola, A. D. Negro, Kinetics of cation ordering in synthetic $Mg(Al, Fe^{+3})_2O_4$ spinels, ejm, 2012, 24, 633-643.

72. T. Stachel, J. W. Harris, The origin of cratonic diamonds - constraints from mineral inclusions, Ore Geo. Rev., 2008, 34, 5-32.

73. K. T. Jacob, R. Patil, Activities in the spinel solid solution $Fe_xMg_{1-x}Al_2O_4$, Metal. Mater. Trans. B., 1998, 29, 1241-1248.

74. K. T. Jacob, C. K. Behera, Spinel-corundum equilibria and activities in the system MgO-Al_2O_3-Cr_2O_3 at 1473K, Metal. Mater. Trans. B. 2000, 31, 1323-1332.

75. K. T. Jacob, C. K. Behera, Equilibria involving the reciprocal spinel solid solution $(Mg_x\ Fe_{1-x})$ $(Al_yCr_{1-y})_2O_4$: Modeling and experiment, Metal. Mater. Trans. B., 2000, 31, 1247-1259.

76. S. Pal, AK. Bandyopadhyay, PG. Pal, S. Mukherjee, BN. Samaddar, Sintering behavior of spinel-alumina composites, Bull. Mater. Sci., 2009, 32,169-176.

77. RJ. Bratton, Initial sintering kinetics of $MgAl_2O_4$, J. Am. Ceram. Soc. 1969, 52, 417-419.

78. K. Rozenburg, IE. Reimanis, H. Kleebe, RL. Cook, Sintering kinetics of a $MgAl_2O_4$ spinel doped with LiF, J. Am. Ceram. Soc., 2008, 91, 444-450.

79. C. Ting, H. Lu, Defect reactions and the controlling mechanism in the sintering of magnesium aluminate spinel, J. Am. Ceram. Soc., 1999, 82, 841-848.

80. J. Huang, S. Sun, Y. Ko, Investigation of high-alumina spinel: Effect of LiF and $CaCO_3$ addition, J. Am. Ceram. Soc., 1997, 80, 3237-3241.

81. RJ. Bratton, Sintering and grain-growth kinetics of $MgAl_2O_4$, J. Am. Ceram. Soc., 1971, 54, 141-143.

82. H. U. Anderson, Influence of oxygen activity on the sintering of $MgCr_2O_4$, 1974, 57, 34-37.

83. JM. Neve, RL. Coble, Initial sintering of Cr_2O_3, 1974, 57, 274-275.

84. HC. Graham, HH. Davic, Oxidation/vaporization kinetics of Cr_2O_3, J. Am. Ceram. Soc., 1971, 54, 89-93.

85. SN. Roy, SR. Saha, SK. Guha, Sintering kinetics of pure and doped chromium oxide, J. Mater. Sci., 1986, 21, 3673-3676.

86. HEN. Stone, Sintering in ferric and chromic oxides. further work, J. Mater. Sci. , 1969, 4, 166-169.

87. HEN. Stone, Sintering in chromic oxide, Metallurgica, 1968, 77, 152-154.

88. WC. Hagel, PJ. Jorgensen, DS. Tomalin, Initial sintering of Cr_2O_3, J. Am. Ceram. Soc., 1966, 49, 23-26.

89. *MK*. Haldar, HS. Tripathi, SK. Das, A. Ghosh, Effect of compositional variation on the synthesis of magnesite-chrome composite refractory, Ceram. Int., 2004, 30, 911-915.

90. H. Zhao, S. Hu, H. Wang, The influence of nano-Fe_2O_3 on sintering and mechanical performance of magnesite–chrome refractory, 2003, Proceedings of Unitecr, Osaca, Japan 19-22, 2003, 284-287.

91. I. Ganesh, S. Bhattacharjee, BP. Saha, R. Johnson, YR. Mahajan, A new sintering aid for magnesium aluminate spinel, Ceram. Int., 2001, 27, 773-779.

92. J. Tsay, T. Fang, Effects of molar ratio of citric acid to cations and of pH value on the formation and thermal-decomposition behavior of barium titanium citrate, J. Am. Ceram. Soc., 1999, 82, 1409-1415.

93. HR. Zargar, C. Oprea, G. Oprea, T. Troczynski, The effect of nano-Cr_2O_3 on solid-solution assisted sintering of MgO refractories, Ceram. Int., 2012, 38, 6235-6241.

94. BD. Cullity BD, SR. Stock, Elements of X-Ray Diffraction (3rd Edition). Prentice Hall; 2001.

95. P. Francus, An image-analysis technique to measure grain-size variation in thin sections of soft clastic sediments, Sediment Geol, 1998, 121, 289-298.

96. ML. Mendelson, Average grain size in polycrystalline ceramics, J. Am. Ceram. Soc., 1969, 52, 443-446.

97. MJ. Mayo, Processing of nanocrystalline ceramics from ultrafine particles, Int. Mater. Rev., 1996, 41, 85-115.

98. A. Krell, J. Kli*MK*e, Effects of the homogeneity of particle coordination on solid-state sintering of transparent alumina, J. Am. Ceram. Soc., 2006, 89, 1985-1992.

99. Y. Xiong, J. Hu, Z. Shen, Dynamic pore coalescence in nanoceramic consolidated by two-step sintering procedure, J. Eur. Ceram. Soc., 2013, 33, 2087-2092.

100. N. Neves, R. Barros, E. Antunes, et al., Sintering behavior of nano- and micro-sized ZnO powder targets for rf magnetron sputtering applications, J. Am. Ceram. Soc., 2012, 95, 204-210.

101. JL. Woolfrey, Effect of green density on the initial-stage sintering kinetics of UO_2, J. Am. Ceram. Soc., 1972, 55, 383-389.

102. JMF. Colinas, CO. Arean, Kinetics of solid-state spinel formation: Effect of cation coordination preference, J. Solid. State. Chem., 1994, 109, 43-46.

103. J. Paik, M. Lee, S. Hyun, Reaction kinetics and formation mechanism of magnesium ferrites, Thermochimica Acta, 2005, 425, 131-136.

104. K. Nagata, R. Nishiwaki, Y. Nakamura, T. Maruyama, Kinetic mechanisms of the formations of $MgCr_2O_4$ and $FeCr_2O_4$ spinels from their metal oxides, Solid State Ion., 1991, 49, 161-166.

105. KH. Stern, High temperature properties and decomposition of inorganic salts part 3, nitrates and nitrites, J. Phys. Chem. Ref. Data., 1972, 1, 747-772.

106. S. Goswami, K. Kiran, Application of kissinger analysis to glass transition and study of thermal degradation kinetics of phenolicacrylic IPNs, Bull. Mater. Sci., 2012, 35, 657-664.

107. P. Ptacek, F. Soukal, T. Opravil, M. Noskova, J. Havlica, J. Brandstetr, The kinetics of Al–Si spinel phase crystallization from calcined kaolin, J. Solid State Chem., 2010, 183, 2565-2569.

108. Y. Lei, Y. Gong, Z. Duan, G. Wang , Density functional calculation of activation energies for lattice and grain boundary diffusion in alumina, Phys. Rev. B., 2013, 87, 214105.

109. R. Shannon, Revised effective ionic radii and systematic studies of interatomic distances in halides and chalcogenides, Acta Cryst. A., 1976, 32, 751-767.

110. GC. Ulmer, WJ. Smothers, The system $MgO\text{-}Cr_2O_3{-}Fe_2O_3$ at 1300°C in air, J. Am. Ceram. Soc. 1968, 51, 315-319.

111. A. Juhin, G. Calas, D. Cabaret, L. Galoisy, J. Hazemann, Structural relaxation around substitutional Cr^{+3} in $MgAl_2O_4$, Phys. Rev. B., 2007, 76, 054105.

112. U. Halenius, GB. Andreozzi, H. Skogby, Structural relaxation around Cr^{+3} and the red-green color change in the spinel magnesiochromite ($MgAl_2O_4$-$MgCr_2O_4$) and gahnite-zincochromite ($ZnAl_2O_4$-$ZnCr_2O_4$) solid-solution series, J. Am. Mineral., 95, 456-462.

113. D. Lenaz, H. Skogby, F. Princivalle, U. Haylenius, Structural changes and valence states in the $MgCr_2O_4$-$FeCr_2O_4$ solid solution series, Phys. Chem. Mineral., 2004, 31, 633-642.

114. SM. Patange, SE. Shirsath, GS. Jangam, KS. Lohar, SS. Jadhav, KM. Jadhav, Rietveld structure refinement, cation distribution and magnetic properties of Al^{+3} substituted $NiFe_2O_4$ nanoparticles, J. Appl. Phys., 2011, 109.

115. F. Martignago, GB. Andreozzi, AD. Negro, Thermodynamics and kinetics of cation ordering in natural and synthetic $Mg(Al,Fe^{+3})_2O_4$ spinels from in situ high-temperature X-ray diffraction. J. Am. Mineral., 2006, 91, 306-312.

116. F. Martignago, AD. Negro, S. Carbonin, How Cr^{+3} and Fe^{+3} affect Mg-Al order-disorder transformation at high temperature in natural spinels, Phys. Chem. Mineral., 2003, 30, 401-408.

117. DS. Walters, SP. Wirtz, Kinetics of cation ordering in magnesium ferrite, J. Am. Ceram. Soc., 1971, 54, 563-566.

118. X. Wang, J. Liu, Y. Kan, G. Zhang, Effect of solid solution formation on densification of hot-pressed ZrC ceramics with MC (M = V, Nb, and Ta) additions. J. Eur. Ceram. Soc., 2012, 32, 1795-1802.
119. D. Carta, MF. Casula, A. Falqui, et al, A structural and magnetic investigation of the inversion degree in ferrite nanocrystals MFe_2O_4 (M = Mn, Co, Ni). J. Phys. Chem. C., 2009, 113, 8606-8615.

120. JHE. Jeffes, Ellingham diagrams. In: Editors-in-Chief, K. H. Jurgen Buschow A. Robert W. Cahn A. Merton C. Flemings A. Bernard Ilschner (print) A. Edward J. Kramer A2Subhash Mahajan, Patrick Veyssiere (updates), *EDS*. Encyclopedia of Materials: Science and Technology (Second Edition). Oxford: Elsevier; 2001:2751-2753.

121. U. Haylenius, GB. Andreozzi, H. Skogby, Structural relaxation around Cr^{+3} and the red-green color change in the spinel (sensu stricto)-magnesiochromite ($MgAl_2O_4$-$MgCr_2O_4$) and gahnite-zincochromite ($ZnAl_2O_4$-$ZnCr_2O_4$) solid-solution series., J. Am. Mineral. 2010, 95, 456-462.

122. B. Lavina, G. Salviulo, AD. Giusta, Cation distribution and structure modelling of spinel solid solutions, Phys. Chem. Mineral., 2002, 29, 10-18.

123. SM. Barinov, Li. Shvorneva, D. Ferro, IV. Fadeeva, SV. Tumanov, Solid solution formation at the sintering of hydroxyapatite–fluorapatite ceramics, Sci. Tech. Adv. Mater., 2004, 5, 537-541.

124. D. Park, K. Son, J. Lee, J. Kim, J. Lee, Effect of ZnO addition in In_2O_3 ceramics: Defect chemistry and sintering behavior, Solid State Ion., 2004, 172, 431-434.

125. MD. Lima, R. Bonadimann, MJ. de Andrade, JC. Toniolo, CP. Bergmann, Nanocrystalline Cr_2O_3 and amorphous CrO_3 produced by solution combustion synthesis, J. Eur. Ceram. Soc., 2006, 26, 1213-1220.

126. KA. Berry,MP. Harmer, Effect of MgO solute on microstructure development in Al_2O_3, J. Am. Ceram. Soc., 1986, 69,143-149.

127. K. Lu, W. Li, B. Chen, Sintering of porous materials, In: Castro R, Benthem K, eds. Springer Berlin Heidelberg; 2013, 115-136.

128. VS. Stubican, I. de Menzes, Grain-boundary reactions in magnesia-chrome refractories: Application of the electron probe I, J. Am. Ceram. Soc. 1966, 49, 535-540.

129. DM. Karpinos, LI. Tuchinskii, AB. Sapozhnikova, LR. Vishnyakov, Sintering of two-phase composites with undeformable inclusions, Sov. Powder Metal. Ceram., 1976, 15, 519-523.

130. JD. Bolton, Aj. Gant, Microstructural development and sintering kinetics in ceramic reinforced high speed steel metal matrix composites, Powder Metal, 1997, 40, 143.

131. D. Fan, L. Chen, Computer simulation of grain growth and ostwald ripening in Alumina-Zirconia two-phase composites, J. Am. Ceram. Soc., 1997, 80, 1773-1780.

132. I. Warshaw, ML. Keith, Solid solution and chromium oxide loss in part of the system MgO-Al_2O_3-Cr_2O_3-SiO_2, J. Am. Ceram. Soc., 1954, 37, 161-168.

133. T. Sata, HL. Lee, Vacuum Vaporization in the system MgO-Cr_2O_3, J. Am. Ceram. Soc. 1978, 61, 326-329.

134. K. Goto, WE. Lee, 'Direct bond' in magnesia chromite and magnesia spinel refractories, J. Am. Ceram. Soc., 1995, 78, 1753-1760.

135. D. Tromans, JA. Meech, Fracture toughness and surface energies of minerals: Theoretical estimates for oxides, sulphides, silicates and halides, Mineral. Eng., 2002,15, 1027-1041.

136. BJ. Kellett, FF. Lange, Thermodynamics of densification: I, sintering of simple particle arrays, equilibrium configurations, pore stability, and shrinkage, J. Am. Ceram. Soc., 1989, 72, 725-734.

137. M. Mazaheri, AM. Zahedi, SK. Sadrnezhaad, Two-step sintering of nanocrystalline ZnO compacts: Effect of temperature on densification and grain growth, J. Am. Ceram. Soc., 2008, 91, 56-63.

138. J. Li, Y. Ye, Densification and grain growth of Al_2O_3 nanoceramics during pressureless sintering, J. Am. Ceram. Soc., 2006, 89, 139-143.

139. A. Saberi, F. Golestani-Fard, H. Sarpoolaky, M. Willert-Porada, T. Gerdes, R. Simon, Chemical synthesis of nanocrystalline magnesium aluminate spinel via nitrate–citrate combustion route, J. Alloys. Compds, 2008, 462, 142-146.

140. MJ. de Andrade, MD. Lima, R. Bonadiman, CP. Bergmann, Nanocrystalline pirochromite spinel through solution combustion synthesis, Mater. Res. Bull., 2006, 41, 2070-2079.

141. NA. Haroun, Theory of inclusion controlled grain growth, J. Mater. Sci., 1980, 15, 2816-2822.

142. FF. Lange, MM. Hirlinger, Hindrance of grain growth in Al_2O_3 by ZrO_2 inclusions, J. Am. Ceram. Soc., 1984, 67,164-168.

143. D. Kolar,M. Trontelj, Z. Tadler, Influence of interdiffusion on solid solution formation and sintering in the system $BaTiO_3$-$SrTiO_3$, J. Am. Ceram., 1982, 65, 470-474

144. C. Herring, Effect of change of scale on sintering phenomena, J. Appl. Phys., 1950, 21, 301-303.

145. Z. Razavi Hesabi, M. Haghighatzadeh, M. Mazaheri, D. Galusek, SK. Sadrnezhaad SK., Suppression of grain growth in sub-micrometer alumina via two-step sintering method, J. Eur. Ceram. Soc., 2009, 29, 1371-1377.

146. M. Mazaheri, M. Haghighatzadeh, AM. Zahedi, SK. Sadrnezhaad, Effect of a novel sintering process on mechanical properties of hydroxyapatite ceramics, J. Alloy. Compd., 2009, 471, 180-184.

147. QY. Chen, CM. Meng, TC. Lu, et al., Enhancement of sintering ability of magnesium aluminate spinel ($MgAl_2O_4$) ceramic nanopowders by shock compression, Powder Technol. 2010, 200, 91-95.

148. I. Ganesh, JFM. Ferreira, Synthesis and characterization of $MgAl_2O_4$-ZrO_2 composites, Ceram. Int., 2009, 35, 259-264.

149. N. Kuskonmaz, N. Can, A. Can, L. Sigalas, Sintering behavior of nano-crystalline γ-Al_2O_3 powder without additives at 2-7 GPa. Ceram. Int., 2011, 37, 437-442.

150. F. Meng, C. Liu, F. Zhang, Z. Tian, W. Huang, Densification and mechanical properties of fine-grained Al_2O_3–ZrO_2 composites consolidated by spark plasma sintering. J. Alloy. Compds., 2012, 512, 63-67.

151. A. Rabiezadeh, A. Ataie, AM. Hadian, Sintering of Al_2O_3–TiB_2 nano-composite derived from milling assisted sol–gel method. Int. J. Ref. Metal. Hard. Mater., 2012, 33, 58-64.

152. M. Mazaheri, M. Valefi, ZR. Hesabi, SK. Sadrnezhaad, Two-step sintering of nanocrystalline $8Y_2O_3$ stabilized ZrO_2 synthesized by glycine nitrate process, Ceram. Int., 2009, 35,13-20.

153. X. Wang, P. Chen, I. Chen, Two-step sintering of ceramics with constant grain-size, I. Y_2O_3. J. Am. Ceram. Soc., 2006, 89, 431-437.

154. K. Bodiaova, A. Ajgalak, D. Galusek, A. Vana, Two-stage sintering of alumina with submicrometer grain size, J. Am. Ceram. Soc., 2007, 90, 330-332.

155. J. Ding, Y. Liu, Y. Lu, et al, Enhanced energy-storage properties of $0.89Bi0.5Na0.5TiO_3$–$0.06BaTiO_3$–$0.05K0.5Na0.5NbO_3$ lead-free anti-ferroelectric ceramics by two-step sintering method, Mater. Lett., 2014, 114, 107-110.

156. M. Wu, Two-step sintering of aluminum-doped zinc oxide sputtering target by using a submicrometer zinc oxide powder, Ceram. Int., 2012, 38, 6229-6234.

157. K. Pietrzak, M. Chmielewski, W. Włosiński, Sintering Al_2O_3-Cr composites made from micro and nano powders, Sci. sintering, 2004, 36, 171.

158. T. Gupta, Sintering of MgO: Densification and grain growth, J. Mater. Sci., 1971, 6, 5-32.
159. KPR. Reddy, AR. Cooper, Oxygen diffusion in magnesium aluminate spinel, J. Am. Ceram. Soc., 1981, 64, 368-371.

160. R. Porat, S. Berger, A. Rosen, Dilatometric study of the sintering mechanism of nanocrystalline cemented carbides, Nanostructured Mater., 1996, 7, 429-436.

161. Z. He, J. Ma, Grain-growth rate constant of hot-pressed alumina ceramics, Mater. Lett., 2000, 44, 14-18.

162. J. Zhao, MP. Harmer, Effect of pore distribution on microstructure development: II, first- and second-generation pores, J. Am. Ceram. Soc., 1988, 71, 530-539.

163. M. Chu, LC. De Jonghe, *MK*F. Lin, FJT. Lin, Precoarsening to improve microstructure and sintering of powder compacts. J. Am. Ceram. Soc., 1991, 74, 2902-2911.

164. X. Song, J. Lu, T. Zhang, J. Ma, Two-stage master sintering curve approach to sintering kinetics of undoped and Al_2O_3-doped 8 mol% yttria-stabilized cubic zirconia, J. Am. Ceram. Soc., 2011, 94, 1053-1059.

165. N. Benameur, G. Bernard-Granger, A. Addad, S. Raffy, C. Guizard, Sintering analysis of a fine-grained Alumina-Magnesia spinel powder, J. Am. Ceram. Soc., 2011, 94,1388-1396.

166. D. Li, S. Chen, W. Shao, X. Ge, Y. Zhang, S. Zhang, Densification evolution of TiO_2 ceramics during sintering based on the master sintering curve theory, Mater. Lett., 2008, 62, 849-851.

167. JD. Hansen, RP. Rusin, M. Teng, DL. Johnson, Combined-stage sintering model, J. Am. Ceram. Soc. 1992, 75, 1129-1135.

168. YJ. Sheng, GJ. Wasserburg, ID. Hutcheon, Self-diffusion of magnesium in spinel and in equilibrium melts: Constraints on flash heating of silicates, Geochim Cosmochim Acta. 1992, 56, 2535-2546.

169. H. Peng, B. Myhre, Improved flow of refractory castables by optimised particle size distribution, International Colloquium on Refractores, Achen, Germany, 2012.

170. LF. Amaral, IR. Oliveira, P. Bonadia, R. Salomão, VC. Pandolfelli, Chelants to inhibit magnesia (MgO) hydration, Ceram. Int. 2011, 37, 1537-1542.

171. VSS. Birchal, SDF. Rocha, VST. Ciminelli, The effect of magnesite calcination conditions on magnesia hydration, Mineral. Eng., 2000,13,1629-1633.

172. R. Salomao, VC. Pandolfelli, Magnesia sinter hydration-dehydration behavior in refractory castables, Ceram. Int., 2008, 34, 1829-1834.

173. NJ. Lang, B. Liu, X. Zhang, J. Liu, Dissecting colloidal stabilization factors in crowded polymer solutions by forming self-assembled monolayers on gold nanoparticles Langmuir, 2013, 29, 6018-6024.

174. ASTM C1437-13, standard test method for flow of hydraulic cement mortar. 2013.

175. V. Petkov, PT. Jones, E. Boydens, B. Blanpain, P. Wollants, Chemical corrosion mechanisms of magnesia–chromite and chrome-free refractory bricks by copper metal and anode slag, J. Eur. Ceram. Soc., 2007, 27, 2433-2444.

176. ZF. Yuan, WL. Huang, K. Mukai, Local corrosion of Magnesia–Chrome refractories driven by marangoni convection at the Slag–Metal interface, J. Colloid Interface Sci., 2002, 253, 211-216.

177. M. Wang, C. Hsu, M. Hon, The reaction between the magnesia–chrome brick and the molten slag of $MgO–Al_2O_3–SiO_2–CaO–FeO$ and the resulting microstructure, Ceram. Int. 2009, 35, 1501-1508.